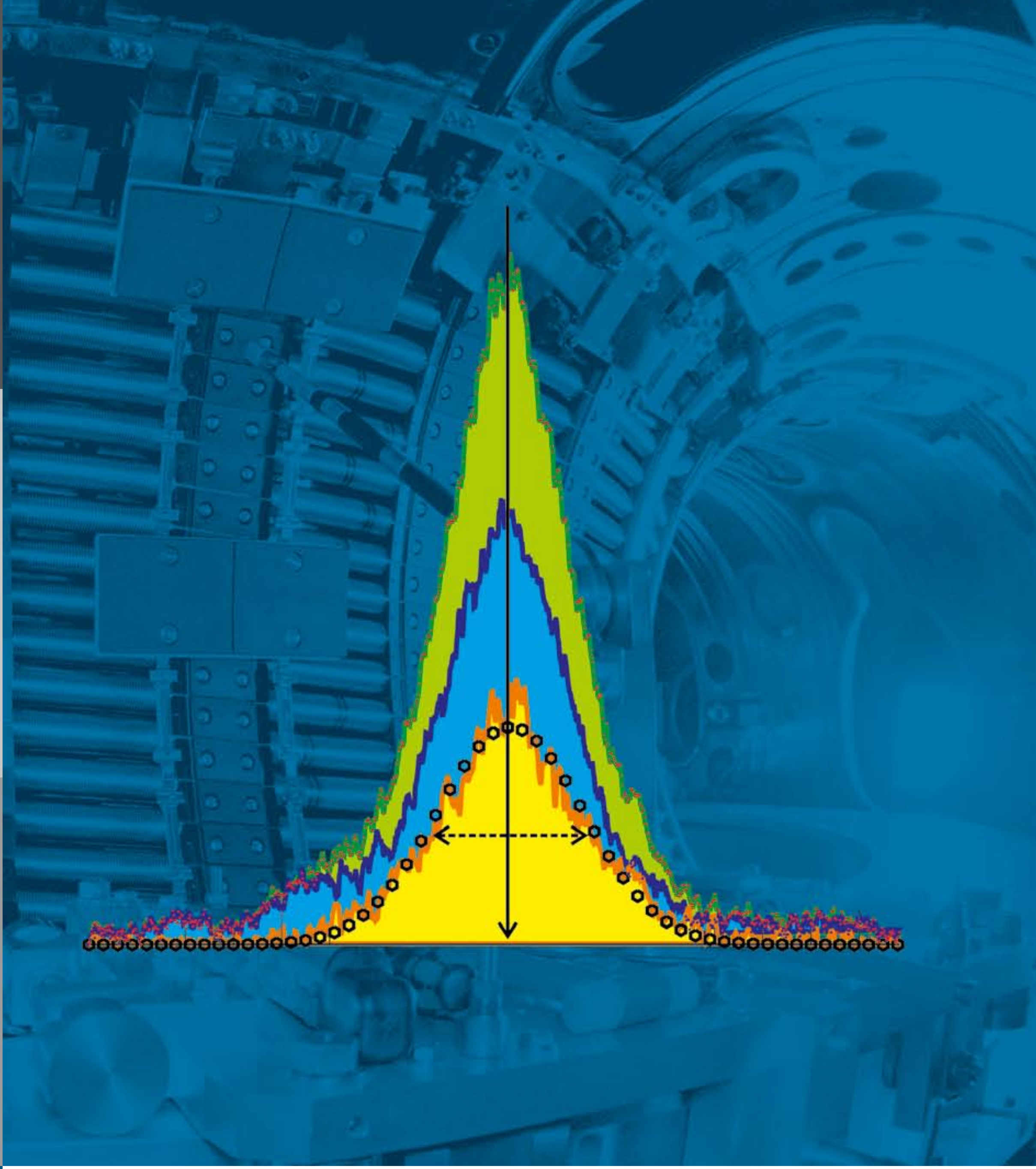

The Influence of the Dynamic Ergodic Divertor on the Radial Electric Field at the Tokamak TEXTOR

Jan Willem Coenen

JÜLICH
FORSCHUNGSZENTRUM

Mitglied der Helmholtz-Gemeinschaft

Schriften des Forschungszentrums Jülich
Reihe Energie & Umwelt / Energy & Environment Band / Volume 39

Forschungszentrum Jülich GmbH
Institute of Energy Research (IEF)
Plasma Physics (IEF-4)

The Influence of the Dynamic Ergodic Divertor on the Radial Electric Field at the Tokamak TEXTOR

Jan Willem Coenen

Schriften des Forschungszentrums Jülich
Reihe Energie & Umwelt / Energy & Environment Band / Volume 39

ISSN 1866-1793 ISBN 978-3-89336-574-6

Bibliografische Information der Deutschen Nationalbibliothek.
Die Deutsche Nationalbibliothek verzeichnet diese Publikation in der
Deutschen Nationalbibliografie; detaillierte Bibliografische Daten
sind im Internet über <http://dnb.d-nb.de> abrufbar.

Herausgeber und Vertrieb: Forschungszentrum Jülich GmbH
Zentralbibliothek, Verlag
D-52425 Jülich
Telefon (02461) 61-5368 · Telefax (02461) 61-6103
e-mail: zb-publikation@fz-juelich.de
Internet: http://www.fz-juelich.de/zb

Umschlaggestaltung: Grafische Medien, Forschungszentrum Jülich GmbH

Druck: Grafische Medien, Forschungszentrum Jülich GmbH

Schriften des Forschungszentrums Jülich
Reihe Energie & Umwelt / Energy & Environment Band / Volume 39

D 61 (Diss., Düsseldorf, Univ., 2009)

ISSN 1866-1793
ISBN 978-3-89336-574-6

Kurzfassung

Der Gegendstand dieser Arbeit ist die Untersuchung des Einflusses von resonanten externen Störfeldern (RMPs) auf das radiale elektische Feld E_r in magnetisch eingeschlossenen Hochtemperaturplasmen mittels Ladungsaustauschspektroskopie (CXRS) am Tokamak TEXTOR. Dazu wurde eine optische Diagnostik entwickelt, welche CXRS an C^{6+} unter Ausnutzung eines Wasserstoffdiagnostikstrahles ermöglicht. Zwei Systeme, eines zu Messung der poloidalen Rotation v_θ und der Ionentemperatur sowie eines zur Messung der toroidalen Rotation v_ϕ, werden verwandt. Die Instrumentation erlaubt Messungen mit 1-2 cm radialer Auflösung bei einer 1 km/s Auflösung für v_θ und 5 km/s für v_ϕ. Die radiale Kalibrierung der Beobachtungssysteme wird mit aktiver Beam-Emissions-Spektroskopie (Dopplerverschiebung) durchgeführt. Die Festlegung der Wellenlänge geschieht durch differentielle Dopplerspektroskopie für das poloidale und durch eine Neonreferenzlinie für das toroidale System. Das E_r wird abgeleitet unter Benutzung der radialen Kräftebilanz für C^{6+} Ionen. Die externen Störfelder werden hier durch den Dynamischen Ergodischen Divertor (DED) in der $m/n = 6/2$ Basismode aufgeprägt.
Mittels des neuen Beobachtungssystems wurden Studien zum Einfluss externer Drehmomente auf Rotation und E_r durchgeführt. Die toroidale Rotation folgt dem durch Neutralteilcheninjektoren eingebrachten Drehmoment. Eine Nullpunktsverschiebung entgegen des Plasmastromes wird bei ausgeglichenem Impulseintrag beobachtet. Im Plasmarand wird die v_ϕ durch Reibung an Neutralteilchen gebremst und folgt der Teilchenfluss in der Abschälschicht. Die poloidale Rotation folgt im Plasmazentrum der poloidalen Komponente des Drehmomenteintrages (3 ± 3 km/s); im Plasmarand wird die poloidale Rotation durch Drifteffekte und Verluste von schnellen Teilchen des NBI dominiert.
Der Einfluss des DED manifestiert sich in einer Zunahme der Rotation in Korrelation mit der Störamplitude und daher einem positiveren E_r. Ein Anstieg von +10 kV/m kann beobachtet werden. Der toroidale Beitrag zum E_r erhöht sich über den gesamten Plasmaradius. Dieses Verhalten wird durch die hohe Senkrechtviskosität verursacht. Der poloidale Beitrag ist stark lokalisiert innerhalb der durch die externe Störung verursachten ergodischen Zone, hier wirkt eine $\vec{j} \times \vec{B}$ Kraft. Diese wird durch einen nach innen gerichteten Ionenstrom, der einen erhöhten Elektronenverlust kompensiert verursacht.
Der DED kann das globale Einschlussverhalten ändern: Abhängig vom Sicherheitsfaktor (q_a) im Plasmarand erhält man verbesserten oder verschlechterten Teilcheneinschluss. Im Fall verbesserten Teilcheneinschlusses, genannt „Improved Particle Confinemeny (IPC)", beobachtet man einen Anstieg von Dichte (40%) und Teilcheneinschusszeit τ_p (30%), korreliert mit einer Verbindung von Feldlinien zwischen der q=5/2 Fläche und den DED Wandelementen. Dies ist mit einer Verringerung des Teilchentransportes korreliert und führt zu einem positiven Anstieg des E_r und der E_r-Verscherungsrate ($\Delta\Omega \simeq 1.5 \cdot 10^5 s^{-1}$) bei q=5/2. Die Änderungen in der berechneten magnetischen Vacuumtopology korrelieren mit sichtbaren Veränderungen in der Teilchenflussverteilung auf den DED Wandelementen. Feldlinien dringen nach außen, Strukturen erscheinen ab $I_{DED} = 2.5$ kA. Mit zunehmender DED Amplitude wird der ergodische Bereich breiter, der Teilcheneinschluss besser. Sobald aber die q=5/2 Fläche komplett ergodisiert ist, verschlechtert sich der Einschluss deutlich.
Der Übergang in dieses, „particle Pump Out(PO)" genannte, Szenario kann eher erzwungen werden, indem die q=5/2 Fläche zur HFS verschoben wird, q=5/2 wird dann direkt ergodisiert und der Transport durch laminare Feldlinien (kurze Verbindungen zum DED) dominiert. Der Einschluss verschlechtert sich. Veränderungen in der Verscherungsrate treten nicht auf.
Ein Anstieg in der E_r Verscherungsrate und der verbesserte Einschluss sind genereall korreliert.Vermutlich ist dies verbunden mit einer Abnahme von Dichtefluktuationen wie in Messungen unter Einfluss der 3/1 DED Basismode beobachtet wurde.

Abstract

In this work the influence of external Resonant Magnetic Perturbations (RMPs) on the radial electric field E_r in magnetically confined plasmas is investigated by Charge Exchange Recombination Spectroscopy (CXRS) at the Tokamak TEXTOR. For this purpose, an optical diagnostic was developed to perform CXRS with C^{6+} ions utilizing a neutral hydrogen diagnostic beam. Two systems are used to measure the poloidal rotation as well as the ion pressure and the toroidal rotation, respectively. The setup allows measurements with 1-2 cm radial resolution and a velocity resolution of typically 1 km/s for v_θ and 5 km/s for v_ϕ. For the radial calibration active beam emission spectra (Doppler shift) are used. The wavelength reference is determined via differential Doppler shift spectroscopy and a neon reference line for the poloidal and toroidal system, respectively. The radial electric field, E_r, is then deduced from the radial force balance of C^{6+} ions. The experiments have been performed at the Tokamak TEXTOR. Here, the RMPs are produced with the Dynamic Ergodic Divertor (DED), a set of 16 helical perturbation coils located at the high field side of TEXTOR. Within this work, the base mode number of perturbations has been $m/n = 6/2$.

With these new observation systems, we have first investigated the influence of external torque from neutral heating beams on plasma rotation and E_r. The toroidal rotation in the center is proportional to the net beam torque with an offset counter-current rotation at zero net torque. At the plasma edge, the toroidal rotation is dampened by friction with neutrals and coupled to the counter-current Scrape-Off layer flow by perpendicular viscosity. The poloidal rotation follows the poloidal component of the beam torque in the plasma center (ranging from $3 \pm 3\,\mathrm{km/s}$), at the plasma edge it is dominated by drift effects and loss of fast particles of the counter beam.

Under influence of the DED, a spin-up of rotation with the rise of the perturbation amplitude causes the E_r to become more positive. An increase of $+10$ kV/m is observed. The toroidal contribution increases all across the minor radius because of the large perpendicular viscosity, while the poloidal contribution increases only locally inside the ergodic zone caused by the RMPs. The ergodic zone causes an electron loss, and subsequently a $\vec{j} \times \vec{B}$ force driven by the compensating ion return current.

In addition, the DED changes the global confinement properties. Depending on the edge safety factor (”field line twist”) q_a, either increased or decreased particle confinement is observed. In case of the increased particle confinement (IPC) the increase in density (40%) and particle confinement time τ_p (30%) is correlated to the connection of field lines at the q=5/2 surface to the DED target, locally changing the transport properties and the E_r. Transport is reduced and the E_r shear is increased locally at q=5/2 up to $1.5 \cdot 10^5 s^{-1}$, while the E_r becomes more positive. The changes in magnetic topology calculated in the vacuum approximation for the radial perturbation field can be related to the experimental particle flux pattern at the DED target. This situation is characterized by field lines connecting the ergodized x-points of the 5/2 island chain to the target. With further increasing perturbation, the ergodic zone widens, the particle confinement increases, up to the point where the q=5/2 surface is completely ergodized and the particle confinement decreases again.

Under conditions, where the q=5/2 surface is closer to the perturbation coils (smaller edge safety factor), the particle confinement is observed to decrease (particle Pump Out - PO), local field line connections to the target are not established and enhanced transport within laminar flux tubes with short connection to the target directly leads to the loss in global confinement.Enhanced shear in E_r is not observed for this case.

Increased E_r shear and increased particle confinement are correlated.They probably are connected to a reduction of density fluctuations as was observed in discharges under the influence of DED in $m/n = 3/1$ base mode configuration.

Contents

Chapter 1

Introduction

The limited supply of fossil fuels and the connected issues of pollution and climate change are forcing the turnaround towards sustainable and clean energies.

A viable new primary energy source is needed. Fusion power is one of the most ambitious and promising scientific projects of our times, aiming at providing one of the most reliably available future energy sources [Horton 08, Williams 02] .

Nuclear fusion utilizes the energy output resulting from the fusion of singly and doubly heavy water, deuterium and tritium, raw material that is either abundant (deuterium) in nature or can be bread from lithium (tritium).

The fusion process applicable with highest cross section at low energies

$$ {}^{2}_{1}D +^{3}_{1} T \rightarrow^{4}_{2} He + n^{0} + 17.6\text{MeV} \tag{1.1} $$

causes the hydrogen isotopes to fuse into helium and release one neutron in conjunction with the release of 17.6 MeV of binding energy [Wesson 97]. The helium takes 3.5 MeV while the neutron has a kinetic energy of 14.1 MeV. In order to gain energy from this reaction a setup has to be devised that allows the confinement of the reaction partners for a duration large enough to ensure collisions and hence fusion. The fuel mixture has to be brought up to high enough temperature and pressure. Since the kinetic energy follows the Maxwell-Boltzmann distribution a temperature of about $4 \cdot 10^7$ K (average energy of $\sim$ 10keV) is sufficient for a viable fusion power production. At such temperature the gas is fully ionized and forms a thermonuclear plasma.

The next step towards the realization of fusion power as a new primary energy source is the international tokamak ITER, the largest magnetic confinement experiment so far (plasma volume ITER: 837 m^3 JET (largest device today): 80 m^3). For the first time an output of 500 MW fusion power will be targeted with a gain (Q) larger than ten to demonstrate the feasibility of fusion. Q is the ratio of fusion power to externally injected heating power which can be above one only in a sufficiently confined thermonuclear plasma. A typical fusion power-plant has to reach Q ≥ 50 in order to operate economically [Horton 08].

In order to reach this ambitious goal, several smaller facilities have been working towards the aim of developing a viable scenario for ITER from a physics and engineering perspective. Experiments at the JET tokamak showed that break even is possible with a device of that size. JET, in addition, produced 16MW of fusion power during its deuterium-tritium campaign.

To reach the envisioned 500 MW fusion power with ITER, the base line plasma scenario will be the so-called H-Mode. The H-Mode is characterized by an improved confinement connected to the spontaneous onset of a transport barrier close to the plasma edge by means of external heating power [Wagner 82, Wagner 84]. The transport barrier in the H-Mode is associated with a strong pressure gradient in the edge. This gradient is also the origin of pressure driven instabilities, so-called Edge Localized Modes(ELMs). The pressure gradient relaxes periodically causing a burst of particles and energy onto the plasma facing components [Zohm 92, Zohm 96].

Based on extrapolations ELMs could have devastating effects on the first wall of the ITER device. Those transient events will be connected to heat loads large enough to cause significant melt damage, carbon erosion, cracking of wall tiles and hence substantially limit the operational time and availability of ITER [Leonard 99, Becoulet 03, Loarte 07, Linke 08]. This means that while keeping the advantageous improvement of confinement one needs to devise a method to mitigate the ELMS to a sustainable level or suppress them completely [Becoulet 03].

It was shown [Evans 04, Evans 06b, Liang 07] that by means of external resonant magnetic perturbations (RMPs), imprinted by external coils, a stochastization of the plasma edge can be achieved effectively changing the pressure gradient to a sustainable level, suppressing the ELMs. RMPs are one tool to effectively control ELMs and are considered for operation in ITER and future devices. In order to extrapolate those results for ITER or even the prototype reactor DEMO and the corresponding coil design, a detailed understanding of the changes in the plasma edge during H-Mode and ELM suppression is required.

The radial electric field E_r is one of the most important aspects in this context as the sheared $\vec{E} \times \vec{B}$ rotation is thought to be instrumental for the onset of the H-Mode. The suppression of anomalous / turbulent transport is the most convincing concept to explain the emergence of the transport barrier. This turbulent driven transport is typically thought to be caused by micro instabilities in plasma density, temperature and plasma potential [Biglari 90, Ida 98].

It is seen that a strong $\vec{E} \times \vec{B}$ shear is connected to the onset of improved confinement scenarios [Biglari 90, Moyer 95, Burrell 97, Burrell 05] such as seen in the changes occurring with the transition into high confinement mode [Ida 90]. The shear is driven by either the steep pressure gradient (H-Mode) or the poloidal rotation [Groebner 90, Burrell 97] as part of the radial force balance ($E_r(\nabla p, v_\theta, v_{phi})$) [Kim 91, Rozhansky 96].

Experiments with external magnetic perturbations have been performed at TEXT, Tore Supra, TEXTOR and have revealed many basic aspects of transport and structure formation of plasmas with stochastic boundaries, however, mostly in L-Mode plasmas [DeMichelis 95, Ghendrih 96, Schmitz 07].

At TEXTOR the Dynamic Ergodic Divertor (DED) is installed [Finken 98, Finken 99b], a very flexible tool to control power exhaust to the first wall, plasma edge transport and rotation [Finken 01, Finken 05b, De Bock 08]. The DED, consisting of sixteen helically wound coils, at the high field side of TEXTOR, can produce a magnetic multipole field by running either DC or AC current. This magnetic field is able to break up the closed flux surfaces by resonantly interacting with the magnetic field at the rational flux surfaces, causing a stochastic plasma boundary.

The changes in plasma rotation are in general connected to the evolution of the radial electric field through the radial force balance . Assuming a stochastic or ergodic system as stated above will lead to a loss of electrons and hence cause a more positive radial electric field towards the center of the plasma which in turn has to be connected to a spin up of rotation due to a $\vec{j} \times \vec{B}$ force [Unterberg 07]. This enhanced particle loss and the connected radial ion return current [Kaganovich 98, Cornelis 94] are spinning up the rotation into the co-current or ion diamagnetic drift direction.

In this work, a detailed study of the radial electric field under the influence of the DED connects the changes in plasma transport to changes in the E_r profile and hence provides an insight to the improvement of confinement with respect to turbulent suppression by means of $\vec{E} \times \vec{B}$ shearing.

In order to be able to measure the radial electric field, high resolution diagnostics for the rotation are required, since especially the poloidal rotation can be very small. Typically for divertor tokamaks the poloidal rotation is measured with a resolution in the order of kilometers [Groebner 90]. Effects caused by the DED are in the range of such uncertainties; hence a system had to be devised to improve the resolution well below 1 km/s.

Charge exchange spectroscopy on carbon impurities is the most successful tool at the moment for the measurement of impurity rotation and temperature profiles [Fonck 84, Isler 94]. Carbon as one of the prominent target materials for the vessel wall is always present in the plasma in small amounts.

At TEXTOR the main diagnostic used in this work is a charge exchange spectroscopy setup utilizing a toroidal and poloidal observation system in combination with a low power hydrogen diagnostic beam. Since carbon is fully ionized at the temperatures present, the neutral hydrogen from the diagnostic beam or any hydrogen beam (NBI) is able to actively populate the energy levels via charge exchange. Emission from those ions then allows localized measurements of Doppler shift and spectral broadening to determine the impurity ion velocity and temperature.

Compared to other diagnostics like Doppler Reflectometry [Conway 04, Soldatov 07, Trier 08]. or the heavy ion beam probe [Ida 98] the advantages of this charge exchange diagnostic are, its high spectral and rotation resolution as well as its large coverage over half of the minor radius $0.5 < r/a < 1.1$, including the whole plasma edge. This diagnostics is capable of supplying all necessary information for the radial force balance and thus the radial electric field calculations .

The aim of this work is to study the influence of the Dynamic Ergodic Divertor on the radial electric field by means of Charge Exchange Recombination Spectroscopy and determine the role of the E_r and its shear during global confinement transitions.

This meant developing a viable method to measure the radial electric field in a consistent fashion. Thus a toroidal observation system for the hydrogen diagnostic beam RuDI [Ivanov 04, Deichuli 05] was developed to complement the existing poloidal system [Busch 06, Kreter 01].

In order to make measurements of the radial electric field, the diagnostic had to be improved to realize measurements with 0.7 km/ s and 5 km/s resolution for the poloidal and toroidal rotation direction, respectively.

Equipped with this diagnostic, measurements during the newly discovered [Finken 07a] Improved Particle Confinement (IPC) scenario were made. The connection between the improvement in particle confinement time and its connection with changes in the E_r should be studied. All contributions to the radial force balance are measured ($\nabla p, v_\theta, v_\phi$). The question on how the radial electric field is affecting, or is affected by, the IPC and the changes in magnetic topology should be answered in order to compare the general paradigm [Biglari 90, Moyer 95] of turbulent suppression and the existence of transport barriers with strong $\vec{E} \times \vec{B}$ shear, with the observation during IPC. Connecting the evolution of the radial electric field and its shear to the DED induced magnetic topology and the in parallel evolving IPC should be compared with measurements of turbulent transport [Xu 07, Kramer-Flecken 06] indicating indeed a prominent role of the E_r in the evolution of transport barriers and the IPC.

The work presented here is structured in the following manner:

In **chapter 2:** *Physics Principles of Tokamak Transport and Rotation* (p. 7) the basic principles for this work are elucidated. Starting with the principles for plasma confinement and transport regimes this chapter finally presents the equations determining the rotation for a one and two component plasma as well as the radial force balance deducing the radial electric field and its shearing rate.
Chapter 3: *TEXTOR and The Dynamic Ergodic Divertor (DED)* (p. 23) is used to describe the TEXTOR Tokamak, the plasma experiment on which the presented work has been performed. In addition the Dynamic Ergodic Divertor and its properties are presented here as they will be used during the discussion of the results.
Since one of the main aspects of the work was the development, design and improvement of the Charge Exchange Diagnostic on the RuDI hydrogen beam, **chapter 4:** *Spectroscopy & Diagnostics* (p. 37) is dedicated to the description of the diagnostic and its features. It gives an overview on the capabilities and special features of both the high resolution poloidal as well as toroidal observation system. In addition it explains the methods used to acquire rotation and temperature measurements form the spectra as well as the methods used for the radial calibration.
chapter 5: *Data Evaluation* (p. 57) will be used introduce the actual measurements as well as the methods of data evaluation including a detailed analysis of the measurement uncertainties connected to photon statistics.
The outcome of the measurements performed with the developed diagnostics are presented in **chapter 6:** *Results* (p. 67). They include the first ever performed toroidal rotation measurement in the very plasma edge of TEXTOR, as well as the first consistently measured radial electric field profiles via Charge Exchange Recombination Spectroscopy at TEXTOR and the first consistently measured profiles under the influence of external magnetic perturbation (DED) altogether. Data under the influence of different external momentum input is shown as well as the detailed analysis of the so-called Improved Particle Confinement (IPC) scenario with respect to changes in plasma parameters, confinement time and the changes in the radial electric field.

This analysis allows a connection of the topological changes induced by the external magnetic perturbation and the changes in the rotation and hence the radial electric field. This presents the unique opportunity to study the influence of E_r changes and its implication on transport suppression (turbulence). Results regarding turbulence behavior with DED are shown as well to compare with the $\vec{E} \times \vec{B}$ shearing rate and the comparison with established hypotheses for transport barriers and suppressed turbulent transport.

chapter 7: *Summary & Outlook* (p. 119) is the place for the final overview on the results. Here the conclusions with respect to the acquired data are presented. Based on the experience with the existing diagnostic setup and acquired results an outlook is presented for future improvements on the diagnostic setup and with respect to future experiments.

Chapter 2

Physics Principles of Tokamak Transport and Rotation

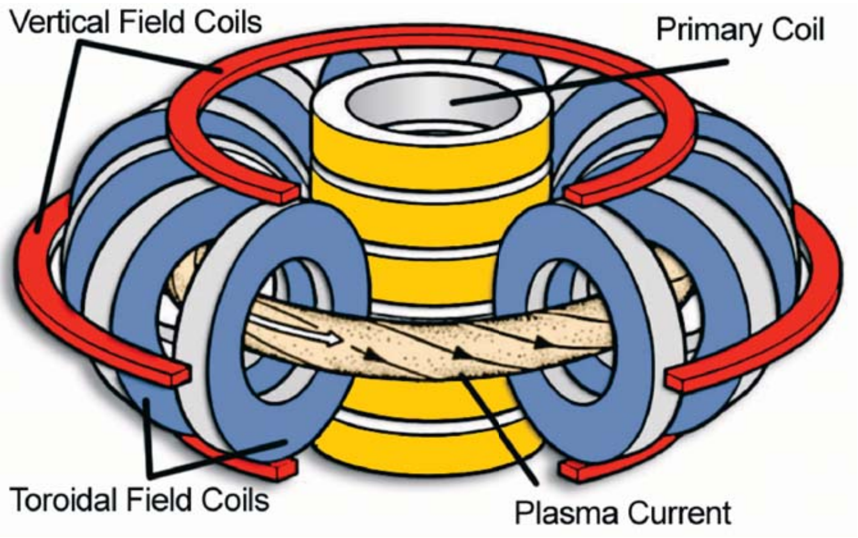

Figure 2.1: Sketch of a basic tokamak setup, showing an air solenoid as the primary coil driving the plasma current which in turn produces the poloidal magnetic field. Also shown are the toroidal field coils which produce the toroidal field component and some vertical magnetic field coils.

2.1 The Tokamak

In the following chapter some of the basic physical aspects of confining a thermonuclear plasma with a tokamak device will shortly be browsed through: the basics for toroidal plasma confinement, beginning with the description of the basic particle drift motions and their effects, the necessary confining magnetic fields and the different transport regimes originating from the confinement method (neoclassical transport). The following sections will describe the concept of the tokamak confinement and some basics on the resulting transport physics. Especially the section on plasma rotation and radial electric field will later be used to discuss the measured data and resulting interpretations.

In order to confine a highly energetic plasma one can, for instance, use the charge of the particles, that is use the inherent properties of the plasma to confine it. A plasma is basically ionized gas and hence can be confined using electromagnetic fields.

From this, one can deduce the concept of magnetic confinement. Charged particles are gyrating around magnetic field lines but move freely along them and thus can be confined when choosing a viable magnetic configuration ([Wesson 97]). In the history of fusion research several concepts have been used in the past, out of which two realistic options have manifested themselves. The stellarator, operating with a completely external magnetic field, and the tokamak where the magnetic field confining the plasma is in part originating from a current driven inside the plasma itself.

Nowadays the most promising option to achieve nuclear fusion on an commercial level seems to be the tokamak which reaches far better energy confinement conditions than the more demanding concept of a stellarator. The machine discussed in the course of this work is the tokamak TEXTOR (described in Chapter 3).

A typical tokamak setup is shown in figure 2.1, showing the mechanical setup as well as the basic principles.

The tokamak itself is a ”doughnut” shaped vacuum vessel, in which ionized gas is used as the secondary winding of a transformer. Due to the current, the plasma is heated and a magnetic field is induced into the poloidal direction around the current (e_θ) namely the so-called poloidal magnetic field B_θ. In order to obtain a reasonable particle confinement an additional toroidal field B_ϕ is applied along (e_ϕ) the torus via external field coils together with a vertical magnetic field B_v for plasma shaping and position control.

The basic idea hence can be described quite simply. The plasma pressure needs to be balanced by the magnetic pressure. The plasma pressure itself exerts an a force in the radial direction while the poloidal magnetic field counteracts this by a radially inwards oriented magnetic force. This in then complemented by toroidal and vertical fields to control the plasma position and shape [Wesson 97].

2.1.1 Confinement

As has been described above, the particles are confined to the magnetic field. Despite this fact the whole confinement concept is far more complex. Including particle drifts, anomalous transport and other effects and instabilities which arise from the magnetic confinement idea one has to draw a far more detailed picture.

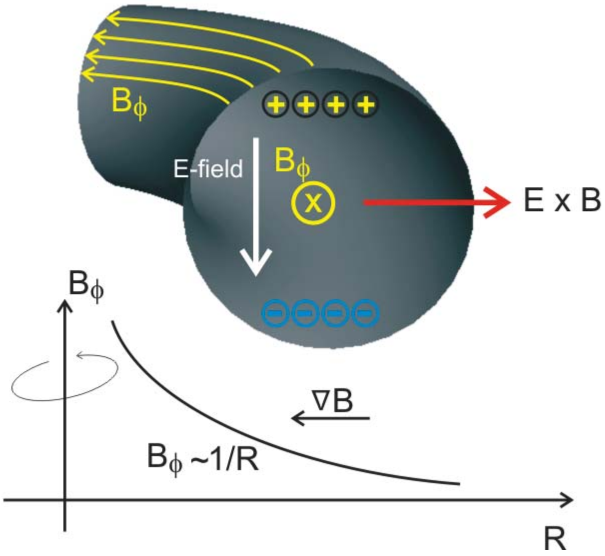

Figure 2.2: Particle drifts in a toroidal magnetic field configuration

Particle Drifts

Particle drifts are the crucial ingredient to understanding, even in a simplified single particle approach, the motions in tokamak plasmas, and hence understanding the confinement principles and the transport phenomena (sec. 2.1.2).

Under the influence of a force perpendicular to the magnetic field, particles are subject to certain drift motions given in a general form as

$$\vec{v_D} = \frac{\vec{F} \times \vec{B}}{q \cdot B^2} \tag{2.1}$$

The most prominent drift motions are determined via equations 2.2-2.4 (cf. [de Blank 08]).

$$\begin{aligned}
\vec{v}_R + \vec{v}_{\nabla B} &= \frac{m}{qB^3}(v_\parallel^2 + \frac{1}{2}v_\perp^2)\vec{B} \times \nabla B \qquad (\nabla\text{B drift}) && (2.2)\\
\vec{v}_{\vec{E}\times\vec{B}} &= \frac{\vec{E} \times \vec{B}}{B^2} \qquad (\text{E}\times\text{B drift}) && (2.3)\\
\vec{v}_{\nabla p} &= -\frac{\nabla p \times \vec{B}}{qnB^2} \qquad (\text{diamagnetic drift}) && (2.4)
\end{aligned}$$

To explain the necessity of a helical field structure for the magnetic confinement in a tokamak one can start with the assumption of only a toroidal field being present which is generated by the external coils (2.1).

This field has distinct curvature causing on the one hand a centrifugal force operating on the particles following the field line and on the other hand causing a gradient in the magnetic field from the innermost parts of the torus to the outer edge. Both forces combined are described in eq. 2.2 and lead to a charge separation between the positively charged ions and the negatively charged electrons.

This charge separation leads to the build up of a vertical electric field, which in turn will, according to eq. 2.3, cause all particle to be expelled from the confined volume as can be seen in fig. 2.2.

A poloidal field added to this setup will lead to a good toroidal confinement, and in turn to the already mentioned helical flux surfaces. [Weynants 08, de Blank 08]

Magnetic Topolgy

In the course of the work the terms flux surface and safety factor will be used more than once, and since it is an essential part of what the tokamak physics is made of, the following section will introduce the idea of magnetic flux surfaces, the nested structures common for the tokamak and the so-called safety factor q quantifying the helicity of the magnetic field line.

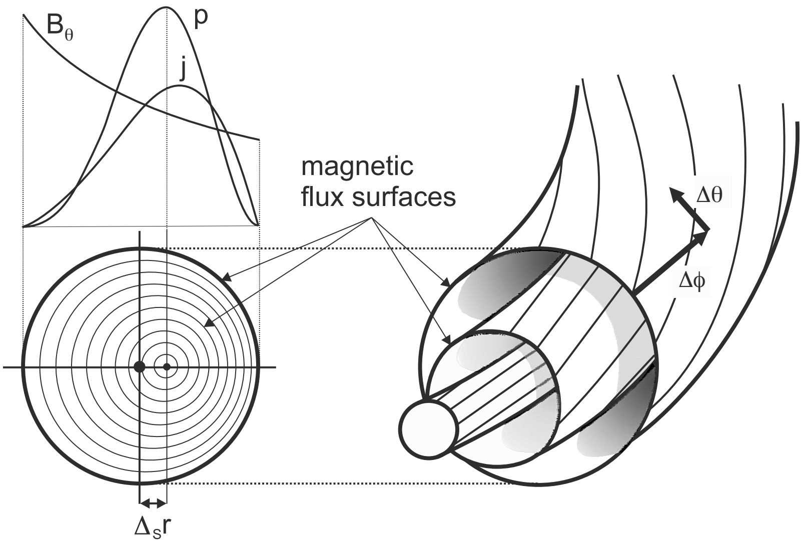

Figure 2.3: Nested flux surfaces in a toroidally and poloidally symmetric geometry (Limiter Tokamak) as well as pressure and current profile together with the Shafranov shift

Based on the balance of magnetic pressure and plasma pressure ($\vec{j} \times \vec{B} = \nabla p$) one can deduce the concept of the so-called flux functions, quantities that are constant on the flux surfaces.

One typically assumes an axisymmetric magnetic field which can be written as

$$\vec{B} = B_R \vec{e_R} + B_\phi \vec{e_\phi} + B_z \vec{e_z} \tag{2.5}$$

where the poloidal part can be expressed as

$$\vec{B_\theta} = B_R \vec{e_R} + B_z \vec{e_z} = \nabla\phi \times \nabla\Psi \tag{2.6}$$

It can be shown [Helander 01] that due to the structure of the magnetic fields the poloidal flux function

$$\Psi = RA_\phi(R, z) \tag{2.7}$$

is constant along the helical field lines and thus leads to so-called flux surfaces. ϕ is the toroidal flux function.

For the confinement the pressure balance must be satisfied which automatically means that no current can flow across flux surfaces and the pressure needs to be constant on flux surfaces $p = p(\Psi)$ based on equation $\vec{j} \times \vec{B} = \nabla p$.

$$\begin{aligned} \vec{B} \cdot \nabla p &= 0 \qquad (2.8) \\ \vec{j} \cdot \nabla\Psi &= 0 \qquad (2.9) \end{aligned}$$

The typical setup as observed in a tokamak is displayed in fig. 2.3. The complete magnetic field produces a set of nested flux surfaces with embedded field lines following the above discussed helical structure. The direction of the field lines changes from surface to surface, which is described by the so-called safety factor q.

A feature shown also in figure 2.3 is the Shafranov shift $\Delta_s r$ which accounts e.g. for the shape of the plasma pressure being peaked close to the plasma center and determines the structure of the flux density of the magnetic field.

Safety Factor q

The so-called safety factor q can be defined as the average change in the toroidal coordinate ϕ over the change in the poloidal coordinate θ along the magnetic field.

The safety factor can hence be written as

$$\begin{aligned} q(\Psi) &= \frac{\langle \vec{B}\nabla\phi \rangle}{\langle \vec{B}\nabla\theta \rangle} \qquad (2.10) \\ &\text{or} \qquad (2.11) \\ q(r) &= \frac{\Delta\phi}{2\pi} \approx \frac{rB_\phi}{R_0 B_\theta}. \qquad (2.12) \end{aligned}$$

The safety factor q is also a measure for the number of toroidal turns when performing one poloidal turn, which is displayed in fig. 2.4. A field line on a flux surface with in this case a

(a) q=1 (b) q=2 (c) q=3

Figure 2.4: Helical field line on different rational flux surfaces

certain rational value of q while staying on this flux surface ends up in itsself an infinite number of times.

This safety factor and flux surfaces are playing a very important role when considering external magnetic perturbations (cf. chapter 3) either from intrinsic error fields or externally applied perturbations like the Dynamic Ergodic Divertor [Finken 99b].

There are basically two types of flux surfaces, firstly the ones with $m/n \in \mathbb{Z}$ an irrational number like $\sqrt{\frac{a+1}{a}} \quad \forall\, a \in \mathbb{N}$ where the magnetic field lines fill the whole flux surfaces and secondly the ones with $m/n \in \mathbb{Q}$ where the field lines cross the same point on the flux surfaces over and over again (cf. 2.4).

The rational q-surfaces are prone to resonant effects and hence are called resonant flux surfaces. The position of such flux surfaces to e.g. the DED coils will determine whether and how they are influenced. Field lines with low m and n numbers are more influenced by such resonant effects, since they will interact again and again on a short timescale.

The flux surfaces with irrational q in turn are robust against such influences since the field lines will never cross the same point in space twice and hence will not get in resonance.

2.1.2 Transport Regimes & Collisionality

As we have seen in the last section, the movement of the charge particles is bound by the magnetic field and confined to the magnetic flux surfaces. To understand the imperfections in the plasma confinement it is necessary to consider a particle and heat transport perpendicular to the flux surfaces (cf. sec. 2.1.1). The charge particles are bound to the magnetic surfaces, but since they are subject to a gyro-motion and hence collision with particles from other surfaces, they are able to move radially.

This is called the classical transport in the cylindrical approximation and the typical scale length for this diffusive regime would be the gyro or Lamor radius.

Since the tokamak can not be simply described in cylindrical geometry other effects like the above mentioned drifts become relevant. One can take into account two types of particles, one

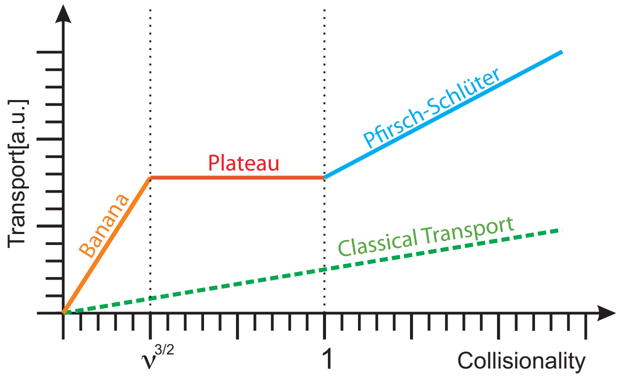

Figure 2.5: Neoclassical transport regimes given in their dependence on the collisionality in comparison to classical transport

with a high and one with low ratio of $\frac{v_{\parallel}}{v_{\perp}}$. The first are abled to move freely along the magnetic field lines and the latter are underlying a magnetic mirror effect due to the difference in magnetic field between the inner torus side (High Field Side) and the outer part of the torus (Low Field Side). This leads to a oscillatory movement, which than in turn is distorted to a so-called banana orbit due to the inhomogeneous magnetic field and the resulting drift motion.

This kind of transport is called neoclassical transport and can be characterized via the so-called collisionality, given by the collision frequency $\nu_{coll.}$ and the transit frequency $\nu_{trans.} = \frac{v_{\parallel}}{qR_0}$. The collisionality is comparable for electrons and bulk ions since $\frac{\nu_{ee}}{\nu_{v_{\parallel e}}} \sim \frac{v_{ii}}{v_{\parallel i}}$ [Helander 01], while highly charged ions are more collisional than the bulk ions. The collisionality without mass dependence can be written as

$$\nu^* = \frac{\nu_{coll.}}{\nu_{trans.}} = \frac{\nu \cdot q \cdot R_0}{\epsilon^{3/2} \cdot v_{\parallel}} \tag{2.13}$$

with ν the collision frequency and ϵ the measure for the inverse aspect ratio r/R_0 at the observed location. $v_{\parallel}$ is the measure for the parallel thermal velocity along the magnetic field lines.

One can separate three transport regimes via their specific values of collisionality, as visible in fig. 2.5.

The high collisionality regime, also called Pfirsch-Schlüter or fluid regime with $\nu^* \gg 1$, where a typical thermal particle can not complete a single orbit without being disturbed by collisions.

In the case small aspect ratio and $\nu^* \ll 1$ one speaks of the combined banana-plateau regime, typical for the core of a tokamak where the orbits of particles are generally completed. If the aspect ratio is large compared to unity this regime is divided into the banana and the plateau regime. Where in the plateau regime most particles are completing their orbits while in the plateau regime both kinds of behaviors are equally probable.

Even though the last section on tokamak confinement and transport gives a quite well theoretical approach, the actual confinement is not as good as it should be from the theoretical point of view [Wesson 97], we have already seen the difference between the classical transport and the neoclassical transport in the toroidal geometry, but the transport is even higher due to the so-called anomalous transport. This anomalous transport is caused by micro-instabilities in the plasma like small scale temperature and density variations, in turn causing turbulence and enhanced transport.

2.1.3 Energy and Particle Exhaust - Limiter vs. Divertor

The last sections have been dedicated to the description of particle and energy confinement due to the applied magnetic fields and some basic transport description. The question remains how to deal with the plasma boundary which will of course at some point have to have contact to the first wall.

The exhaust of particles and energy is one of the crucial issues connected to nuclear fusion devices. On the one hand is it necessary to keep the heat load to the wall materials at a reasonable value in order to ensure high component lifetime and, on the other hand, it is vital that the plasma is not contaminated by impurities originating from plasma-wall interaction.

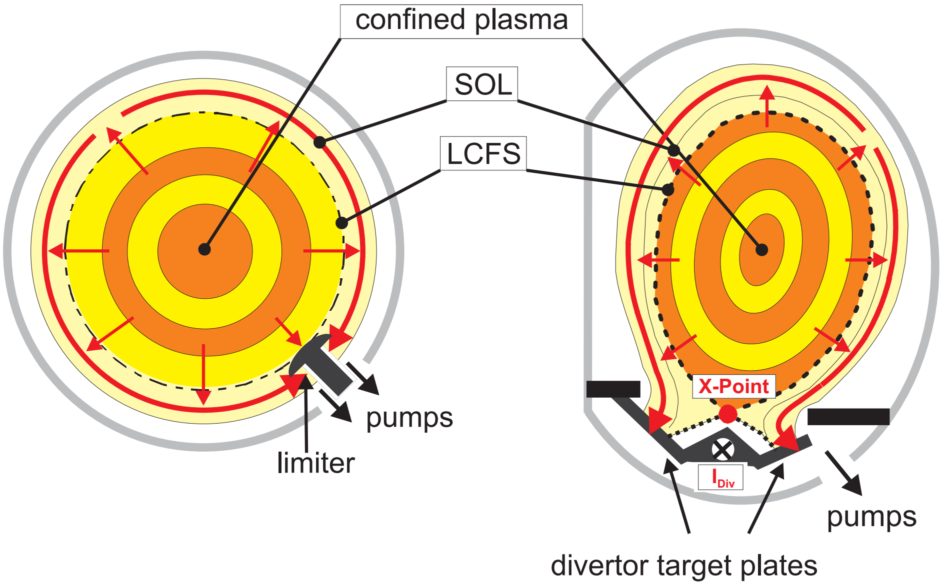

Figure 2.6: Particle and Energy exhaust concepts; Plasma boundary magnetically (divertor) or mechanically (limiter) constraint

One of the more important issues are the exhaust of fusion products and concepts regarding refueling of the plasma with deuterium an tritium (hydrogen).

In the following section a short description of the two more common configuration is given, of which the divertor has proven to be the more promising (Divertor H-Mode [Wagner 82]). A more detailed description of these concepts can be found in the work of Stangeby [Stangeby 00].

Figure 2.6 displays both concepts, the limiter configuration on the left and the divertor configuration on the right side. Clearly visible are the differences between the two concepts, while the limiter configuration is shaping the plasma with means of a mechanical limiter the divertor is using additional coils, shaping the magnetic field in a way such that the outermost field lines are bent onto the divertor target.

In both case one moves from the confined plasma region over the last closed flux surface (LCFS) into the so-called scrape off layer (SOL).

In cases of the limiter configuration the magnetic field lines end on the limiter and lead particles and energy into the SOL. Straight opposite to the Limiter there is the so-called stagnation point which defines the direction along which all particles, heat and energy flow towards the limiting element where the particles can then be neutralized and pumped away. At the stagnation point itself the velocity is zero. The SOL has an extension of a few centimeter in radial direction and features exponential decay of the plasma parameters.

Whereas the limiter configuration presents a very direct connection between the hot core plasma and the SOL, hence putting much stress on the limiting elements, the divertor configuration presents a much better way to decouple the plasma exhaust from the core plasma.

As can be seen in fig. 2.6 a current is running through an additional coil, thus deforming the magnetic surfaces. An x-point is forming where the diverting and the main magnetic field are compensating. The field lines are now diverted into a separated volume, the divertor, where they will be neutralized and pumped away. This method leads to strong separation between the main plasma and the divertor volume, allowing for a better suppression of back spill of neutrals into the plasma. The divertor concept is what is nowadays mostly considered for future tokamak devices such as ITER and DEMO [Aymar 02, Horton 08].

The Scrape-Off Layer

In order to be able to understand the edge behavior of the toroidal and poloidal rotation, presented in chapter 6, a short introduction into the aforementioned SOL is given in the following section. Since the SOL is rather small in comparison to the minor plasma radius ($\lambda < a$) one can use a simplified approach to describe the SOL, by straightening the SOL into a two dimensional

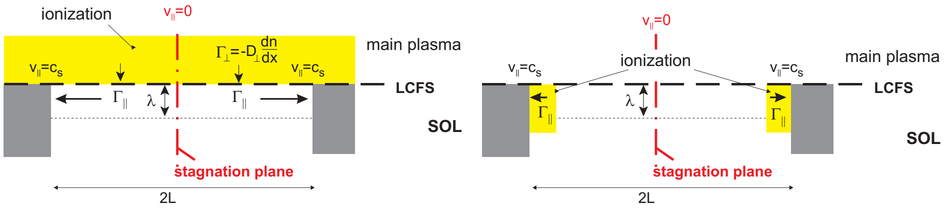

(a) Simple SOL

(b) Complex SOL

Figure 2.7: 2-d model of the SOL, (a) a simple SOL filled via crossfield diffusion $D_{\perp}$ and (b) the complex SOL with the ionisation taking place near the target.

picture as given in figure 2.7. The particle flow is in general along the field lines in z-direction, while the radial diffusion is described as being in the x-direction.

One general distinguishes two models, the simple SOL as shown in 2.7(a) and the complex SOL given in figure 2.7(b). While the simple SOL models mostly holds true for the so-called Limiter configuration assuming the ionization taking place inside the plasma the complex model is valid for the divertor configuration, with the ionization taking place inside of the SOL near the target.

In principle the electrons will rush to the target and build up a negative potential with the characteristic length being the Debye length

$$\lambda_D = \sqrt{\frac{\epsilon_0 k T_e}{n_e e^2}} \tag{2.14}$$

which in principle now builds a thin shielding sheath.

In any case the shielding is not perfect and the thermal motion of the plasma particles is sufficient to penetrate the sheath and accelerate the ions towards the target. Due to a pressure gradient towards the target a symmetric flow is developed toward both ends which at the stagnation points has no velocity in parallel direction while it reaches sound speed at the target (”Bohm criterion”). This flow is one of the boundary conditions for plasma rotation close to the edge and can be observed through radial coupling in the edge plasma rotation.

The symmetry of the flow can be removed by drift motions due to the electric fields or pressure gradients normal to the magnetic field direction. For more details see [Unterberg 08, Stangeby 00].

2.2 Plasma Rotation and Radial Electric Field

The following section will give the necessary theoretical approaches to get an understanding of the plasma background and impurity rotation, meaning the rotation of the deuterium plasma and the rotation of impurity species which due to different charge mass and coupling may very well rotate differently from the background. Plasma rotation, in this work the impurity rotation, is the main ingredient in determining the radial electric field from the radial force balance as discussed in some detail in section 2.2.3.

2.2.1 Background Rotation

As is described in Section 2.1.1 a simple picture of single particle movement can already be given by the application of particle drifts due to the gradients in pressure and magnetic field or other perpendicular forces.

Since the plasma cannot simply be seen in the single particle approach one can only describe the plasma rotation on the basis of the fluid equations, namely the single fluid model, incorporating ions and electrons.

$$n_i m_i \frac{d\vec{v}_i}{dt} = \underbrace{n_i e(\vec{E} + (\vec{v}_i \times \vec{B}))}_{\text{Lorentz force}} - \underbrace{\nabla \cdot \mathbf{\Pi_i} - \nabla p_i}_{\text{viscosity \& pressure}} + \underbrace{\vec{F}_i}_{\text{ext. forces}} + \underbrace{\vec{R}_{i,e}}_{\text{friction}} - \underbrace{n_i m_i \nu_{i0} \vec{v}_i}_{\substack{\text{collisions} \\ \text{(CXRS friction)}}} \tag{2.15}$$

$$n_e m_e \frac{d\vec{v}_e}{dt} = -n_e e(\vec{E} + (\vec{v}_e \times \vec{B})) - \nabla \cdot \mathbf{\Pi_e} - \nabla p_e + \vec{F}_e + \vec{R}_{e,i} \tag{2.16}$$

$$\frac{d\vec{v}_a}{dt} = \frac{\partial \vec{v}_a}{\partial t} + \vec{v}_a \nabla \cdot \vec{v}_a \ \ , \ \ a\epsilon\{i, e\} \tag{2.17}$$

In the following discussion we concentrate on the approach presented in [Chen 85, Helander 01, Rozhansky 96, Cornelis 94] starting on the momentum balance equation describing the force density for electrons (e) and ions (i) as given in the equations above. n_a, m_a and v_a are describing the density, mass and velocity of electrons and ions ($a\epsilon\{i, e\}$).

While the first term on the right side describes the well known forces (given in terms of the force density) operating on charged particles in electric and magnetic fields (Lorentz force) the other terms introduce the viscosity tensor Π_a, the friction between the two species ($R_{i,e} = -R_{e,i}$), the external force F_a and a collisional term for the ions reflecting the friction caused by thermal neutrals in the plasma edge interacting via charge exchange with the plasma ions. Typical external forces on ions are the external momentum input due to neutral beam heating, while during the further development of the formalism, external forces on electrons will be neglected. From equations 2.15 & 2.16 one can readily deduce the single fluid equation when representing the mass and velocity by m_i and v_i and assuming a quasi neutral plasma ($n_e = n_i$), following [Cornelis 94, Rozhansky 96].

$$\rho \frac{d\vec{v}_i}{dt} = \vec{j} \times \vec{B} - \nabla \cdot \mathbf{\Pi_i} - \nabla(p_e \ + \ p_i) + \vec{F}_i - n_i m_i \nu_{i0} \vec{v}_i \tag{2.18}$$

Here ρ is the plasma mass density ($\rho \approx m_i n_i$). Electron inertia as well as viscosity have been neglected, while the electric field and friction cancel out.

In order to obtain the poloidal and toroidal equations of motion for the plasma one multiplies equation 2.18 with the magnetic field $\vec{B}$ and utilizes a so-called flux surface average ($\langle\rangle$) as described in [Rozhansky 96, Helander 01, Cornelis 94] and ends up with the following equations

$$(1 + 2q^2) n_i m_i \frac{dV_\theta}{dt} = -\langle j_r \rangle B_0 - \frac{\langle \vec{B} \cdot \nabla \mathbf{\Pi} \rangle}{\Theta B_0} + F_\theta - 2q\langle F_\phi cos\theta \rangle - (1 + 2q^2) m_i n_i \nu_{i0} \vec{V}_\theta \tag{2.19}$$

$$n_i m_i \frac{dV_\phi}{dt} = \Theta \langle j_r \rangle B_0 + F_\phi - m_i n_i \nu_{i0} \vec{V}_\phi \tag{2.20}$$

$$\text{with} \quad \Theta = \frac{B_\theta}{B_\phi}. \tag{2.21}$$

A feature visible in those equations is the connection between toroidal and poloidal rotation ($V_{\theta,\phi} = \langle B_0 / B\phi v_{\theta,\phi} \rangle$, flux surface averaged velocities).

A toroidal force e.g. neutral beam injection can lead to a spin up in poloidal rotation, while a purely poloidal force does not cause a poloidal spin up in a straightforward way [Helander 01]. Another implication from the formula is the factor $(1+2q^2)$ which connects the rotation in both direction, so the plasma can not rotate separately but connects both components via the flux surfaces.

$$\frac{\langle \vec{B}\cdot\nabla\Pi\rangle}{\Theta B_0} + F_\theta = \alpha(V_\theta - V_\theta^{neo}) \tag{2.22}$$

$\frac{\langle \vec{B}\cdot\nabla\mathbf{\Pi}\rangle}{\Theta B_0}$ is the viscous force and can, according to [Cornelis 94, Rozhansky 96], be approximated as given by equation 2.22 with α the viscosity and V_θ the neoclassical poloidal rotation.

$$\begin{aligned} \alpha &= \frac{\sqrt{\pi}}{2}\cdot\frac{qv_{th}}{R}m_i n_i \quad \text{(Plateau-Regime)} && (2.23) \\ V_\theta^{neo} &= \frac{k}{eB}\frac{dT_i}{dr} \qquad\quad \text{(Plateau-Regime, k=-0.5).} && (2.24) \end{aligned}$$

This description holds as long as the poloidal velocity is well below the thermal ion velocity $v_{th} = \sqrt{2k_B T/m_i}$ and is derived under the assumption of stationary conditions $\frac{\partial}{\partial t} = 0$

From the given formula and assumptions one can now deduce the equations, determining the poloidal and toroidal rotation.

$$\begin{aligned} \alpha(V_\theta - V_\theta^{neo}) &= -\ \langle j_r\rangle B_0 + (F_\theta - 2q\langle F_\phi\rangle) - (1+2q^2)m_i n_i \nu_{i0} V_\theta \quad \text{(poloidal)} && (2.25) \\ &-\ (\frac{\partial}{\partial r} m_i n_i D_\perp \frac{\partial V_\phi}{\partial r}) = \Theta\langle j_r\rangle B_0 + F_\phi + m_i n_i \nu_{i0} V_\phi \quad \text{(toroidal)} && (2.26) \end{aligned}$$

Equation 2.25 is the determining equation for the poloidal rotation, valid under the assumption that the plasma is in stationary conditions and the convective derivative as well as anomalous transport are negligible.

Equation 2.26 is the expression for the toroidal rotation where as commonly proposed a large transport of momentum is introduced (from experimental observation). This transport is described via the anomalous perpendicular viscosity ($(\nabla\Pi)_{an} = \frac{\partial}{\partial r}\eta_{an}\frac{\partial V_\phi}{\partial r}, \eta_{an} = m_i n_i D_\perp$). A typical value for $D_\perp$ is the empirical value $1\ m^2/s$. Due to the strong dampening in the poloidal rotation the anomalous perpendicular viscosity is neglected in the poloidal equation.

Note that in a truly neoclassical approach neither the external force nor the neutral particle dampening are present, which together with the ambipolarity constraint would prohibit toroidal rotation by itself. In an actual experiment toroidal rotation is present, owing mainly to momentum input from an external source like tangential neutral beam heating, which is then balanced into stationary conditions by the above mentioned collision with neutrals (eq. 2.15) as well as convection and the introduced anomalous viscosity.

2.2.2 Impurity Rotation

In case of a typical tokamak plasma, the single fluid description has to be extended, so that besides the background ions (denoted with i), another contribution is taken into account which we call impurities (denoted with Imp.) in effect leading to a three species plasma. The following considerations are of special importance since the measurements, that are discussed, are based on emissions originating from plasma impurities, namely fully ionized carbon.

In this section a short introduction to the poloidal rotation shall be given considering a tokamak plasma with one single impurity ion species based on the calculations performed in [Kim 91].

Beginning with the equilibrium parallel momentum and heat flow balance equations for a primary and impurity ions in eq. 2.29, with $\mathbf{\Pi_a}$ and $\mathbf{\Theta_a}$ here the viscous stress tensors for friction and heat respectively, the rotation in the neoclassical description can be developed. $\vec{F}_{a,0}$ and $\vec{F}_{a,1}$ are denoting the associated friction forces.

$$\begin{aligned} \langle \vec{B} \cdot \nabla \cdot \vec{\Pi}_a \rangle &= \langle \vec{B} \cdot \vec{F}_{a,0} \rangle && (2.27)\\ \langle \vec{B} \cdot \nabla \cdot \vec{\Theta}_a \rangle &= \langle \vec{B} \cdot \vec{F}_{a,1} \rangle && (2.28)\\ & a \epsilon \{i, Imp\} \end{aligned}$$

Poloidal Rotation

For the polidal rotation equation 2.29, 2.30 can be derived, when assuming that the electron contribution to the viscous and friction forces is negligible [Kim 91, Testa 06] and that $E_{\|}$ can also be neglected (cf. toroidal rotation).

$$V_\theta^i = -0.5 \cdot v_{th,i} \rho_i (K_1 \cdot L_{T_i}^{-1}) \frac{|BB_\phi|}{\langle B^2 \rangle} \cdot h \tag{2.29}$$

$$V_\theta^{Imp.} = 0.5 \cdot v_{th,i} \rho_i \left[K_1 + \frac{3}{2} K_2 \cdot L_{T_i}^{-1} - (h - \frac{Z_i}{Z_{Imp}} \frac{T_{Imp}}{T_i}) L_{p_i}^{-1} \right] \frac{|BB_\phi|}{\langle B^2 \rangle} \cdot h \tag{2.30}$$

In these Equations L_{T_i}, L_{p_i} are the gradient lengths for temperature and pressure (e.g. $d(lnTi)/dr$), while $v_{th,i} = \sqrt{2k_B T_i / m_i}$ is the thermal ion velocity and $\rho_i = m_i v_{th,i} / Z_i e B$ the corresponding Lamor radius. In this case [Kim 91] gives a complete description of the interactions between main and impurity ions parametrized in the two collision parameters K_1 and K_2, which both depend on the applicable transport regime (given in [Kim 91]). The factor h describes the possible helicities for the tokamak magnetic field configurations and is $h = -1$ for a typical TEXTOR discharge ($h = sign(B_\phi) \cdot sign(I_p)$) [Testa 06].

2.2.3 Radial Electric Field

The following section will give a short overview on the formalism describing the radial electric field calculated based on the momentum formalism as seen above as well as the shearing of the radial electric field and its relevance for typical confinement regimes [Ida 98]

To start with an obvious statement one should imagine that any kind charge separation will lead to an electric field counteracting this charge separation or to a return current as described in [Stangeby 00, Cornelis 94, Chen 85], as e.g. observed for the $\nabla \vec{B}$ drift in section. 2.1.1.

As part of this work it will be described that, even though the ambipolarity is maintained, during ergodisation experiments a permanent $\vec{j} \times \vec{B}$ force is present, in turn being connected to changes in the radial electric field [Unterberg 07, Busch 05]. In general ambipolarity ($\nabla \vec{j} = 0$) would prohibit this, since $\nabla \vec{j} = 0$ is required for a plasma in equilibrium state.

Assuming the typical 2 species plasma such a current would be written as

$$j = en_i v_i - en_e v_e, \tag{2.31}$$

containing both the electron and the ion contribution.

A violation of the ambipolarity would directly lead to a radial electric field to compensate the charge separation or to the evolution of a compensating current. [Stangeby 00, Cornelis 94].

Also the changes in NBI ion confinement and in particle confinement in general can be connected to the changes in the radial electric field and the rotation.

To understand this, the following section will introduce the two most interesting quantities, the radial electric field and the ExB shear.

The Radial Force Balance

Assuming a stationary case ($\partial/\partial t = 0$) for the momentum balance equations 2.15 & 2.16 (p. 17) and neglecting the force and friction terms discussed one can formulate the **radial force balance** with a diamagnetic contribution as well as contributions from the toroidal and poloidal rotation.

$$\begin{aligned}
E_r &= E_{r(diam.)} + E_{r(pol)} + E_{r(tor.)} && (2.32)\\
E_{r(diam.)} &= \frac{1}{Z_i e n_i}\frac{dp_i}{dr} && (2.33)\\
E_{r(pol)} &= -\, v_{\theta,i} B_\phi && (2.34)\\
E_{r(tor.)} &= v_{\phi,i} B_\theta && (2.35)
\end{aligned}$$

In case of this radial equation convectivity and viscosity can be neglected under the assumption that local variations in density and temperature are small on the scale of the ion Larmor radius ($\rho_i / L_{n_a,T_a}$, $a \epsilon \{i,e\}$) [Rozhansky 96].

This equation is determining the radial electric field given the knowledge about the pressure (p_i), density (n_i) as well as the toroidal(v_ϕ) and the poloidal (v_θ) rotation.

As described in section 2.2.2 the impurity ion rotation might deviate from the rotation of the main ions, but the radial electric field given by equation 2.32, if consistently measured for one species, should be valid universally.

Since E_r is a common property to all ion species it should be possible to determine the field profiles based on main as well as impurity, which has been proven by measurements at machines like the JET Tokamak [Testa 06] and TFTR [Fonck 84] as well as DIII-D [Burrell 94]. For the JET experiments the evaluated values for the radial electric field calculated from deuterium and carbon agree within 15% and within the intrinsic error bars.

The E×B Shearing Rate $\Omega_{\tilde{\mathbf{E}}\times\tilde{\mathbf{B}}}$

Whereas the quantity directly accessible from the radial forrce balance and the plasma rotation and pressure is the radial electric field, the E×B shearing rate is the parameter most noticed with regard to changes in plasma transport.

The shearing rate [Hahm 95, Burrell 97] given as

$$\omega_{E\times B} = \frac{(RB_\theta)^2}{B}\frac{\partial}{\partial\Psi}\left(\frac{E_r}{RB_\theta}\right) \tag{2.36}$$

or

$$\Omega_{E\times B} = \left|\frac{RB_\theta}{B_\phi}\frac{\partial}{\partial r}\left(\frac{E_r}{RB_\theta}\right)\right| \tag{2.37}$$

shows several interesting features. B_θ is the poloidal magnetic field, B_ϕ the toroidal magnetic field and B its amplitude. R describes the major radius.

The term $E_r/B_\theta R$ shows that both the electric field as well as the magnetic field shear are contributing to the final result. Since the lowest order electrostatic potential is a flux function this term is also constant on the flux surfaces, while the term $(RB_\theta)^2/B$ varies. In a strong simplification in order to understand this equation, E_r/RB_θ could be understood as the toroidal angular speed described by standard neoclassical equations [Burrell 97], assuming negligible poloidal and diamagnetic contribution to E_r.

Relevance for Plasma Confinement and Fusion Research

Now that the most quantities are introduced the following paragraphs are used to give a short insight on what is the importance of the radial electric field and the $\vec{E}\times\vec{B}$ shear for tokamak transport and confinement. We will try to give some hints to the data and discussions in later chapters (Section 3.3 & Chapter 6)

As has been pointed out before, the H-Mode [Wagner 82] and similar improved confinement scenarios have driven the success of fusion development in the last 15 years. One major aspect of this research was the developement of models explaining the transition between L-Mode (low confinement) and H-Mode (high confinement). Most of these models [Burrell 97] have in common that they are taking into account changes in the radial elelectric field and especially the $\vec{E}\times\vec{B}$ shearing rate to explain the changes in plasma transport and confinement. The changes in the radial electric field and its gradient are related to changes in the turbulent transport and the growth rates of instabilities [Biglari 90, Burrell 97, Moyer 95]. The radial extent and growth of turbulent eddies in the plasma edge is influenced.

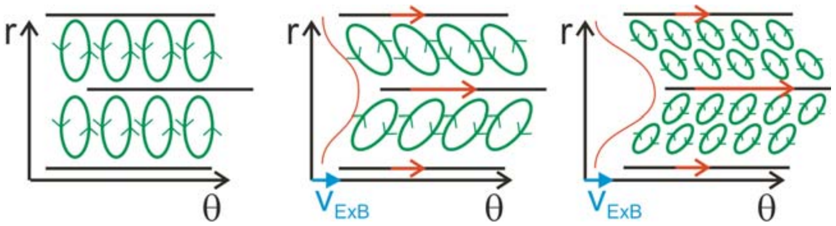

Figure 2.8: Schematic picture of turbulence decorrelation / distortion by $\vec{E} \times \vec{B}$ shear

As shown in figure 2.8 the basic effect is assumed to be the reduction in radial transport due to a decrease in the radial correlation length of fluctuations in density temperature and or plasma potential.

As is described in section 2.2.3, equation 2.32 indicates that the radial electric field can be influenced by altering the plasma pressure, the toroidal or poloidal rotation.

A long list of experiments have been performed to test the connection between $\vec{E} \times \vec{B}$ velocity shear and plasma confinement, including H-Mode edge confinement improvement, VH-modes and ITB discharge experiments [Burrell 94, Synakowski 97, Van Oost 03, Dreval 08].

It was shown that in the L-H transition especially changes in the edge pressure gradient as well as v_θ are observed. Changes in those quantities directly related to changes in the radial electric field and its shear.

Considering all the experiments, the velocity shear seems to have a quite universal character for tokamak confinement. This role is backed up by the theoretical work of Kim [Kim 91], pointing out the crucial role of the $\vec{E} \times \vec{B}$ velocity in the description of plasma fluctuations.

A shear in the $\vec{E} \times \vec{B}$ velocity distorts the flow eddies as depicted above and reduces radial transport. This reduction in radial transport is due to both the change in phase between the velocity and density perturbation and to a decrease in amplitude of the perturbation themselves.

The shearing rate as given in equation 2.36 & 2.37 enters the various stabilization models quadratically, hence the sign is not playing an important role [Stacey 05]. Even though the models still deviate from the measurement data, when comparing the ExB shearing rate with the turbulence growth rates, it seems clear that the radial electric field is the crucial parameter to understand and influence plasma confinement. In general $\omega_{\vec{E} \times \vec{B}} \leq \gamma_{max}$ is used as a the prediction for turbulence suppression.

In chapter 3 the Dynamic Ergodic Divertor is discussed as a tool to influence plasma transport in the edge as well as a means of changing the radial electric field by influencing the plasma rotation. The suppression of turbulent transport [Xu 06, Kramer-Flecken 06] as well as the spin-up of rotation [Finken 01, Finken 05b, Busch 06, Unterberg 07] have been observed under the influence of the DED. This will be complemented in chapter 6, where the use of the DED is demonstrated, causing two distinct scenarios to emerge, one with improved particle confinement, the so-called improved particle confinement scenarios and one with decreased particle confinement, the so-called particle Pump Out scenario [Coenen 08, Schmitz 09].

Chapter 3

TEXTOR and The Dynamic Ergodic Divertor (DED)

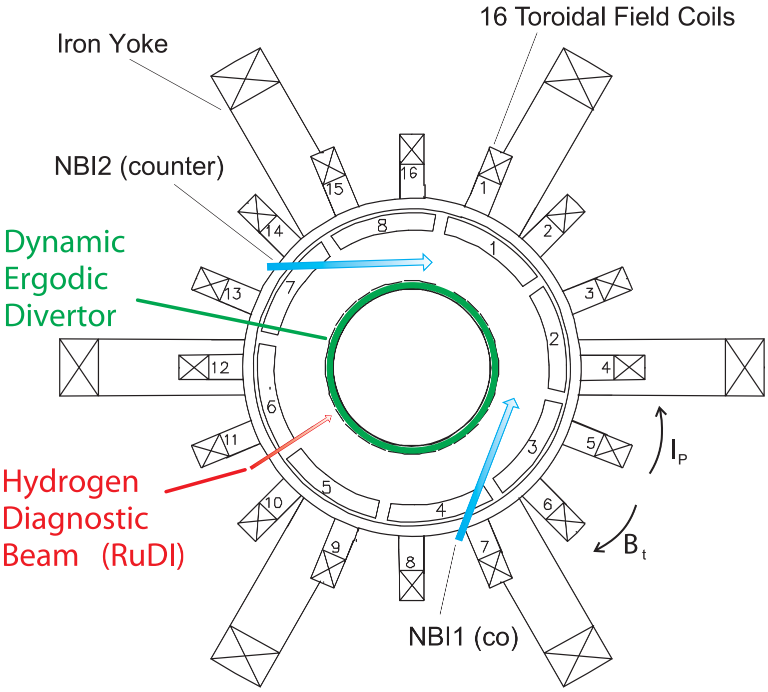

Figure 3.1: Top View of TEXTOR. Directions given for standard conditions. NBI=Neutral Beam Injector.

TEXTOR-DED stands for the combination of the limiter tokamak TEXTOR (Torus Experiment for Technolgy Oriented Research) [Neubauer 05] and a set of perturbations coils mounted inside of the tokamak vessel, the Dynamic Ergodic Divertor (DED) [Finken 99b].

3.1 The Tokamak TEXTOR

TEXTOR is a medium size Tokamak operated at the "Institute for Energy Research - Plasma Physics, Forschungszentrum Jülich GmbH". TEXTOR is the experiment of the Trilateral Euregio Cluster and has been operated since 1982. During the lifetime of TEXTOR additions to the experimental setup have been performed, e.g. the installation of the Dynamic Ergodic Divertor in 2002, which plays the crucial role in the work presented here.

The experimental setup is displayed in fig. 3.1, which shows an overview of TEXTOR, including some of the major components e.g. the toroidal field coils, the neutral heating beams and the diagnostic hydrogen beam RuDI.

3.1.1 Setup and Operational Parameters

In contrast to most present day devices TEXTOR is a limiter tokamak, with a minor radius of the plasma column of about $47\,\mathrm{cm}$. The major radius is given as the distance from the center of the primary solenoid to the center of the liner, the inner metal wall, and has a value of $\mathrm{R} = 1.75\,\mathrm{m}$.

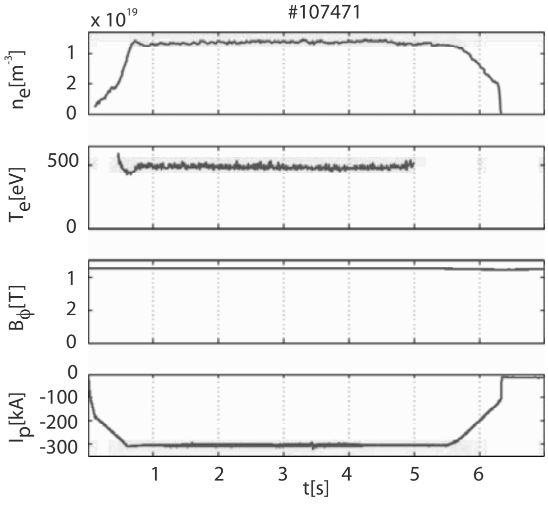

Figure 3.2: Typical TEXTOR discharge, #107471, showing the plasma current (I_p) and the toroidal magnetic field (B_ϕ) as well as the line averaged electron density (n_e) and temperature of the plasma(T_e).

The setup consists of a primary transformer solenoid with an iron core and a six legged iron yoke (cmp. fig. 3.1), a set of 16 copper toroidal field coils and a stainless steel vacuum vessel. As mentioned before, inside of the vacuum vessel a so-called liner is mounted. Its is heatable and equipped with several openings for the diagnostic ports. It gives the opportunity to use the inner wall quite flexibly, e.g. mounting different wall components to test new wall materials.

TEXTOR like every tokamak is an axisymmetric machine, with a circular plasma. This symmetries hold true up to the plasma edge where the nature of the topology is more a three dimensional one than simply 2D [Schmitz 08b]. In any case reversing the plasma current and magnetic field should in turn just reverse the rotation and drift directions and hence mirror the machine. The one exception to this rule is the ALT-II limiter belt limiter. Since the ALT-II limiter is fixed at the bottom of the machine (at 45°) with a radial position of r=46.6 cm, its position can have implications on plasma rotation and flows in the plasma edge.

Apart of the ALT-II limiter two poloidal limiters are mounted at the top and the bottom of the machine which can be moved into the plasma when required. An overview of the specifications is given in table 3.1.

The central solenoid is able to induce a current into the plasma between 0.2 and 0.8 MA, while the typical operational window lies around 350kA. The toroidal magnetic field ranges up to 3.0T and is being sustained during the whole discharge.
Depending on the plasma current the discharge has a maximum duration of up to 10 seconds, while a typical flat top phase is in the order of 5 s.

Parameter	Value
Plasma boundary	Limiter / DED
Major plasma radius	1.75 m
Minor plasma radius	0.47 m
Plasma shape	circular
Plasma volume	7 m^3
Number of TF coils	16
Magnetic Field (max)	3.0 T
Plasma current (max)	0.8 MA
Pulse length (max)	10s
Installed heating power	9 MW
Heating systems	NBI, ICRH, ECRH

Table 3.1: Parameters of the TEXTOR tokamak [Neubauer 05]

The line-averaged density depends on discharge and machine conditions; it ranges from $0.9 \cdot 10^{19} m^{-3}$ to $10 \cdot 10^{19} m^{-3}$, while typical electron and ion temperatures are in the range of keV in the core and $\sim 100eV$ in the plasma edge (fig. 3.2).

3.1.2 Diagnostics & Heating

TEXTOR is equipped with a large set of diagnostics, either for plasma and machine control or for scientific purposes. Several heating systems are available to supply additional energy to the plasma [Neubauer 05]. The diagnostics include magnetic pickup coils, ECE imaging, HCN laser interferometry, Microwave reflectometry, thermal beams, active beam spectroscopy

(CXRS), optical spectroscopy, Soft-Xray spectroscopy, VUV spectroscopy, optical overview cameras and many more [Donne 05, Brezinsek 05a]. The HCN interferometer as well as the magnetic diagnostics are integral part of the plasma density and position control scheme, while the other diagnostics are mainly used for physics purposes, density measurements (ion, electron), high resolved rotation measurements, impurity studies and more.

To reach and maintain a viable high confinement fusion plasma external heating is necessary to drive the transition from so-called L-Mode (Low) to a higher confinement stage (H-Mode). In case of the TEXTOR tokamak three main systems are installed.

Neutral Beam Heating is supplied via two tangentially mounted 45 to 60 V, 100A hydrogen (deuterium) beams which can inject a power of up to 2 MW each(fig.3.1). TEXTOR has two systems of Cyclotron heating ([Koch 08]), a set of two pairs of ICRH (Ion Cyclotron Resonance Heating) antenna and one gyrotron for suppling ECRH (Electron Cyclotron Resonance Heating). Both systems can add another 5 MW in total.

3.2 The Dynamic Ergodic Divertor

The Dynamic Ergodic Divertor (DED), installed at TEXTOR in 2002, is a flexible tool to control and study the behavior of the plasma edge properties under the influence of an external magnetic perturbation field in resonance with the tokamak field [Finken 99b, Finken 04]. It is also introducing a divertor concept based on the generation of a ergodic boundary layer [Schmitz 08b].

Setups similar to the DED have been applied at Tore Supra [Ghendrih 96], and by use of existing correction coils at Jet and DIII-D [Evans 06a, Liang 07] and have proven to be a powerful tool to control power and particle transport in the plasma edge, including suppression of harmful edge modes [Evans 06b].

Beginning with the early phase of development of the DED several theoretical and modeling approaches as well as intensive experimental measurements have been performed to understand the interaction of DED with the tokamak plasma [Lehnen 05b, Lehnen 05a, Schmitz 07, Abdullaev 03, Finken 05a] and compare the calculated magnetic topologies with the actually measured quantities like plasma density and temperature as well as heat flux patterns on the DED target [Schmitz 08b, Jakubowski 04b].

On the following pages a short overview on the DED setup and its operational parameters shall be given followed by a simple description of the magnetic topologies and regimes accessible with the DED. In the end a short theoretical overview will be given in order to later connect observed effects with the their theoretical counterparts.

3.2.1 Setup and Parameters

The DED consists of 16 helically wound perturbation coils mounted on the High Field Side (HFS) of TEXTOR ($+2$ additional compensation coils). Those coils ($1 \leq j \leq 16$) can be seen in the left part of fig. 3.3. They are mounted at a minor radius of $r = 0.535$ m and cover a poloidal range of about 72°$(2 \times \theta_c = 80°$ incl. compensation coils). The coils are mounted in such a way that they are aligned with the pitch angle of the field lines on the $q = 3$ surface at the High Field Side (cf. sec. 2.1.1). The ideal coil setup, to produce pitch resonance, is given as such that the coils start at $\phi_j = j\pi/8$ and wind once around the vessel. This means a poloidal angle starting from $\theta_j = \pi - \theta_c$ and ending at $\theta_j = \pi + \theta_c$.

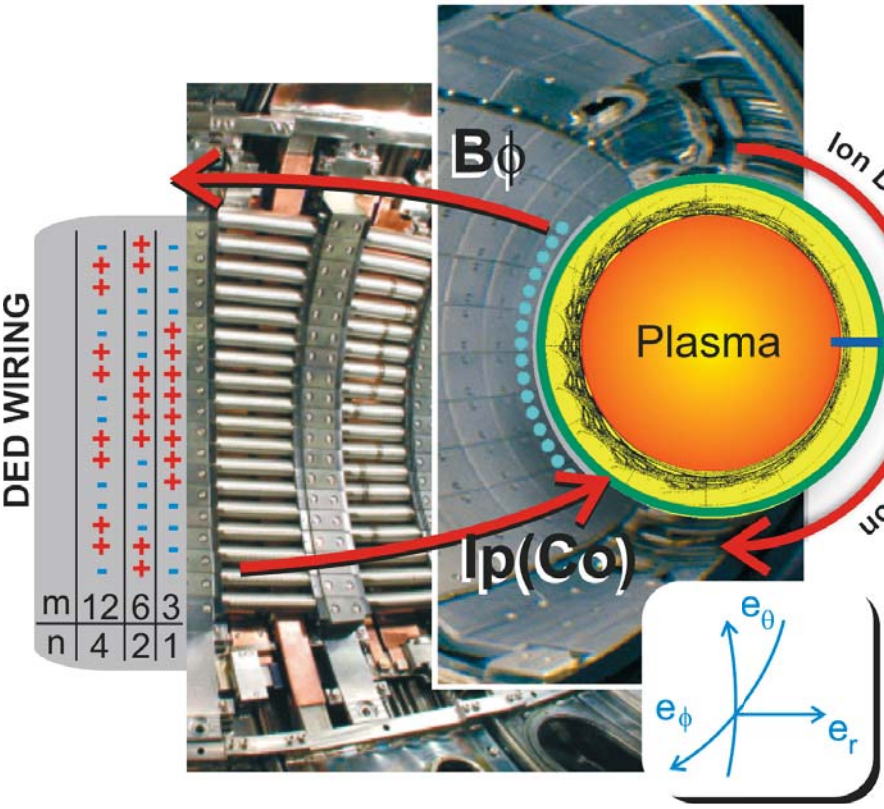

Figure 3.3: Coordinate System under normal TEXTOR Conditions (DED AC+ || electron diamagnetic drift direction (EDD), DED AC- || ion diamagnetic drift direction (IDD)), DED Wiring for different operational modes (sec. 3.2.2)

The coils can be interconnected in several setups, which allows the following DED configurations: m/n 12/4, 6/2, 3/1. m being the poloidal mode number and n the toroidal mode number or the number of toroidal(n) or poloidal(m) turns (cf. figure 3.3). Those configurations have different consequences regarding the magnetic topology and plasma transport which are explained in more detail in section 3.2.2. Each of those configuration has a unique spectrum of modes with different amplitudes.This causes resonances at several of the q-surfaces apart of the main resonance. The coils are protected by a layer of graphite tiles (fig.3.3). A more detailed introduction in the magnetic field and setup of the DED can be found in [Finken 05a].

The DED can be operated in all of the configurations at several amplitudes depending on the connection of the different coils. This causes different perturbation amplitudes with respect to the different mode spectra. In addition to normal DC operations, the power supplies are also able to provide a multitude of frequencies between 89 Hz and 10 kHz.

While in the 3/1 mode four neighboring coils are combined such that the same current is flowing through them, allowing for $I_{\max}$ of 3.75kA the setup in 12/4 uses each coil separately (cf fig 3.3) allowing for a maximum current of 15kA. The different configurations produce different multipole structures and have different behaviors regarding radial decay and extent as is described in the following section. The 3/1 mode has the most prominent resonances at m=3 and n=1, the other configurations behave according to the defined mode numbers.

In the course of this work mainly the 6/2 DC configuration is considered.

3.2.2 Magnetic Topology of TEXTOR-DED

The magnetic topology and the different operational regimes mostly depend on the position of the resonant q surface with respect to the plasma edge and the DED [Finken 05a]. Even though the typical perturbation $B_{\mathrm{DED}} \lesssim 0.02$T is small in comparison to the main B field ($B_{\mathrm{DED}}/B_{\theta} \lesssim 0.1$ [Finken 05a]) the topological structures can be seen very well in the experiment [Schmitz 08b, Jakubowski 04b] and in the calculations [Finken 05a].

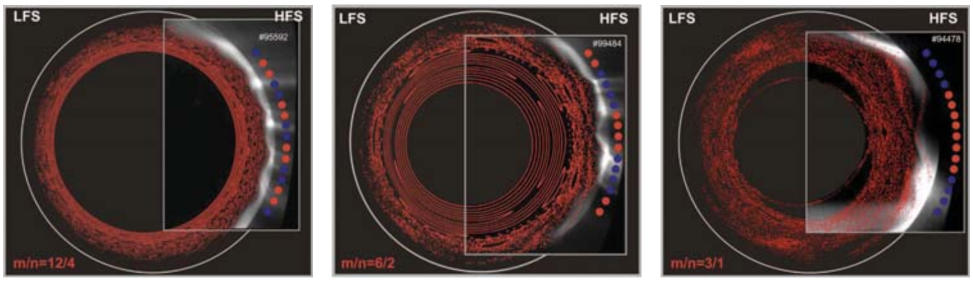

(a) m/n=12/4 @ 11 kA (b) m/n=6/2 @ 7.5 kA (c) m/n=3/1 @ 3.75 kA

Figure 3.4: Poloidal cut through the TEXTOR vessel: DED operational modes - showing the calculated vacuum topology (Poincaré plot) overlayed with the CIII emission of intrinsic carbon impurities.

As an introductory example fig. 3.4 shows a comparison between the calculated magnetic topology (Poincaré Plot see below) and the intrinsic CIII emission (from carbon impurities) gathered via a tangentially viewing camera. The three images show the three different base modes of the DED. The 12/4 mode shows a shallow penetration, only the plasma edge is affected, while in the 3/1 configuration the penetration reaches far into the plasma (half the minor radius). In all cases the CIII emission matches the structures of the near field shown by the topology plots.

Visualization and Modeling

A standardized method is applied to model and visualize the magnetic structures present in the ergodic plasma edge of TEXTOR-DED. Such methods are necessary in order to understand the influences on the particle and heat transport (electrons and ion follow the magnetic field lines).

Codes At TEXTOR two numerical codes are applied. The Gourdon Code [Gourdon 70, Finken 05a] and the ATLAS approach [Abdullaev 99, Jakubowski 04b, Finken 05a], both superimposing the DED field over the two dimensional axissymetric and stationary tokamak field, hence neglecting self consistent reactions of the plasma (see below). Both Codes will be used in this work, in order to present the data in comparison with the magnetic topologies.

The **Gourdon Code** was developed in 1970 and uses the assumption that one can simply superimpose the equilibrium magnetic field and the radial perturbing field. This method exactly describes the field lines, neglecting any plasma response (Vacuum Approximation). The resulting field vector can be used to track the field lines. The interaction between plasma and perturbation is neglected and the screening of the magnetic field is assumed to be negligible.

The code requires the equilibrium fields as well as the fields originating from the external DED coils. While the plasma equilibrium is calculated using the DIVA Code [Zehrfeld 99], the externally applied field is based on the current distribution in the coils and Bio - Savart's law [Biot 20]. The equations of motion are solved in 3 dimensions with numerical integration. The calculations represent the magnetic topology as given by those calculations.

The **ATLAS Code** uses another approach for the calculation of the field line in the vacuum approximation (so-called mapping), it uses a suitable mapping function to allow n-dimenional steps to be performed instead of integrating step by step [Abdullaev 03]. With this approach, it is possible to formulate an analytical solution and hence formulate a mapping between different poloidal cuts [Abdullaev 03, Jakubowski 04a]. This approach is also called ”simplectic maping” [Jakubowski 06]. Both methods can achieve good agreement with the experiments performed at TEXTOR-DED [Schmitz 08b, Jakubowski 04b, Coenen 08], but details are subject to the m/n configuration of the DED. Every configuration has a different spectra and causes different resonance effects depending on the amplitude of the respective modes and amplitudes.

There are two main methods to visualize the results of the above mentioned calculations. The Poincaré and the laminar plot. Both are combined in fig. 3.5 and will be explained in the following paragraphs followed by the different parts of the magnetic topology.

Limitations to the Vacuum Picture As is stated above, both approaches assume the so-called vacuum approximation. While this is so far the only way to judge the measured data in comparison with the theoretical magnetic topology, limitations are known to exist. From measurements at TEXTOR it is known that the m/n=12/4 setup agrees very well with the magnetic calculations, based e.g. on measurements on the DED divertor target footprint pattern [Jakubowski 04b] but the lower modes of the DED can show deviations from the calculations. Especially the effects

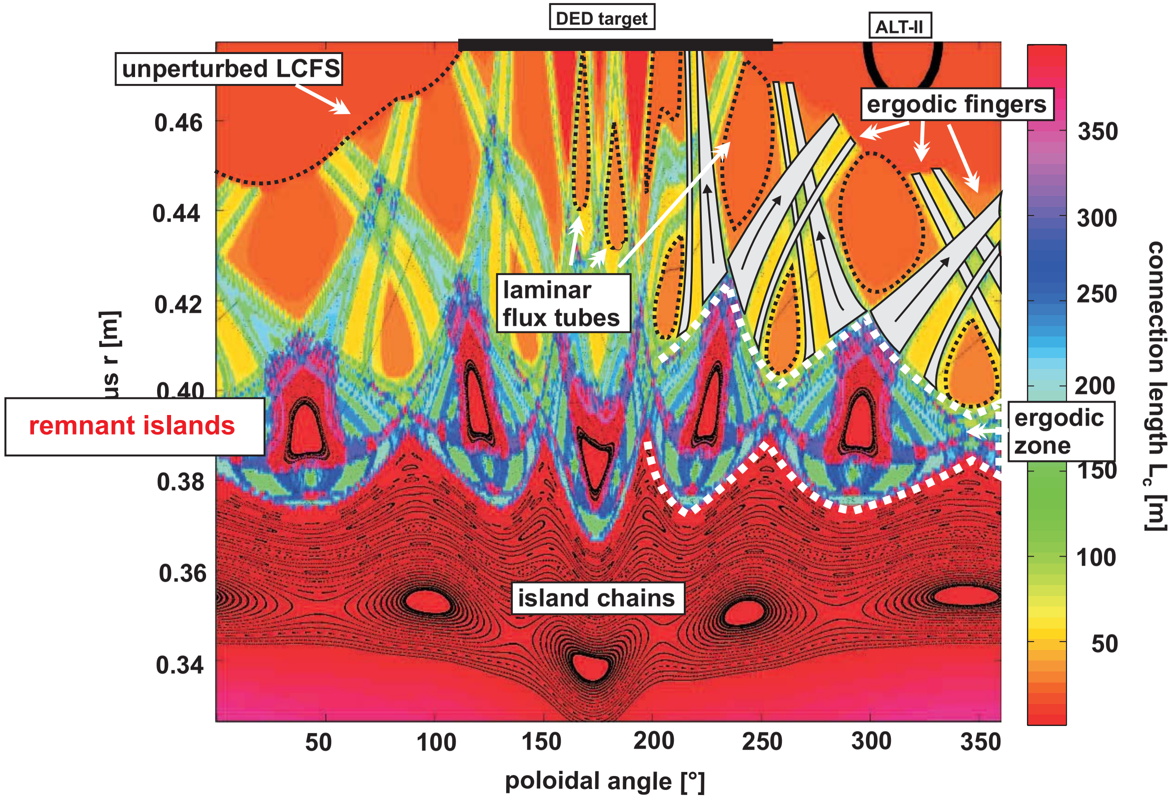

Figure 3.5: An overview of the magnetic topology in the stochastic edge for m/n = 6/2 base mode configuration. Shown here is a superposition of Poincaré (black colored intersection points of the magnetic field lines with the chosen poloidal plane), laminar plot (color coded connection length distribution) and highlighted are the characteristic topological domains [Schmitz 08b] in the r-θ (poloidal) plane.

30 CHAPTER 3: TEXTOR AND THE DYNAMIC ERGODIC DIVERTOR (DED)

during m/n=3/1 setup with its deep penetration into the plasma are likely to deviate from the calculations in vacuum approximation.

Deviations from this vacuum approach are e.g. effects of rotational screening, the more the field is theoretically thought to be penetrating, the more likely is a counter action of the plasma by developing screening currents [Cole 06]. This is similar to the behavior in an electric motor where the rotation is induced due to counteracting forces. In addition effects like resistive and ideal MHD effects, tearing modes [De Bock 08] and resonant field amplification [Reimerdes 06] are also not included in the vacuum approach.

Under TEXTOR conditions, limited low temperature, L-Mode plasmas, those effects are thought not to cause deviation from the vacuum approach at least for the higher perturbation mode numbers.

In order to judge the agreement between calculations and actual magnetic topology in this work the footprint patterns on the DED target are used as is shown in the discussions given in chapter 6. Another way is to actually measure the structures in the plasma, as given in [Schmitz 08b] for the 6/2 and 12/4 setup. For the 6/2 setup discussed here, reasonably good agreement has been shown.

Poincaré Plots are the classical approach (cf. classical mechanics) to visualize the field lines. It takes a poloidal cut, hence reducing the problem of representation by one dimension, and traces one or more field lines, marking each intersection of those field lines with the given poloidal plane. The intersection point is marked with a dot, as shown in fig. 3.4 and 3.5. The field line is either traced to a maximum number of steps or intersects with the divertor target plate at r=47.7 cm, simulating the theoretical end of the field lines and the effects of the DED near field. Fig. 3.4 displays the topology as an overview over the whole 360 degrees. Typically a visualization as in fig. 3.5 is used to better discriminate between the different topology layers (see below).

Laminar Plots are a different approach to topology visualization and one example is shown in fig. 3.5 by the color coding. In contrast to the black dots (Poincaré plot) the color coding is given by the field line connection length (L_c).

The field line is traced from a starting point into both direction until it hits the wall. The connection length to the target is assigned to each point in the poloidal plane. From the connection length a contour plot is calculated as shown in fig. 3.5. One typical use for these calculation next to the poloidal cuts is the representation of so-called footprint patterns on the DED target, where the field lines intersect with the vessel wall [Jakubowski 04b].

Topological Structures and Layers

In the following we will structure the magnetic topology into 4 distinct zones, beginning with the unperturbed core of the plasma and leading to the ergodic edge of the tokamak plasma.

As can be seen in fig. 3.5 the clear distinction in zones or layers is mostly a simplification to describe the features of the more complex structure in a more accessible way (e.g. Ergodic vs. Laminar Zone [Ghendrih 96]).

Unperturbed Flux Surfaces are located in the innermost parts of the plasma (fig.3.5). The magnetic surfaces are structured following the typical onion principle as described in section 2.1.1. The surfaces may be distorted by the external perturbation, but are not yet completely restructured.

Island Chains are areas where the resonant coupling to the external perturbation field causes a radial field line displacement in such a way that the magnetic field lines are sampling magnetic island structures during their movement. The number of islands is determined by the poloidal mode number and their radial and poloidal extent is given by the position of the resonant flux surface with respect to the position of the perturbation coils. The mode spectrum of the perturbation and the q surface at which the external perturbation interacts (compare fig. 3.5, island chains at q=5/2 and 4/2), is crucial to the magnetic topology. Only q-surfaces that are pitch resonant to parts of the applied mode spectrum will be influenced.

”Ergodic Zone” The ergodic zone is the term characterizing a specific part of the ergodic plasma edge. Although the term zone maybe misleading, when comparing to figure 3.5 and the shown complex structure. In general there are ergodic areas with a long connection length L_C as part of the ergodic edge. As long as the connection length is larger then the decorrelation length L_K one can speak about an ergodic zone (see below).

In the following work, we will use a broader approach when using the term ergodic zone. One can assume an island chain where the resonant perturbation is strongest. In case of such an island chain one could reach a situation where the island width $\Delta\Psi_{m,n}$ exceeds the distance between two islands $|\Psi_{m+1,n} - \Psi_{m,n}|$, which can be called the ergodic zone. Three parameters can describe this zone, the connection length, the Kolmogorov length and the Chirikov Parameter.

The island width is a function of the perturbation field components $|h_{m,n}|$ for the relevant poloidal and toroidal mode numbers (m, n) as well as the q profile $q(\Psi)$. With Ψ the Poloidal Flux Function [Finken 05a].

$$\Delta\Psi_{m,n} = 4 \cdot \left| \frac{\epsilon h_{m,n(\Psi)}}{\frac{d}{d\Psi}\, q(\Psi)^{-1}} \right| \tag{3.1}$$

The connection length (L_C) inside the ergodic zone is very large accounting for the stochastic/ ergodic character of the field lines, filling the ergodic volume completely.

The Chirikov Parameter is a measure for the island overlap and is given as

$$\sigma_{Chir} = \frac{\Delta\Psi_{m,n} - \Delta\Psi_{m+1,n}}{2 \cdot |\Psi_{m+1,n} - \Psi_{m,n}|}. \tag{3.2}$$

Where σ_{Chir} exceeds unity, one observes an ergodic field line behavior, which can also be described via the Kolmogorov or field line decorrelation length in the quasi-linear approximation

$$L_K = \pi q R_0 \left(\frac{\pi \sigma_{Chir}}{2}\right)^{-4/3}. \tag{3.3}$$

The ergodic zone at TEXTOR typically covers about 4 cm at the plasma edge depending on plasma parameters and especially the edge safety factor and the poloidal beta [Jakubowski 04b]. The field lines in the ergodic zone are still bundled together, but are stretched and radially displaced.

The Term ergodic field lines can be misleading even though widely used In literature. Field lines with long L_c and decorrelated behavior are generally described as ergodic field lines. However, application of the Hamiltonian formalism requires generation of fixed points which prohibit ergodization of a complete radial domain in the perturbed edge layer. Only specific sub-volumes can be ergodized. Therefore the term stochastic can be somewhat more accurate in some places and is then used.

”Laminar Zone” The laminar zone is the outermost part of the TEXTOR stochastic edge, if speaking in terms of layers. It is characterized by a small connection length, being influenced by the near field of the DED, connecting two parts of the wall via short field line connection length. The Term Laminar Zone applies at a Kolmogorov Length which is larger than the connection length.

If one considers figure 3.5, one ends up with a laminar zone which is quite structured. A Zone consisting of so-called laminar flux tubes with short connection length to the DED target as well as inwrought ergodic fingers with the typical ergodic behavior, elongating the flux tubes with large L_C. While the Laminar flux tubes with short connection length are dominated by parallel transport along the field lines, the stochastic areas (long L_C) feature enhanced radial transport [Schmitz 08b].

All in all the stochastic plasma boundary as depicted and described above is a complex structure with direct influence on particle and heat transport as well as on the confinement. Open field lines are connecting directly to the target.

3.3 Effects of Stochastization & Scenarios

In this section a short introduction into some scenarios accessible with the DED will be given, with a main focus on the so-called improved particle confinement and the opposite scenario, the particle pump out. This will be the motivation and a first insight into the data later discussed in Chapter 6 regarding those two regimes. As another important example the influences by the DED due to the ergodized edge plasma will be discussed by introducing the concept of a j×B force originating from enhanced parallel electron transport.

3.3.1 Edge Stochastization ($\vec{j} \times \vec{B}$ Force)

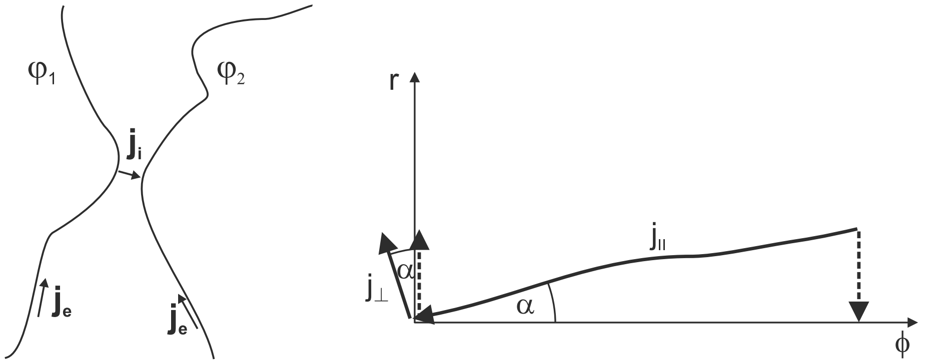

(a) Ergodised magnetic field lines can approach each other. A parallel electron current j_e can hence be compensated by an ion return current j_i

(b) Geometry of currents. Inclined field lines due to radial magnetic components; Perpendicular to the field lines is not anymore the same as radial.

Figure 3.6: Currents in the ergodized edge plasma.

As described above, the stochastic plasma edge produced by the DED consists of several different layers, one being an ergodic zone of some centimeter extent. Already previous experiments at TEXT [Yang 91] with a heavy ion beam probe have observed that, with the presence of an stochastic edge layer, changes to the radial electric field are inevitable.This has been confirmed by Tore Supra by means of spectroscopic measurements on plasma rotation, giving a spin-up in the ion diamagnetic drift direction, hence showing a change in the E_r into the positive direction [Hess 95].

Typicallly the effects observed have been interpreted as an extension of the SOL into the ergodic plasma region [Ghendrih 96] in order to compensate for the enhanced electron transport to the wall.

At TEXTOR we have the ability to change the properties of the ergodization and the strength of the perturbation field by means of the DED base mode numbers and the current amplitude. In all of the DED configurations the effect of rotation spin-up into the ion diamagnetic drift direction has been observed and its value was correlated to the amplitude of the magnetic perturbation (DED current).

The model applied, here, to describe this effects is displayed in figure 3.6 and is explained in more detail in the work of Ch. Busch and B. Unterberg [Busch 05, Unterberg 07]. The open ergodic system leads to an enhanced parallel electron loss along the field lines which is conceivable since the electron mass is much smaller ($\sim 1/1800$) than the ion mass. This enhanced transport leads to the changes in the radial electric field, and causes a ion return current as depicted in figure 3.6(a). The radial component of the perturbation field causes the field lines to come close enough to each other to allow a certain amount of cross field current j_i.

This current is sustained by a finite cross-field conductivity related to viscosity and friction with neutrals, it is necessary in order to keep the ambipolarity condition satisfied which can be written, as in case of the radial currents,

$$\begin{aligned} \nabla\vec{j} &= 0 && (3.4)\\ j_{||}sin(\alpha) + j_{\perp}cos(\alpha) &= 0. && (3.5)\end{aligned}$$

The angle alpha is introduced due to the fact that the disturbed field lines are tilted by the angle alpha with respect to their original direction by the magnetic perturbation field.

This angle alpha also causes a radial component of the current to be present and to flow outward, leading to a $j \times B$ force with a poloidal and a toroidal component (the parallel component can be neglected).

One can use the radial force balance of ions as well as the poloidal and toroidal momentum equations given in equations 2.32 and 2.25,2.26 as well as the calculations in [Kaganovich 98] regarding the transverse current (here given for the collisional limit) to create a model for comparisons [Unterberg 07] with the measured rotation and E_r data (Chapter 6). Assuming that the parallel loss current needs to be balanced by the perpendicular return current one reaches the following statement.

$$E_r = E_{r(diam.)} + E_{r(pol)} + E_{r(tor.)} \qquad \text{(rad. force balance)} \qquad (3.6)$$

$$\langle j_{||,r}\rangle = -\langle j_{\perp,r}\rangle = \sigma_{erg}(E_r - E_a) \qquad \text{(transv. current)} \qquad (3.7)$$

E_a is the so-called ambipolar field which can be written as

$$E_a = -\frac{T_e}{e} \cdot \frac{d\ln(n_e)}{dr} - \frac{1.71}{e}\frac{d\,T_e}{dr} \qquad (3.8)$$

and basically is valid in the case of zero current. σ_{erg} is the cross-field conductivity given by the parallel conductivity $\sigma_{||}$ as well as the Kolmogorov length $L_K$and the field line diffusion coefficient D_{Fl} as

$$\sigma_{erg} = \sigma_{||}\frac{D_{Fl}}{L_K} \qquad (3.9)$$

D_{Fl}, L_K can both be taken from mapping calculations [Abdullaev 99] and lead to a scaling of σ_{erg} as $I_{DED}^{8/3}$. Those quantities represent more or less scaling factors, to match this simple model with the observed effects.

3.3.2 Confinement Scenarios under the Influence of the DED

During the studies regarding the influences of the DED on the radial electric field and the plasma rotation discharges were performed that not only showed the changes in E_r towards more positive values and increase of rotation as expected from the above mentioned model, but also showed changes in the particle confinement.

As an example, discharges in Limiter H-Mode [Unterberg 09] and such with so-called Improved Particle Confinement (IPC) [Coenen 08, Schmitz 09, Finken 07a, Finken 07b] as well as particle Pump Out (PO) [Schmitz 09] are accessible.

The stochastic boundary at TEXTOR caused by the external magnetic perturbation from the DED is the origin of at least the IPC as well as the PO scenario. In both cases a direct connection between the changes in magnetic topology and confinement as well as plasma rotation and radial electric field can be seen as will be shown in Chapter 6.

Numerical simulations of the magnetic topology show that both scenarios are distinguished by the changes in field line connection length with respect to a specific resonance layer, namely the q=5/2 surface, and by the total extension of the stochastic boundary [Coenen 08, Schmitz 09], up to 6-8 cm into the plasma depending on the plasma current and position. The changes in the magnetic field are connected to changes in the global confinement, as will be described in chapter 6.

Chapter 4

Spectroscopy & Diagnostics

Emission spectroscopy is one of the most common methods to investigate plasmas. It allows the measurement of densities, temperatures and particle fluxes and more, via an unintrusive method. The utilized device is the plasma itself, its intrinsic or excited emissions. The interpretation of line emission requires an extensive knowledge of atomic and in some cases molecular physics, the specific cross-section and the underlying processes. For strongly fluctuating plasmas or high gradients, a local measurement is required, which can be supplied by using active atomic beams or laser [Schweer 08].

In this chapter an introduction is given in the spectroscopic methods used, namely active charge exchange with a diagnostic beam and passive Carbon III spectroscopy. The basic principles of measuring ion velocity, temperature and density shall be explained.

4.1 Active Charge Exchange Recombination Spectroscopy (CXRS)

The term Active Charge Exchange Recombination Spectroscopy (CXRS) describes the population and excitation of the atomic levels of impurity ions [Fonck 84] via introduced neutral particle beams. It allows both time and space resolved measurements of plasma parameters such as temperature, density and rotation.

The basic techniques are based on the evaluation of spectral profiles and Doppler-shifted emission lines from plasma impurities excited by charge exchange via the following reaction

$$A + B^{Z+} \rightarrow A^{+} + B^{(Z-1)+}(n,l) \tag{4.1}$$

n is the excitation state, l the angular momentum

A low Z impurity receives an electron from a fast or thermal neutral particle beam (H^0, D^0, Li^0 etc.). Those impurities do exist in almost every fusion plasma, hence this diagnostic method is widely used.

In this particular case we discuss the charge exchange reaction between neutral hydrogen and fully ionized carbon ions. The recombination process as described above leaves the resulting ion in an excited state. For Carbon the following reaction takes place:

$$\begin{aligned} H + C^{6+} &\rightarrow H^{+} + C^{5+}(n,l) \quad (4.2) \\ C^{5+}(n,l) &\rightarrow C^{5+}(n',l') + h\nu \quad (4.3) \end{aligned}$$

In order to choose the most suited emission line one needs to have an understanding of the excitation processes and the intensities of the different spectral lines. In this work only transitions with emission in the visible range are considered since they can be observed with reasonable effort.

It was shown [Fonck 84] that the charge exchange process is a resonant one, leading to the population of levels where the electron preserves its orbital energy and radius. This behavior leads to a peaking of the cross-section for $n_{max} \approx Z^{3/4}$

For higher excited states n, the distribution of the angular momentum number l is peaked around $l \sim n_{\mathrm{max}}$ [Fonck 84]. Thus transitions with $\Delta l = \pm 1$ between states near or below the maximum n are the most intense.

For the carbon spectroscopy considered in this work the visible spectral range is used and hence the transition $n \rightarrow n' = 8 \rightarrow 7$ at 529.0525 nm [Wiese 96] is the most suited.

4.1.1 Measured Quantities

In the following paragraph a short description of the accessible parameters shall be given, introducing the measurement of rotation velocity v_i as well as the measurement of ion temperature T_i and ion density n_i or intensity. In case of all quantities the measurements are commonly performed on impurity ions as described. For the background plasma additional assumptions have to be made. In Section 2.2.3 we have pointed out that eventhough the measured parameters are strictly applicable only for the used ion species, but can be interpreted via the radial electric field as a universal quantity. In the next paragraphs this aspect will be ignored and only sketched if being of interest for the particular quantity.

All quantities can be deduced from the spectral data shown in fig. 4.1(a).

Ion Velocity

The ion velocity is in principle is the most straightforward quantity to calculate, according to equation 4.4 based solely on the Doppler shift [Doppler 42, Einstein 05].

$$v_{ion} = c \cdot \frac{\lambda - \lambda_0}{\lambda_0} \quad (4.4)$$

Here c is denotes the speed of light, λ_0 the wavelength in the rest frame, λ the Doppler-shifted wavelength. In the presented case movements away from the observer are counted as having positiv velocities.

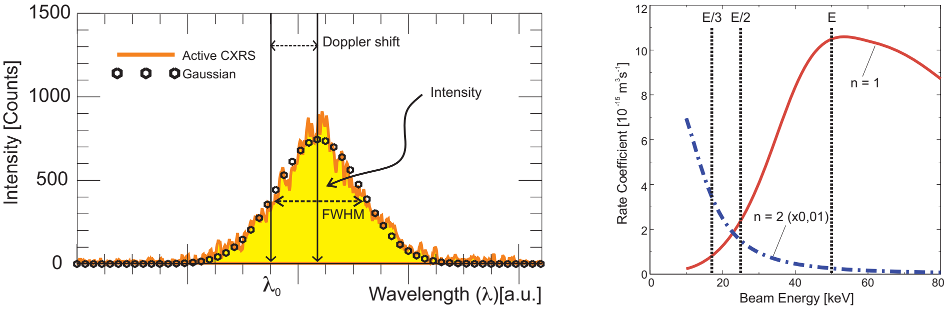

(a) (b)

Figure 4.1: (a) Active CXRS Spectrum from RuDI Diagnostic beam, acquired with the poloidal observation system. Shown are the discharge averaged active signal together with the fitted gaussian. Symbolized are the peak position as well as the intensity and FWHM. (b)Rate coefficient for the CVI (λ =529nm) transition stimulated via CX with a 50KeV hydrogen beam [Summers 94], Presented here are the curves for hydrogen in the $n = 1$ ground state (−) and $n = 2$ excited state ($- \cdot -$, scaled down by 100)

Ion Temperature

The ion temperature is connected to the spectral width of the observed emission line.It can be easily deduced. Based on the assumption of carbon being in thermal equilibrium [Bogen 95] the shape of the spectra can be assumed gaussian.

$$I_{\lambda_0} = I_0 \sqrt{\frac{m_i c^2}{2\pi k_B T_i}} \cdot \frac{1}{\lambda_0} \exp\left\{ \frac{-m_i c^2}{2k_B T_i} \cdot \frac{(\lambda - \lambda_0)^2}{\lambda_0^2} \right\} \tag{4.5}$$

I_{λ_0} denoting the Intensity of the chosen observed wavelength, I_0 the total observed Intensity for the chosen line, T_i, m_i the ion temperature and mass and k_B the Boltzmann constant.

With 4.5 the ion temperature is given in eV [1] as follows [Bogen 95, Isler 94]:

$$\begin{aligned} T_i[eV] &= \left(\frac{\Delta\lambda_{\text{FWHM}}}{\lambda_0}\right)^2 \cdot \frac{mc^2}{8e \cdot ln(2)} \\ &= \left(\frac{\Delta\lambda_{\text{FWHM}}}{\lambda_0}\right)^2 \cdot 1.68 \cdot 10^8 \cdot \mu[amu] \end{aligned} \tag{4.6}$$

The measured value is valid only for the species from which the spectra have been obtained. In how far the temperature agrees with the value of the background hydrogen or deuterium ions depends on the interaction between the two species. A typical measure for the agreement between both temperatures would be the so called equipartition time [Huber 00, Hey 94] which depends on the plasma density and temperature.

---

[1] $k_B \cdot T_i[K] = T_i[eV]$, $k_B = 8.617343 \cdot 10^{-5} eVK^{-1}$

With typical plasma parameters in the plasma edge of TEXTOR and a spatial resolution of the order of 1cm one can assume that the temperature measured is comparable to the temperature of the main ion species (deuterium, hydrogen) [Hey 94] since during one equipartition time the ions only travel 5 mm.

Ion Density

The impurity density measurement not only depends on the emission spectra but also on the knowledge of the photon flux produced in the plasma [Fonck 84] as well as on the beam attenuation.

$$I_\lambda = \frac{1}{4\pi} \sum_{j=1}^{M} \langle \sigma \nu \rangle_j^\lambda \int n_{Z_i} n_{b,j} d\ell \tag{4.7}$$

Equation 4.7 describes the intensity of a particular transition at wavelength λ along a line of sight that crosses the neutral beam (causing prompt CX recombination). Here n_{Z_i} is the impurity density and $n_{b,j}$ is the beam particle component at velocity $v_j = v_{full}/\sqrt{j}$. In case of a neutral hydrogen beam M=3 [Fonck 84]. The contribution of the beam halo neutrals is neglected.

Fig. 4.1(b) shows the rate coefficient for the charge exchange reaction with hydrogen at levels n=1 and n=2. Since both levels can have significantly different contributions to the intensity calculations, they both have to be taken into account (at low energies only 1% of the beam is in the level n=2 but the rate coefficient is 100 times larger).

Commonly an iterative code like CHEAP [von Hellermann 00] is used to solve this equation based on the measured photon flux and the known beam components. The calculation of the carbon density has to be performed in a self consistent way, since the beam attenuation and the carbon density are interdependent quantities in the course of solving this equation.

4.1.2 Fine structure & Zeeman Effect

The excitation due to charge exchange tends to prefer high angular momentum (l) states. Until those states decay, they have the possibilty to mix with lower l states due to ion ion collisions [Fonck 84, Schorn 92], which leads to a statistical population $(2l + 1)/n^2$. Due to the coupling between electron spin and ion angular momentum two distinct energy levels for each state (l) are generated (except for l=0) which both contribute to the spectra. Fine structure components can not be resolved with the means of the used spectrometers, but tend to broaden the spectra as well as give an assymetric contribution to its shape (cf. fig.4.2(b)) [Hey 94, Gangadhara 06].

Another Effect contributing to the spectra shape is the Zeeman effect. At magnetic fields well above $1T$ the Zeeman effect is in the order of the spin orbit coupling hence both couple separately to the magnetic field. Depending on the observation angle with respect to the magnetic field either the π and σ or both are visible.

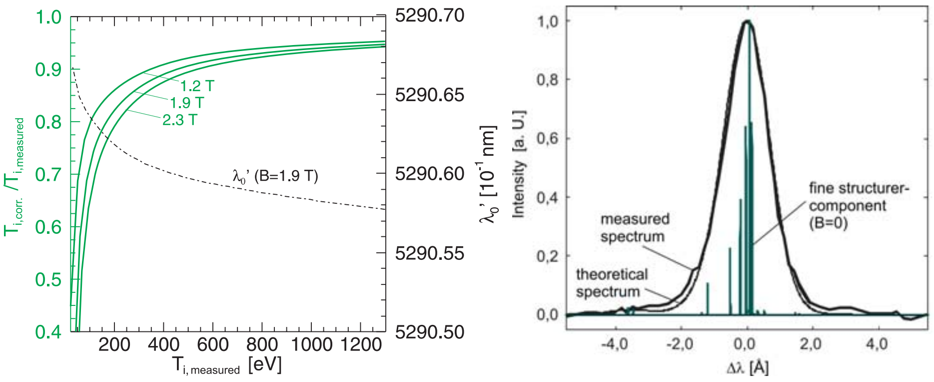

(a) (b)

Figure 4.2: (a) Corrections for the ion temperature at three values of the magnetic field, as well as corrections for the central wavelength of the spectra. Influence of Zeeman effect and fine structure splitting within a magnetic field. Displayed data is valid for the poloidal system at an average angle of 85°[Hey 93]. (b) The fine structure components for the CVI 8-7 transition at 529 nm (simplified with B=0) [Hey 94] overlap to a complex spectrum changing the profile to a non gaussian shape.

In the plasma edge, as observed by the diagnostic the Zeeman effect plays an important role, and thus needs to be corrected for [Hey 94].

Both, the Zeeman effect as well as the fine structure need to be calculated in order compensate for the effects on the actual wavelength and width of the spectra [Hey 93]. With knowledge of magnetic field, temperature, as well as observation geometry a correction is performed, correction factors are calculated and simply applied to the values obtained from the spectral data (cf. fig.4.2(a)).

4.2 Diagnostic Setup

In order to understand the improvements brought to the diagnostic setup, a few remarks are made, in advance, on the necessary diagnostic capabilities.

The resolution in poloidal and toroidal velocity is required to be < 1 km/s and < 10 km/s respectively, based on existing measurements at TEXTOR [Busch 06, Duval 07]. This requires a good spectral dispersion, here e.g. $10.8 \cdot 10^{-3}$Å$/pixel$ for the poloidal system. Taking into account the severe limitations due to photon statistics for the velocity resolution and the spectral shape (Section5.3) is one of the main tasks. The used hydrogen beam (cf. Section 4.2.1) delivers, in comparison to larger NBI, only a small current (2A), leading to a weaker emission of CX light, and hence making intensity one of the main diagnostic requirements (cf. Section 5.3).

In addition to the requirements for the rotation measurements the system should be capable of measuring the temperature over the whole temperature range accessible in the observed volume at TEXTOR $30\,eV < T_i < 1000\,eV$ [Schorn 92].

Common measurement tasks involve the study of DED induced magnetic topology and its influence on plasma rotation and temperature. In order to resolve this a high spatial resolution between 1 and 2 cm is necessary.

The time resolution for the measurement is typically 3 seconds considering the whole acquisition cycle necessary to reach a level of intensity required for high resolution velocity measurements. The frame rate with which the data is acquired is actually 10Hz which is required to allow the background substraction procedure (cf. Chapter 5) based on the beam modulation cycle of 5 Hz.

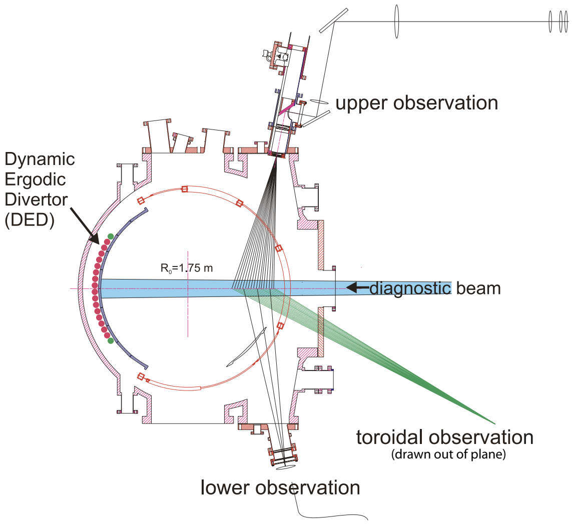

Figure 4.3: Overview of the vessel mounted components and the realized viewing lines of the CXRS diagnostic system. Observing $0.5 < r/a < 1.1$. The diagnostics are mounted to observe the Low Field Side (LFS). More details in figures 4.7 and 4.9

The diagnostic setup consists of three distinct systems, the Russian Diagnostic Injector (RuDI) and the two observation systems, including the subsequent spectrometers and camera DAQ systems.

As is depicted in figure 4.3 the diagnostic beam is located on the low field side of TEXTOR in the equatorial plane, while the observation systems are mounted nearly perpendicular to the direction of the beam in the poloidal and toroidal (equatorial) plane. In the following section each component shall be introduced, with a focus on the detailed description of the observation systems.

Both systems cover about half the minor radius of TEXTOR $(0.5 < r/a < 1.1)$ allowing coverage of the plasma edge (SOL) up to the plasma core. They are optimized to deliver as much intensity as possible to minimize the effects of photon statistics on the measured quantities [Coenen 09], as described in section 5.3.

The poloidal observation system was operated since 2002 [Kreter 01] and subsequently upgraded to its present form. The toroidal system was designed and included into the diagnostic in 2006. The optical designs were performed with the ZEMAX [Zemax-EE 06] software.

A similar systems exist at the TJII stellarator [Carmona 06] which also uses the differential Doppler shift method for CXRS, as applied already at JET and TEXTOR [Hawkes 92, Kreter 01, Busch 06].

The unique combination of the poloidal and toroidal systems at the TEXTOR Tokamak allows a consistent measurement of the rotation as well as of the radial electric field at one toroidal position.

4.2.1 The RuDI Diagnostic Beam

The Hydrogen Beam as depicted in figure 4.4 is based on the same principles as the common heating injectors [Uhlemann 93, deGrassie 03], but scaled down in terms of ion current and beam power, as well as beam diameter.

In case of RuDI an arc discharge plasma box [Deichuli 05] with a heated LaB_6 hollow cathode is used to produce a hydrogen plasma with a proton fraction of 78% as given in table 4.1. The plasma produced is accelerated by a set of grids with an accelerating voltage of up to 50kV. The beam subsequently neutralized in neutral hydrogen gas and fed through the beam duct into the tokamak vessel.

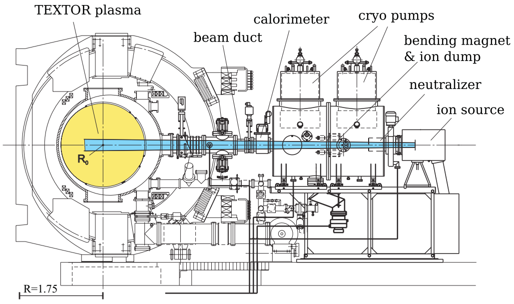

Figure 4.4: Setup of the Russian Diagnostic Hydrogen Beam (RuDI) at TEXTOR. Components such as the Arc-ion source, the Neutralizer and the bending magnet with their respective positions are shown.

Parameter	Value
Ion source	Arc Discharge
Beam energy	20-50 kV
Ion current	1-2.1 A
Species at 50kV	
H^+, H_2^+, H_3^+, H_2^0 [%]	74, 5,15, 5
Divergence	$0.55°$
Neutralisation efficiency	60-70 %
1/e width in TEXTOR	8 cm
Discharge duration	0.5-4 s
Modulation Frequency	5 Hz

Table 4.1: Parameters of the Russian Diagnostic Injector (RuDI) including beam composition, beam divergence and typical modulation frequency

The typical ion current of ~ 2 A leads to a neutral particle current of about 1.2 A, with a width (1/e) inside the vessel of 8 cm [Kreter 01, Busch 06]. The typical operation is performed at 50kV to maximize the rate coefficient of the charge exchange process between the CVI state and the full energy component hydrogen ground state [Fonck 84, Wiese 96]. The arc source is capable of producing 2A ion current with 5Hz modulation over a duration of 4s. The modulation presents an easy approach to background subtraction as described in Chapter 5, differentiating between active charge exchange from the beam and passive charge exchange from the background plasma.

Due to small width, divergence and especially input power the diagnostic beam can be used for spatially resolved CXRS measurements during all plasma scenarios with and without externally applied heating. Since the input power from the diagnostic beam is in the order of 55kW ”modulated” (compared to an ohmic heating of ∼ 300kW) on can be assume that the discharge remains unaffected by the interaction with the beam, and hence measurements can be performed during every heating scenario. The 50kV neutrals undergo charge exchange and then thermalize along the field lines, hence no local heating is achieved.

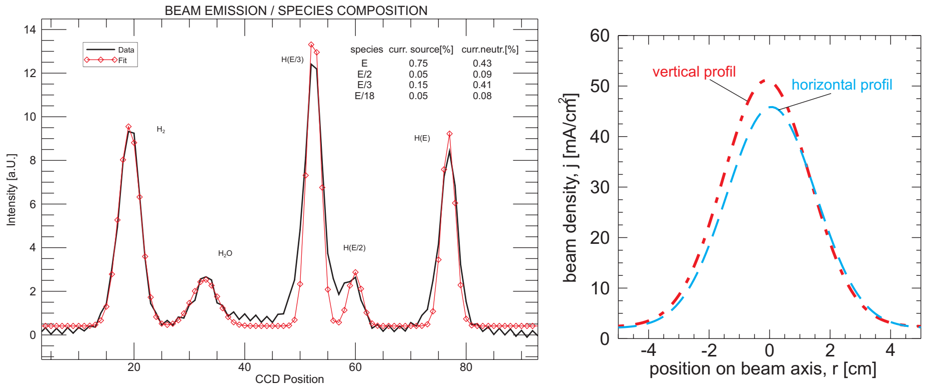

(a) (b)

Figure 4.5: (a) Spectroscopic measurement of the H_α emissions for the arc discharge plasma box, showing the different energy components and the beam composition. (b) Beam Profile measurement via the RuDI calorimeter (cf. fig.4.4)

Spectroscopy is used to determine the beam composition [Uhlemann 93, Geskus 03] based on the Doppler-shifted emissions from the several energy components. The shape and divergence of the beam can be measured via a calorimeter positioned 2 m after the plasma source. A typical species composition measurement is shown in figure 4.5(a), while figure 4.5 shows the gaussian shape of the beam.

4.2.2 Poloidal Observation System

The poloidal setup in this work was used in two distinct configurations. One used until December 2007 and the currently available setup. Both are displayed in figures 4.6 and 4.7.

The crucial point in measuring small poloidal rotation velocities is sufficient intensity reaching the CCD chip. Poisson statistic can have a significant influence on the measurement accuracy

[Coenen 09]. The work performed with the original setup lead to the conclusion that an upgrade was necessary in order to perform the measurements of the radial electric field. In the following section both configurations will be presented with the main focus on the current and improved setup. Since some measurements are based on the older system a short introduction will be given[Busch 06].

Original Setup (2002-December 2007)

The original setup, as displayed in figure 4.6 consists of two optics mounted on the tokamak TEXTOR. The main optics are mounted on top of the vessel, imaging the CVI emission onto 25 optical fibers, which are imaged in turn onto a high resolution spectrometer. The additional optics are mounted below the tokamak vessel, imaging the carbon emissions on 3 optical fibers used to function as reference channels ([Coenen 09, Carmona 06, Busch 06]). This system was mainly used for passive spectroscopy on intrinsic Carbon emissions (CIII) due to its lack of transmission and hence intensity for active profile measurements.

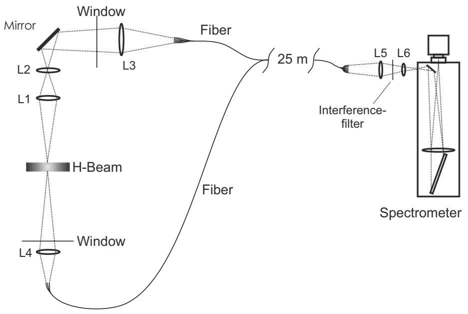

Figure 4.6: Poloidal observation with fiber connection (used until December 2007)

Lens	focal length [mm]	diam. [mm]
L1(2x)	250	50
L2(2x)	190	80
L3(3x)	190	80
L4(1x)	50	80
L5(2x)	31.5	120
L6(1x)	31.5	100

Table 4.2: Optical components of the poloidal observation systems

The system covered about 30 cm of the plasma minor radius leading to a complete coverage of the outer region of the plasma including the plasma edge and SOL at the low field side.

However this system due to its way of transmitting the light through optical fiber suffered from severe restriction due to photon statistic (5.3) and was consequently replaced by an upgraded system with a direct imaging optics for the upper main observation system. The upgrade includes a new camere system and improved transmission optics from spectrometer to CCD chip (cf. tab. 4.6).

Upgraded Setup (since December 2007)

The current poloidal observation system is also located in the poloidal plane of the tokamak vessel, as depicted in figure 4.3, it is equipped with a direct imaging from the vessel top and an additional bundle (3 channels) of optical fibers with a line of sight from the bottom of the tokamak vessel (opposing lines of sight) for the differential Doppler spectroscopy (cf. 4.3).

Table 4.3 in combination with figure 4.7 gives an overview of the properties of the poloidal observation system.

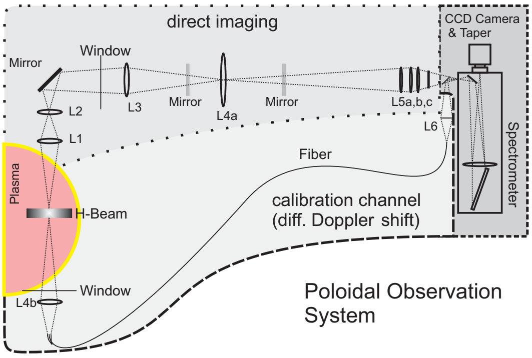

Figure 4.7: Geometrical overview, including optical components, of the poloidal observation system (Poloidal Cut). (colored in electronic version)

The direct imaging is optimized in two ways to satisfy the experimental needs and to overcome intensity limitations: Firstly the direct imaging components (figure 4.7) relay the 30 cm observation volume on to the entrance slit (h=25mm, w = 200µm) and subsequently through the spectrometer onto the 25 mm tapered image intensifier (≡ 10.5mm Chip) (cf. table 4.6) and secondly the numerical aperture (NA) is optimized to satisfy as much as possible the limitations due to the spectrometer acceptance angle (NA=0.05, table 4.5). The spectrometer as well as the camera system is explained in more detail in section 4.2.4.

(a)

lense	focal length [mm]	diameter [mm]
L1(2x)	250	50
L2(2x)	190	80
L3(1x)	100	350
L4a(1x)	145	150
L4b(1x)	50	80
L5(3x)	190	80
L6(1x)	80	12

(b)

Components	Distance
OBJ to L1	740 mm
L1 to L2	150 mm
L2 to L3	478 mm
L3 to L4	1110 mm
L4 to L5a	710 mm
L5a to L5b	20 mm
L5b to L5c	32 mm
L5c to Slit	45 mm

Table 4.3: Optical components of the poloidal observation systems and lens distances for both observation systems displayed in figures 4.7

The distance between the RuDI beam and the first optical element (L1) is 74 cm.

The in-vessel components (L1& L2) were optimized for an image NA of 0.4 [Busch 06] since they originate from the previous setup and are imaging the emission through the window on to the relay optics (L3-L5). This setup has a length of about 216 cm and is build to image the emission from the NA=0.4 at the window onto the spectrometer slit. By using a direct imaging system instead of fiber optics almost an order of magnitude in intensity was gained. In addition a broadband anti-reflection coating was applied for the range of 400 to 700 nm.

The bottom vessel observation for the differential Doppler spectroscopy is located 99 cm away from the beam, with one (L4b) lens imaging the emissions onto the optical fibers (NA=0.4) and another one (L6) imaging the fibers onto the spectrometer slit via a small mirror. Both parts are inclined by an angle of about 11° to the beam due to the available access points. This fact is later used to perform beam emission spectroscopy (BES) to determine the radial position of the viewing lines via the Doppler shift.

The radial channels can be chosen depending on the experimental scenario and the intensity requirements. Since a CCD Camera is used it is possible to either readout each CCD line, hence realize a very high spatial resolution with low intensity, or combine (binning) some channels in order to have reasonable spatial resolution with a good intensity.

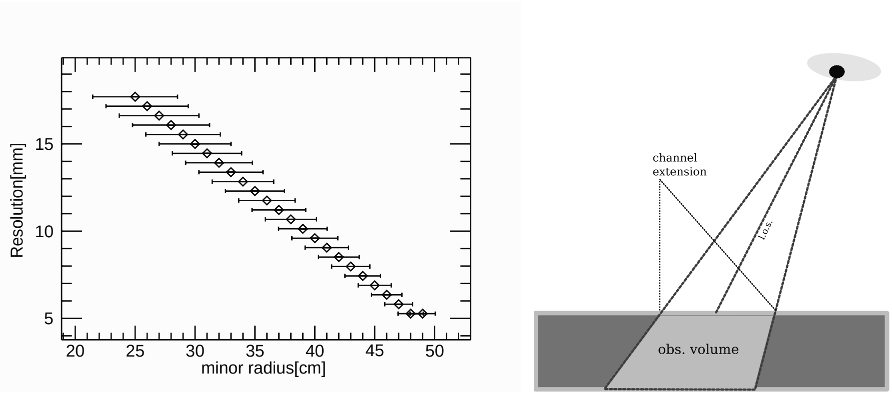

(a) (b)

Figure 4.8: (a) Spatial resolution for the poloidal system under the assumption of a channel spacing of 1cm.Bars also represent the resolution.(b) Observation volume, determined by beam width, and channel extension, as well as incident angle.

The spatial or radial resolution is determined by the size of the observed beam volume (fig. 4.8(b)), which in turn is determined in size by the CCD binning and the optical magnification. A channel observing 1cm of the beam will collect light from the complete volume, defined by the incident angle and the beam width.

The radial resolution is in the order of centimeter and is visualized in figure 4.8(a) for a case with each channel covering 1 cm. The poloidal system has a specially good resolution in the plasma edge due to the small incident angle with the beam at larger minor radius. This is of special interest for edge transport studies, as well as the measurement of the radial electric field in the plasma edge. The resolution plotted in figure 4.8(a) represents an evenly spaced case, but different radial resolutions for each part of the observation volume can be chosen. The overlap between several channels is only resolvable by sacrificing radial resolution, but should in the worst case only smoothen the profiles slightly.

4.2.3 Toroidal Observation System

The toroidal observation system is mounted in the equatorial plane of the tokamak observing the hydrogen diagnostic beam via a small mirror tangentially, as displayed in figs.4.3 and 4.9.

It consists of the collecting part (L1, L2) inside the tokamak vessel including the small mirror collecting the light from the direction of the beam, as well as a set of lenses to image on to the optical fibers (L3, table 4.4). The design was optimized to transfer the light to the fibers mounted on the image space side of the optics. The fibers have a numerical aperture of 0.4 and a diameter of 1 mm.

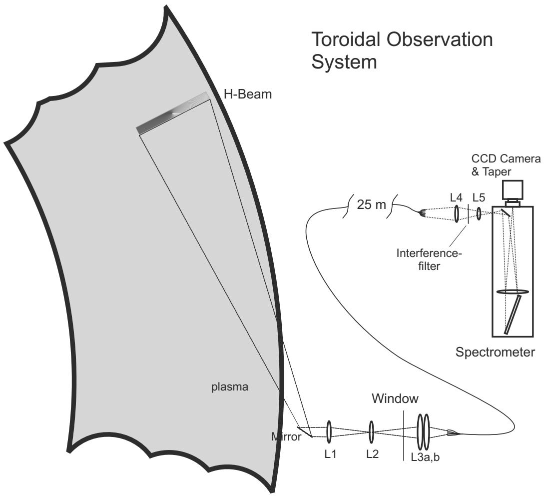

Figure 4.9: Setup of the toroidal observation system and its optical elements(Top View)

In contrast to the poloidal system the radial spacing is given by the size and the mounting of the optical fibers. The core of the fibers is 0.8 mm and leads to an object size of 12-15 mm.

(a)

lense	focal length [mm]	diameter [mm]
L1(1x)	120	31.5
L2(1x)	70	31.5
L3(2x)	100	50
L4(1x)	80	25
L5(1x)	50	25

(b)

Component	Distance
OBJ to L1	1132 mm
L1 to L2	128 mm
L2 to L3	152 mm
L3 to Fiber	68 mm
Fiber length	2500 mm
Fiber to L4	100 mm
L4 to L5	55 mm
L5 to Slit	45 mm

Table 4.4: Optical components and parameters of the toroidal observation system

The radial spacing and resolution is shown in figure 4.10 and is with 1-2 cm comparable to the poloidal system. The fibers are arranged in a block of 2 times 10 fibers, giving 2 fibers per radial channel (10 total), in order to improve the intensity available for each radial channel. In contrast to the poloidal system the resolution decreases to the plasma edge. Even though it would be preferred the other way around, constructional constraints leave this as the only viable viewing option for the toroidal observation system.

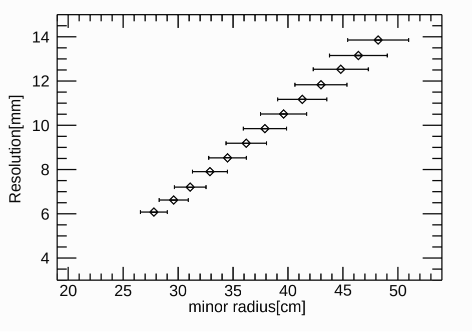

Figure 4.10: Spatial resolution for the toroidal system calculated for the actual fiber viewing lines. Bars represent the resolution.

In front of the spectrometer the fibers form a single line and are imaged on to the 250µm wide spectrometer slit using a small relay optic (cf. Section 4.2.4. In between the first 5 channels (10 fibers) and the last 5 channels (10 fibers) an additional fiber is supplied for the neon reference (λ=529.82 nm) produced by Geissler discharge neon lamp [Geissler 08, Pluecker 58]. All fibers are mounted in a straight brass housing, supplying accuracy and support to assure all fibers are aligned perfectly parallel to the reference channel [Coenen 09].

4.2.4 Spectrometers & Camera Systems

The light dispersion elements for the described diagnostics are two high resolution spectrometers as described in the overview table 4.5.

	Poloidal Yellow Spectrometer	Toroidal Blue Spectrometer
Spectrometer Type	Littrow	Littrow
Grating Type	Echelle	Echelle
Grating Size[mm]	220×110	160×130
Line Density $\left[\frac{\text{Lines}}{\text{mm}}\right]$	79.015	1200
Blaze	$76°$	$57.37°$
Order used	46	2
Focal Length [mm]	1000	750
Numerical Aperture	0.05	0.08

Table 4.5: Parameters for both spectrometers used in the poloidal and toroidal observation systems

The high resolution is required to resolve the particularly small poloidal velocities of order of 1 km/s. As mentioned before, the light collecting parts of the diagnostic are optimized for high transmission, since the spectrometers themselves have got very small numerical apertures (table 4.5) and etendue. The values are 0.021, 0.072 for the poloidal and toroidal system respectively. This trade off between resolution and photon statistics is the limiting factor for the capabilities of the diagnostic (section 5.3).

Both spectrometers are mounted in the Littrow configuration with an Echelle grating. Since intensity is of the essence to assure good photon statistics and hence a good spectral resolution, both gratings are used near the blaze angle. The poloidal spectrometer with a focal length of 1 m and a high dispersion grating is optimized for the use at λ=529 nm in the 46^{th} order, while the toroidal spectrometer is a common multi purpose spectrometer. Since in this high order several other lines may be visible in the observation region a bandpass filter with a width of 2 nm is used. The toroidal spectrometer is used in the 2^{nd} order; an additional filter is not required.

Even though the poloidal spectrometer in particular is optimized for use on the CVI line, both spectrometers can be used over most parts of the available spectral range (400-700nm) by adjusting the grating angle [Busch 06, Kreter 01].

	Poloidal (Upgrade) DAQ	Poloidal DAQ	Toroidial DAQ
Image Intensifier	BV2562 TZ-V	BV2562 TZ-V	BV 2582 QZ 100N
Structure	22μm	22μm	22μm
Taper	27:11.9	optical 1:1	27.5:12
Structure	6μm	-	μm
Camera	AVT Pike F100B	Dalstar 1M30	Dalsa CA D1
Chip	(1000x1000) px	(1024x1024) px	(256x256)px
Pixel Size	7.4 μm	12μm	16μm
Effective Size	16.8 μm	12μm	36.67μm
DAQ	PC SYSTEM	PC SYSTEM	VXI Controller
File Format	PNG/Raw	Binary	Binary

Table 4.6: Overview of Cameras, Chips, Fiber Tapers and Image Intensifiers used, including the older version of the poloidal setup.

The width of the slit is 200 μm and 250 μm, leading to an instrument function of 20 pixel and 12 pixel for the poloidal and toroidal system respectively after imaging on the subsequent cameras. In case of the toroidal system the instrumental function can be checked for each discharge with the available neon reference line.

The dispersion of the two spectrometers, measured with emission from an argon and neon reference lamp around λ=529 nm, are given in table 4.7. As an example figure 4.11 shows the argon lines used for the upgraded poloidal observation system.

Both specrometer systems are supplied with an image intensifier as stated in table 4.6, which are tapered on to the respective cameras to increase the transmission to the chip.

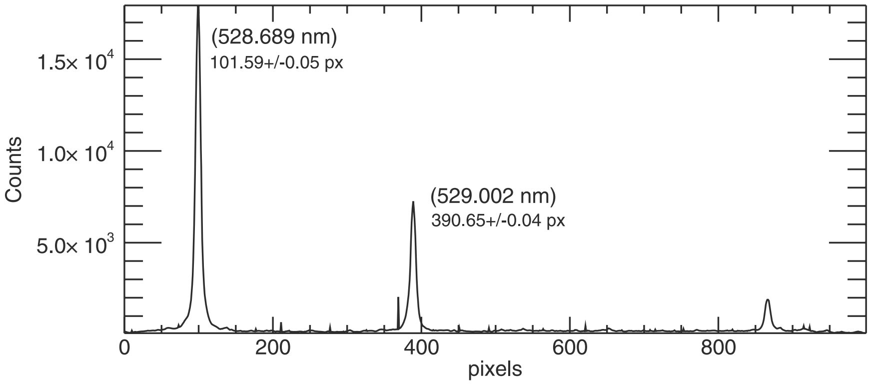

Figure 4.11: Argon lines used, to deduce the dispersion for the poloidal spectrometer

System	Wavelength[Å]	Discharges	Dispersion [Å/px]
Poloidal (AVT Pike)	CVI 5290.53		$(10.799 \pm 0.003)\ 10^{-3}$
Toroidal (Dalsa-VXI)	CVI 5290.53		(0.1624 ± 0.0005)

Table 4.7: Overview on the used dispersion values (Setup cf. section4.2)

Each system contains of a CCD camera system with symmetric chips allowing frame rates up to 30 fps with the full chip. The typical time resolution for the measurement is one beam period per discharge. This means a time window of three to four seconds per discharge. The frame rate is 10Hz to supply an integration time of up to 2 seconds for signal and background frames according to the 5 Hz beam modulation.

In chapter 5 the method is described to discriminate the background light from the actual active CXRS signal. Based on the beam modulation a scheme is developed for the acquisition of camera frames. During one beam period of about 3 to 4 seconds the beam is switched on and off every 100 ms and a frame is acquired every 100 ms with an exposure (shutter) times of 100 ms resulting in a set of frames with active and passive CXRS light as well as with only passive CXRS emissions. The cameras are triggered at a pace to match the modulation period of the diagnostic beam (5Hz) and hence are delivering 10 fps.

The toroidal system, due to the generally higher rotation velocities, is not as critical with respect to resolving rotation spectrally. It uses a $256\ pixel \times 256\ pixel$ chip where always two lines are combined in the direction of the chip correspoding to the radial direction in the plasma. This is done to increase the read out speed. A radial channel (fiber) typically is imaged onto $3(6)\ pixel \times 256\ pixel$, while the carbon spectrum itself is only covering a small part in spectral direction. This allows for the neon reference line (λ=529.82 nm) to be displayed continuously next to the plasma emission lines.

The whole chip covers $\sim$ 4 nm (table 4.7) which corresponds to temperatures between 20 eV and 3000 eV (Typical $\mathcal{O}$(100 eV)) measured from the Doppler broadening. The spectral resolution of the spectrometer allows a Doppler shift rotation measurement between 1 km/s (0.1 pixel) and the maximum measured of $\sim$ 100 km/s [Finken 05b].

The situation for the poloidal spectrometer is more specialized to the needs of the measured parameters. The setup is comparable with the toroidal system with one distinct difference, due to the high dispersion of (10.799 ± 0.003) 10^{-3} Å/px only a limited spectral window can be obtained across the (1000x1000) pixel^2 chip. The spectrometer has a resolving power of $R_{theo} = 4.1 \cdot 10^5$. The spectral window of $1.1nm$ allows temperature measurements of up to 900 eV with a resolution well in the range of eV, taking into account only the dispersion of the spectrometer. The resolution in terms of Doppler shift measurements of the ion velocity is in the order of 0.3 pixel based on the computer aided analysis, meaning 200 m/s when considering the dispersion.

The radial binning, meaning the combination of several CCD lines, is performed off line. Since the emissions are directly imaged onto the spectrometer and hence the camera chip one has complete freedom whether to analyze the whole frame line by line with a small intensity, or to choose a binning which offers more intensity. The AVT Pike F100B is able to obtain full frame images with a frame rate well above the beam modulation rate.

The resolutions can be severely limited by the photon (Poisson) statistics which has to be taken into account for later measurements and accuracy discussions, as given in section 5.3.

4.2.5 Theoretical Resolution of the Measurements

In this paragraph only the resolution available due to the dispersion as mentioned before, now taking into account the actual CCD pixel size and the computer based methods to determine the spectral shape. The actual resolution is determined by the actual spectra described in the following chapter (chapt. 5).

Poloidal Observation System

If one takes into account the Dispersion ab. 4.7) of $(10.799 \pm 0.003)10^{-3}$Å and equation 4.4 one can calculate the actual resolution available in terms of velocity. In order to assess the velocity and temperature resolution one needs to assume a certain accuracy determined by the mathematical procedure used to fit the data to the gaussian hypothesis. One can assume that the procedure is typically able to determine the peak position well under one pixel. For the purpose of this discussion we assume $0.3pixel$, based on the experience with the used routines.

$$\left|\Delta v_\theta^{theo}\right| = c \cdot \frac{\text{Disp[nm/px]} \cdot 0.3 \text{ pixel}}{529\text{nm}} \approx 180m/s \qquad (4.8)$$

For the assesment of the theoretical temperature resolution we perform a similar calculation based on equation 4.6

$$\left|\Delta T_i^{theo}\right| = 1.68 \cdot 10^8 \cdot 12 \cdot \text{Disp[nm/pixel]} \cdot \left(\frac{0.3 \text{ px}}{529\text{nm}}\right)^2 \approx 1eV \qquad (4.9)$$

As can be seen here the dispersion together with the evaluation methods gives still sufficient margin for high resolution measurements.

Toroidal Observation System

The same applies for the toroidal observation system. The dispersion is given as 0.1624 ± 0.0005Å.

$$\left|\Delta v_\theta^{theo}\right| = c\cdot\frac{\text{Disp[nm/px]}\cdot 0.3\text{ pixel}}{529\text{nm}} \approx 2800\text{ m/s} \tag{4.10}$$

$$\left|\Delta T_i^{theo}\right| = 1.68\cdot 10^8\cdot 12\cdot\text{Disp[nm/px]}\cdot\left(\frac{0.3\text{ pixel}}{529\text{nm}}\right)^2 \approx 10eV \tag{4.11}$$

4.3 Calibration Methods

The two observation systems utilize two distinct ways to determine the rest frame wavelength λ_0, which is necessary for the rotation (cf. equation 4.4) as well as for the temperature (cf. equation 4.6) measurements. The poloidal system uses the so called differential Doppler spectroscopy [Hawkes 92, Busch 06], while the toroidal system simply relies on a neon reference line, which is imaged on one of the channels imaged onto the CCD chip.

Differential Doppler spectroscopy utilizes two opposing lines of sight to acquire one red shifted and one blue shifted spectrum from the same rotation. In case of the poloidal observation system, this is one channel mounted on top of the tokamak and one optical fiber channel originating from below the vessel as displayed in figure 4.7.

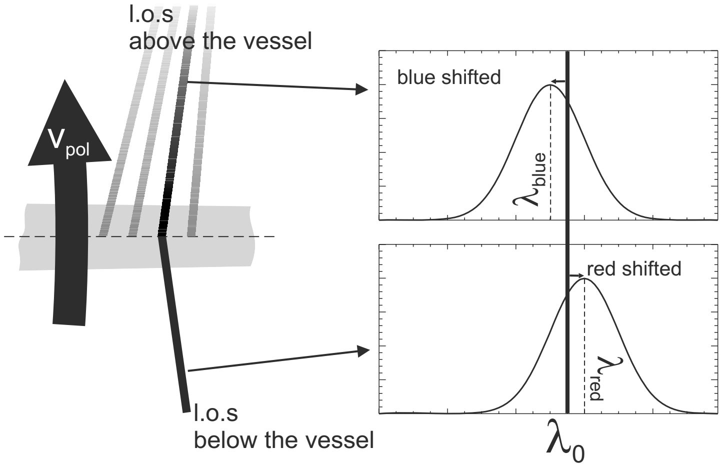

Figure 4.12: Sketch of the differential Doppler spectroscopy principle. Two opposing lines of sight compensate for any inherent calibration error and deliver a very precise measurement of the reference wavelength [Busch 06].

Via this setup one obtains two spectra, with distinctly the same shift in opposite directions. Both shifts represent the rotation velocity (v_{pol}) with respect to the rest frame wavelength λ_0 as shown in figure 4.12.

Both spectra are fitted with a gaussian distribution and the positions of λ_{red} and λ_{blue} are then used to calculate the position of λ_0 on the CCD chip. This is achieved by taking the mean value of the peak position corresponding to the wavelength on the CCD.

$$Pos(\lambda_0) = 0.5 * (Pos(\lambda_{\mathrm{red}}) + Pos(\lambda_{\mathrm{blue}})) \tag{4.12}$$

With sufficient photon statistics this method is accurate to the order of the velocity resolution of the spectrometer (<1 km/s) and hence the best method to assure a valid measurement of small poloidal rotations. This system is used in a similar form since 2000 [Kreter 01] and a similar system is used at the TJII stellarator [Carmona 06]. In contrast to the common use of reference lines this method presents a direct measurement of the rest frame wavelength and is hence less prone to systematic errors, which are here compensated by the differential approach.

The toroidal observation system uses a neon reference line imaged onto the CCD which is continuously emitted through the whole discharge. The line (529.82 nm) is fitted together with the CXRS spectra and its position is used to determine the position of the rest frame wavelength. Since all fibers, including the reference channel, are mounted collectively in front of the spectrometer, the discrepancy between incident angles is negligible.

The absolute intensity calibration is needed for the density calculations, it is performed using an Integrating sphere in front of the observation system at the position of the neutral heating beam. This allows to measure the ratio between emitted photon flux and the counts on the cameras CCD. This is then could later be used as input for the iterative CHEAP code [von Hellermann 00, von Hellermann 08] which solves equation 4.7.

4.3.1 Radial Calibration

The radial calibration can be performed in two ways. The first option is to illuminate the optical fibers or the spectrometer slit, so that an image is produced on a measuring tool at the position of the hydrogen beam inside of the vessel. Hence a direct connection can be established between the fiber or slit position and the radial position along the beam. This method is very accurate and used during openings of the tokamak vessel.

Since a vessel opening is only performed once every year a second reliable option is needed. This option is based on the Dopplershift spectroscopy principle using so called Beam Emission Spectroscopy(BES). A typical frame from one of the BES discharges is shown in figure 4.13. Each energy component of the neutral beam has got a different velocity, and each line of sight has got a distinct angle with respect to the beam direction. Hence one can use this knowledge to deduce the position of the viewing line with respect to the known position of the zero degree viewing line.

$$r_{\mathrm{l.o.s}} = R_{\mathrm{l.o.s}} - R_0 \;\; = \tfrac{1}{3} \;\sum_i \frac{r_{\mathrm{plumb.}} - h_{\mathrm{plumb.}}}{tan(\beta_{l.o.s,\, i})} \tag{4.13}$$

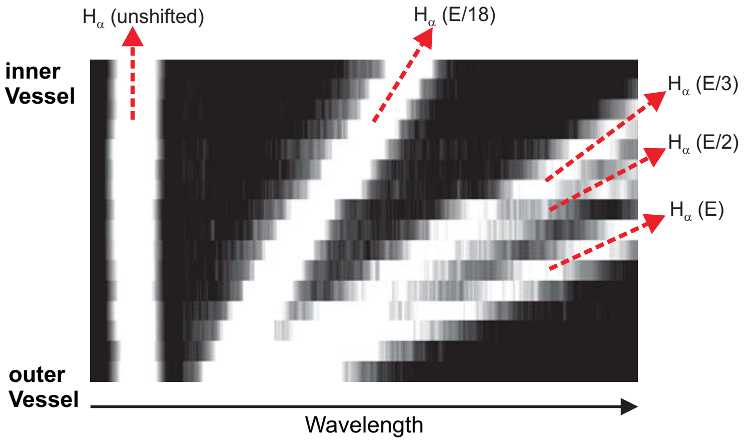

Figure 4.13: H$_\alpha$ emissions for the radial calibration of the poloidal observation system. Due to the inclination angle of the viewing lines each channel has a distinct Doppler shift for the different parts of the beam energy spectrum (1(H$^+$), 1/2(H$_2^+$), 1/3(H_3^+), 1/18(water) [Busch 06].

$$\beta_{l.o.s,\ i} = arccos(\Delta\lambda \cdot 0.15 \cdot \sqrt{i}) \quad (4.14)$$

$$i \equiv E/i\ ,\ i\epsilon\{1,2,3\} \quad (4.15)$$

β describes the angle between the line of sight and the diagnostic beam deduced from each Doppler-shifted energy component spectrum. The factor 0.15 accounts for the H_α wavelength as well as the beam velocity with respect to c. The value $\Delta\lambda$ is the wavelength shift for each energy componens with respect to the H_α emission. The beam emission takes place during a beam discharge into the H_2 gas vented tokamak vessel, at 10^{-3} mbar.

4.3.2 Finite Slit Height

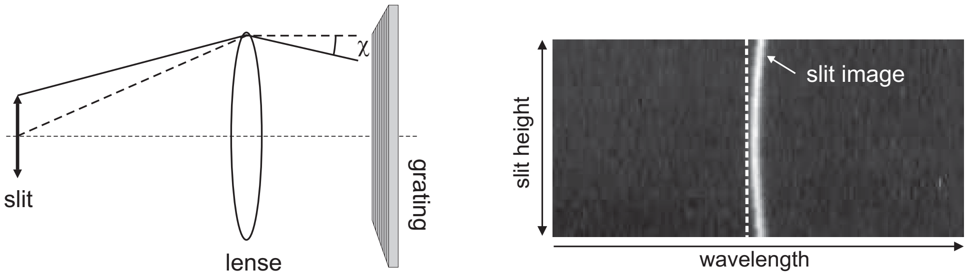

(a) (b)

Figure 4.14: (a) Sketch of the effects of finite slit and grating height, causing a distortion of the image of straight slit.(b) shows a typical frame obtained with the observation system imaging a neon pen-like lamp onto the entrance slit of the poloidal spectrometer.

In order to determine the correct spectral position for each channel of the observation system one has to take into consideration the finite height of slit and grating as displayed in fig. 4.14(a). Since the slit as well as the grating have finite height, different points of the entrance slit are imaged under distinct angles χ onto the grating [Last 03]. For light coming to the grating under the angle χ the grating has a smaller line density, since the lines are closer by $cos(\chi)$. This effect leads to a stronger bending of the outermost parts of the slit. according to equation 4.16.

$$\lambda' = \frac{\lambda_0}{cos(\chi)} > \lambda_0 \tag{4.16}$$

The image on the camera chip (fig.4.14(b)) has to be corrected accordingly. In case of the used spectrometers a Neon or Argon line around λ =529 nm was imaged onto the entrance slit. The acquired images have been evaluated and a 2nd order polynomial was fitted to the data.

When data from the database is read, the correction is automatically applied according to a configuration file on a shot by shot basis.

Chapter 5

Data Evaluation

This chapter will continue the explanations given in section 4.1.1 of the measured quantities. The methods to acquire the information regarding temperature, density and rotation are explained and the accuracy of the resulting data is being discussed.

5.1 CXRS Measurements with the RuDi Hydrogen Beam

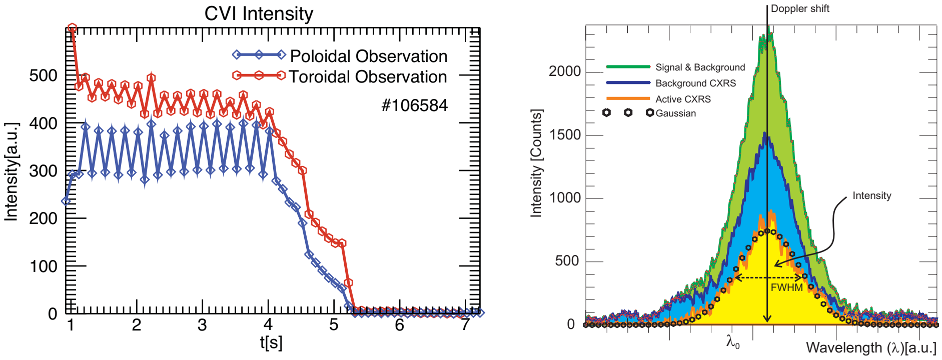

(a) (b)

Figure 5.1: Intensity evolution of the C VI Line, measured during one discharge. showing the modulation of the intensity with the neutral beam modulation. Charge Exchange Spectra from the poloidal observation system, displaying the measurement of the spectral shape.

The measurements are performed via charge exchange as explained in section 4.1. In case of the setup used at TEXTOR the hydrogen beam is modulated with 5Hz and the frames are acquired accordingly. This means that the cameras are triggered with a frequency of 10 Hz, acquiring one frame with and one frame without active charge exchange signal from the hydrogen beam.

The time resolution of the acquisition system is accordingly 100ms while the time necessary to acquire signal with sufficient S/N ratio is in the range of seconds.

This becomes more clear when taking figure 5.1 into consideration. Both (a) and (b) show the principle used. On the left hand side a time trace of the acquired camera data is shown, depicting the overall intensity and the modulation in its amplitude.

Shown are modulated signals for the poloidal and toroidal system with a modulation depth (ratio of active to passive signal) of $\Delta(I_{pol})/I_{pol} = 0.199 \pm 0.060$ and $\Delta(I_{tor})/I_{tor} = 0.054 \pm 0.027$ respectively, which is the typical value for a TEXTOR discharge with densities around $n_e \cong (2-3) \cdot 10^{19} m^{-3}$.

The modulation depth describes the ability to discriminated the active from the passive component of the CXRS spectra as shown in figure 5.1(b).

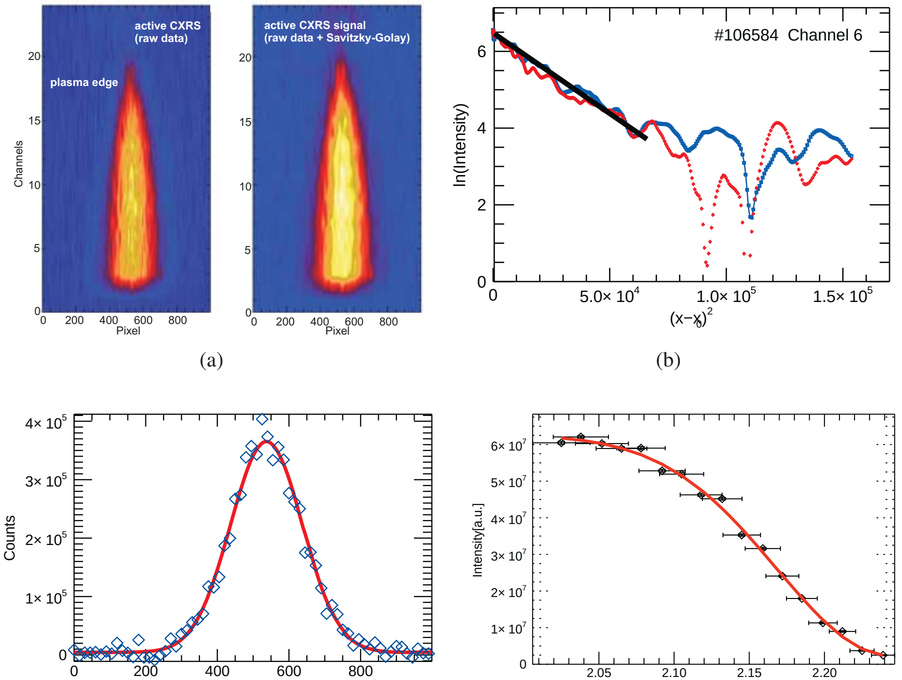

(a) (b)

(c) (d)

Figure 5.2: Typical analysis steps shown based on the poloidal data for discharge # 106584 in the typical order. (a) shows the active signal along the spectral and radial axis, before and after smoothing. (b) shows the linearized spectra (assuming gaussian distribution) performed on channel 6 (R=2.03m) of the presented data giving a linear decay of Δln(I)= 2.8 or a gaussian behavior over more than one order of magnitude.(c) shows the data and the resulting fit for channel 6 (R=2.03m), (d) shows the calculated intensity over the whole radial profile.

Regarding the signal intensity a few facts need to be taken into account. Typically a modulation depth above 10% [Kreter 01, Busch 06] is preferred to acquire reliable data, but on the other hand a small modulation depth can be compensated by a large overall intensity. The shape of the spectra and hence the ability to perform the data analysis directly correlates with the intensity available (cf. section 5.3).

Regarding the signal to background ratio a few factors come into play. The C^{6+} density rises towards the plasma center as can be seen in figure 5.2(a) and 5.2(d) while, on the other hand, the hydrogen beam intensity drops towards the center due to the interaction with the plasma ions. This means the active signal depends on these two factors while the recycling flux, which is the source of the passive background CX, is scaling with the plasma density. The higher the density the higher the background signal the worse the modulation depth. In addition to this effect discharges with neutral beam introduce additional difficulties since the background signal increases even more towards the plasma center [Kreter 01]

To acquire the spectra shown in figure 5.1(b) or figure 5.2(c) the data is evaluated as follows. First one determines the length of the flat top phase of the discharge for evaluation and afterwards sums up all the available active and passive frames, respectively. Then the difference between the two spectra delivers the actual active CX emission spectrum.

One ends up with a set of spectra, one for each radial channel, which represents the mean spectra for the whole shot or time period selected. From experience at least 2s of flat top phase are necessary to acquire a reasonable signal quality (10 active and 10 passive frames with 100 ms duration each).

After those spectra are acquired, additional analysis steps are performed ending with the final fitting procedure and the calculation of the ion temperature and rotation.

Figure 5.2 shows the steps based on the poloidal data of shot 106584. The data was binned into 25 channels into the radial direction and retains its original 1000 pixel in the spectral direction. Figure 5.2(a) shows the raw data for all radial channels after the initial averaging process.

It is obvious that the temperature, meaning the width of the spectrum is increasing towards the plasma center, as well as the intensity of the signal which is correlated to the impurity density (cf. equations 4.6-4.7).

In order to improve the spectral shape but at the same time retain the spectral features like width and peak position a Savitzky-Golay smoothing is applied [Savitzky 64, Press 92] which results in the smoother representation shown on the right hand side of 5.2(a).

In order to determine if the spectrum actually fulfills the assumptions of a gaussian shaped emission spectrum a test is performed. According to equation 4.5 the logarithm of the intensity displayed against the quadratic distance from the peak maximum should follow a linear trend if the emission spectrum is of gaussian shape. Figure 5.2(b) shows this behavior for one of the radial channels of the previously presented data. Typically the window of gaussian behavior is used as an input parameter for the subsequent fitting in order to guarantee the best fitting results by using only the truly gaussian part.

After the data has been averaged and the individual fitting windows have been determined the fit is performed [Markwardt 03] assuming a gaussian shape and a base line of zero according to the background subtraction scheme. Figure 5.2(c) shows the resulting curve together with the used data from channel 6. The agreement between the gaussian assumption and the fit is reasonably good and accounts for the later discussed (cf. section 5.3) high velocity resolution of the poloidal system.

At the end of the data evaluation the quantities Intensity as well as temperature and rotation are calculated. Figure 5.2(d) displays as an example the calculated intensity profile given from the amplitude and width of the evaluated spectra according to

$$I = \sqrt{2\pi} \cdot \mathrm{A} \cdot \frac{\mathrm{FWHM}}{2\sqrt{ln4}} \tag{5.1}$$

where A is the peak amplitude and FWHM represents the Full Width Half Maximum.

Remarks on the Carbon Density Measurements:

From the above mentioned intensity the carbon density can in principle be deduced by using the so-called CHEAP Code (Charge Exchange Analysis Package) [von Hellermann 08, von Hellermann 00]. The code, if supplied with the correct RuDI parameters and geometry, is able to calculated self consistently the local beam attenuation in an iterative process, always taking into account the carbon density as well. With the input of plasma density, ion temperature and plasma rotation as well as the beam composition, the carbon density can be deduced. The calculation is based on the conversion of intensity into photon flux density, hence needs an in vessel calibration using a calibrated light source. Since in the course of this work only the pressure is of interest, an absolute calibration has not been performed; only a relative point to point calibration was necessary.

Remarks on Impurity Rotation Measurements:

As given in equation 4.4 the rotation is calculated from the shift in wavelength, or spectral peak position. The peak position for each radial channel is calculated and corrected with respect to the effect caused by the finite slit height. The positions are then used with respect to the calculated reference position (based on one upper and one lower viewing line) to deduce the actual impurity rotation after correcting the wavelength difference with respect to Zeeman and fine structure influences (section 4.1.2).

Remarks on the Ion Temperature Measurements:

The ion temperature is calculated from the width of the spectrum given by the gaussian fit performed during the data evaluation. The width represents the temperature without account of the Zeeman and fine structure broadening as given in section 4.1.2. The temperature is derived with the corresponding correction factors. Profiles of the ion temperature are shown in the following section and rotation profiles are presented in chapter 6. The discussion of the accuracy of the calculations and the respective uncertainty remarks are given in section 5.3.

5.2 CIII Measurements

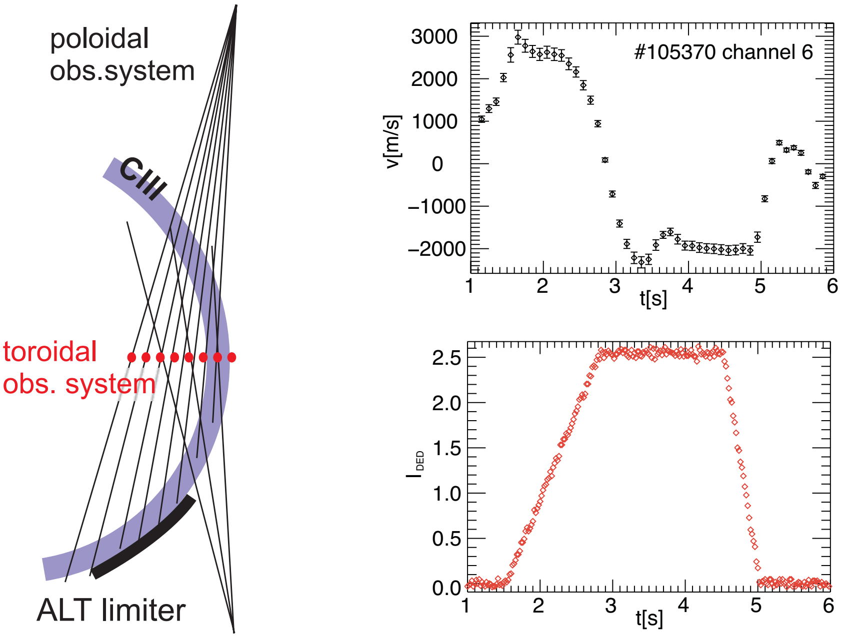

(a) (b)

Figure 5.3: (a)Shows the setup of the viewing lines used during CIII emission measurements. the dots symbolize the equatorial viewing lines of the toroidal system. (b) Presents data for a plasma discharge observed via CIII emission to observe the time dependences.

In the case of the active CXRS measurement the time resolution is limited by photon statistics to an integration time of 1.5s (3 s modulated). In cases where a higher time resolution for the rotation is needed, both the poloidal and the toroidal observation systems can measure the passive CIII emission from the plasma.

The C III emission at 464.7 nm is localized at the plasma edge since it represents a low ionization stage of carbon, in contrast to the CVI emission which can be observed over the whole plasma radius [Claassen 90].

Where the active measurements allow, due to the intersection of viewing lines and beam, a profile measurement from the whole plasma the CIII measurements are restricted to one local measurement with high intensity just inside the last closed flux surface.

Thanks to high intensity at this position the time resolution can be increased up to 30 ms (limited by the DAQ).

An example for this is shown in figure 5.3, displaying the rotation measurement during DED operation. The CIII rotation follows the DED amplitude, it changes towards the ion diamagnetic drift direction (cf. section 3.3).

For both systems the signals are line integrated since the viewing lines run tangentially through the emission layer. One the one hand this means that the localization of the signals is especially difficult, on the other hand it means that especially for the poloidal system the deduction of the wavelength reference position is more complicated.

While in case of the toroidal system a neon lamp can be used to blend in a reference line and hence deduce the Doppler shift, the poloidal systems differential Doppler shift approach needs to be revisited. For the active method a clear assignment between upper and lower channel was possible based on the radial calibration. For the passive method the lower channel is now matched with a channel showing the same spectral width, hence the same temperature and location as the upper partner.

With respect to the data analysis, the difference between the active and passive measurements is that, for the latter, the averaging is not performed. All subsequent steps are identical except that the procedure is performed for only one radial channel, but for a large number of frames.

5.3 Accuracy

In the following section the accuracies and the constraints as well as the applied uncertainty calculations for the toroidal and poloidal impurity velocity, and for the the ion temperature are presented.

The measurement uncertainties in rotation and temperature are calculated on the basis of the uncertainty of the dispersion and the calculated uncertainty on width and position of the gaussian fit. For the temperature an additional term is used to account for the poisson statistic.

Some of the numbers regarding the resolution have been discussed earlier (Section 4.2.4 & Section 4.2.5); with the dispersion, as given in table 4.7 the poloidal system is capable of resolving 1km/s rotation as a spectral shift of 1.6 pixel on the CCD Chip while 100eV in ion temperature are equivalent to a FWHM of 118 pixel. For the toroidal system 1km/s is around 0.1 pixel and 100 eV are in the range of 7 pixel.

Two points are evident: first the poloidal system is quite well equipped for rotation and ion temperature measurements but, due to limitations in the intensity, is prone to errors due to Poisson statistics, especially regarding the position measurements. The smaller the intensity the more distorted the spectral shape can be. Secondly this does not have a large effect on the temperature measurements, since the width is well determined.

For the toroidal system the situation is much less complicated, firstly because of the toroidal system has much more light available and a smaller dispersion and secondly due to the different measurement scale ($>$ 10km/s). The temperature measurement on the other hand is more difficult with the given dispersion.

In Figure 5.4 a temperature measurement is shown, comparison between the poloidal and toroidal data. The agreement between both measurements is quite well. Considering the radial and the temperature uncertainties the two curves match. The radial uncertainty originates

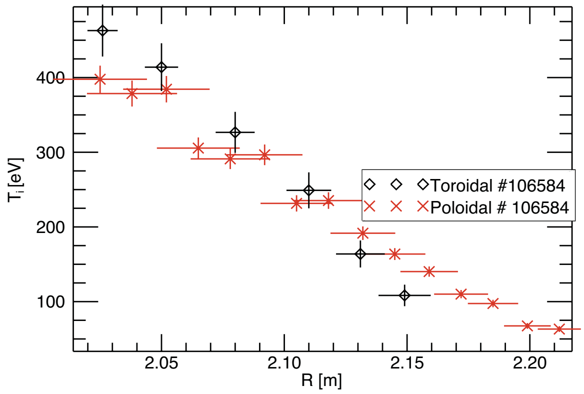

Figure 5.4: (Temperature measured by poloidal and toroidal observation during discharges #106584, January 2008)

from the calculations presented in figures 4.8(a) and 4.10. This plot on the other hand shows the different capabilities of the two systems, while the poloidal temperature uncertainty is miniscule compared to the symbols displayed, the toroidal temperature uncertainty is much larger. Typically the poloidal system is preferred for temperature measurements, since the resolution is much better (1 eV $\widehat{=}$ 1 pixel).

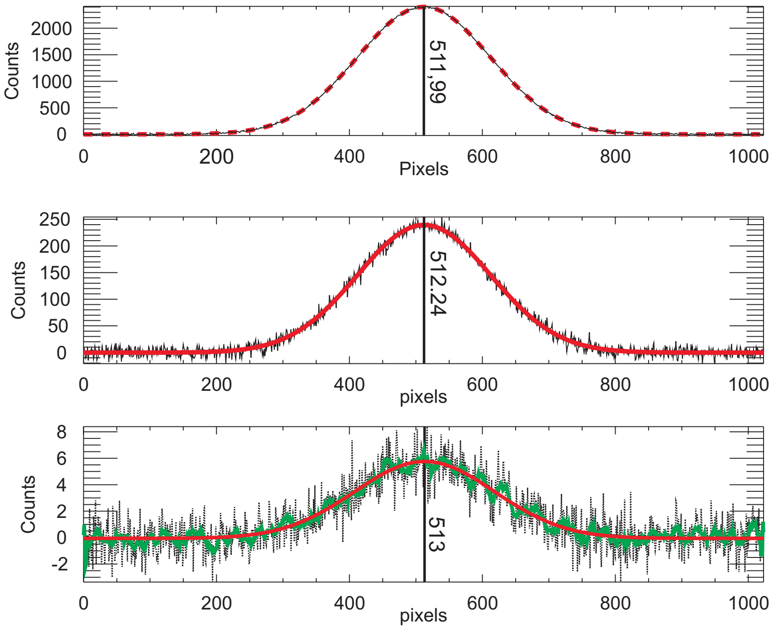

Figure 5.5: Simulated spectra on a 1024 pixel chip, with a FWHM comparable to typical temperatures at TEXTOR. Gaussian shape spectra with different ”intensities” and overlayed poisson noise. The central value is 512, the values fitted afterwards are presented as well.

The effect of Poisson statistics has been discussed to some extent; to show the effects qualitatively and quantitatively figures 5.5 and 5.6 are used.

Fig.5.5 shows the simulated behavior, assuming a gaussian signal distorted by poisson noise. The smaller the intensities, the more dominant the changes on the spectrum and the subsequent position calculation.

Since the simulations were used to understand the behavior of the diagnostic before the present status was established, measurements with a tungsten lamp were performed additionally. The result is presented in figure 5.6(a). An intensity of 1 is equivalent to the worst case and evidently shows that intensity gain is required to reach a reasonable velocity resolution.

This stresses that intensity and dispersion are intertwined and that both need to be optimized in order to obtain reasonable results.

The data typically taken is presented using the following uncertainty calculations:

$$\sigma_v = c \cdot \sqrt{\Delta_{\mathrm{p}}^2 \cdot \sigma_{\mathrm{D}}^2 + \mathrm{D}^2 \cdot (\sigma_{\mathrm{rp}}^2 + \sigma_{\mathrm{p}}^2)}/\lambda_0 \tag{5.2}$$

$$\sigma_T = T_i \cdot (2\sqrt{(\sigma_{\mathrm{D}}/\mathrm{D})^2 + \cdot (\sigma_{\mathrm{s}}/\sigma_{\mathrm{spec}})^2} + \frac{1\,pixel}{\mathrm{fwhm}}) \tag{5.3}$$

For the velocity, equation 5.2 describes the calculation of the uncertainty taking into account the doppler shift in terms of chip position ($\Delta_p[pixel]$), the the Dispersion (D[Å/pixel]) and its uncertainty ($\sigma_D[\text{Å}/pixel]$) as well as the uncertainty on the peak position ($\sigma_{\mathrm{p}}[pixel]$) and the reference position ($\sigma_{\mathrm{rp}}[pixel]$) (both pixel positions on the chip). The gaussian fit uses as input parameters the obtained spectral data and statistical information from the data set. The statistical weight is given as $1/\sqrt{N_{\mathrm{active}} + N_{\mathrm{passive}}}$, where N denotes the number of counts per pixel in the frames with and without active beam respectively. For the temperature a similar uncertainty calculation (eq.5.3) has been performed, and a systematic error (1 pixel / fwhm[pixel]) has been included accounting for the unfortunate fact that a small deviation due to poisson noise can have a significant influence on the toroidal measurements of T_i. The dispersion as well as its uncertainty are included into the calculation as well as the spectral width ($\sigma_{\mathrm{spec}}[pixel]$) and its uncertainty ($\sigma_s[pixel]$)

From this calculation one can deduce the typical error bars, which amount for the poloidal rotation typically to σ= 0.7 km/s and for the toroidal rotation σ=4 km/s.

For the temperature it is clear from equation 5.3 that the error scales with the temperature itself, and is larger further inside the plasma. To this a systematic uncertainty is added, accounting for the narrow spectral width being subject to more influence from photon statistics. A photon ending up in one or another pixel can have influence on the shape and hence on the width and peak position.

The typical error for the poloidally measured ion temperature is in the range between 2 eV and 10 eV, while the toroidally measured temperature has a larger uncertainty of 5 eV to 40 eV.

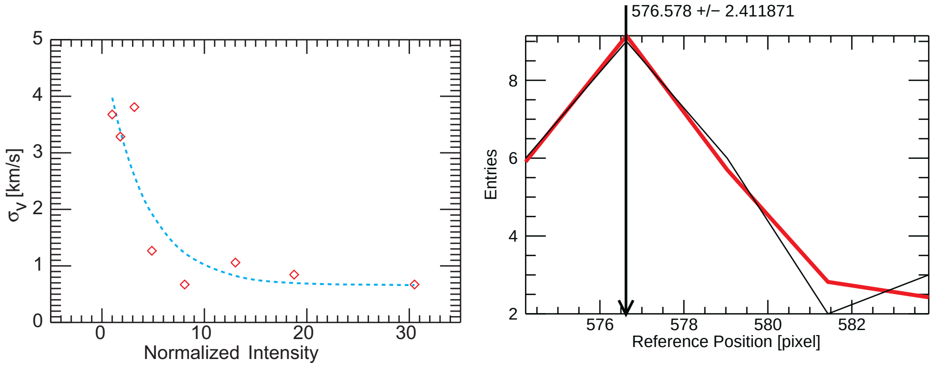

(a) (b)

Figure 5.6: (a) Behavior of the velocity measurements, simulated measurements with different assumed intensities. (b) Data showing the distribution of the measured reference position for the rest frame wavelength in pixel, measured during different discharges within one day of operation (30th January 2008).

As has been pointed out, the absolute accuracy strongly depends on the photon statistics. The present status of the diagnostic utilizes the described direct imaging to supply as much intensity to the spectrometer as possible. The poloidal diagnostic produces very good results with respect to the relative accuracy (0.7 km/s) which only depends on the light gathered and transported by the observation system on top of the tokamak vessel. But the reference channel from the vessel bottom is still transfered via fiber optics(as can be seen in figure 4.7. Those signals suffer from small intensities compared to the directly imaged main observation on the vessel top.

Figure 5.6(b) shows data accounting for the determined wavelength reference position (equation 4.12) based on one upper and the single lower channel. This shows that a spread of a few pixels is possible when relying on a single measurement of the reference position.

Since the spectrometer components are not in anyway influenced or moved during the measurement campaign, it is assumed that the actual reference position is not changing from discharge to discharge. The calculated average position is reasonable and its uncertainty is well below one pixel $(2.41\,pixel/\sqrt{26} = 0.47 \rightarrow 0.2km/s)$ (cf fig.5.6(b)) and in this case small compared to the relative uncertainty of 0.7 km/s.

With the described accuracy this system is well equipped for the measurement of small poloidal rotations, of the ion temperature and toroidal rotation.

Chapter 6

Results

This chapter will focus on the results obtained with the diagnostic setup presented in the previous chapters, which will be complemented by a number of other TEXTOR diagnostics.

As has been already stated in chapter 2.2 the results on plasma rotation will mainly be presented and discussed in terms of the radial electric field and its contributions as given by the radial force balance 2.32, the diamagnetic, the poloidal and the toroidal terms.

We will concentrate in the description of E_r because this is a general and unique quantity, while the rotation of carbon and background ions can be different as described in chapter 2.

The data will be presented in terms of rotation only if necessary for comparison with calculations or in order to put the profiles and measurements in perspective with recent other results.

In order to introduce the measurements and give an assessment for the connection between the measured quantities like the rotation and the electric field contributions section 6.1 will demonstrate the general behavior of plasma rotation in TEXTOR, while 6.2 will focus on the general effects of the external magnetic perturbations on the plasma rotation. Section 6.3 will then in detail discuss the results on the influence of the DED with respect to global confinement properties as seen during Improved Particle Confinement (IPC, section 6.3.1) the particle Pump Out (PO, section 6.3.2) scenario.

The observed phenomena, the interpretations and implications for plasma confinement and operation of external magnetic perturbation for the plasma confinement will be given and possible interpretations described. In the end this will lead to a coherent picture for confinement changes with the Dynamic Ergodic Divertor at TEXTOR.

6.1 Rotation and Radial Electric Field without DED

In general the plasma rotation is given from the equations in the sections 2.2.2. The rotation discussed below is the C^{6+} rotation as has been described in chapter 5, which means that it might differ from the rotation of the background ions (hydrogen, deuterium).

6.1.1 Influence of Neutral Beam Injection - Toroidal Torque

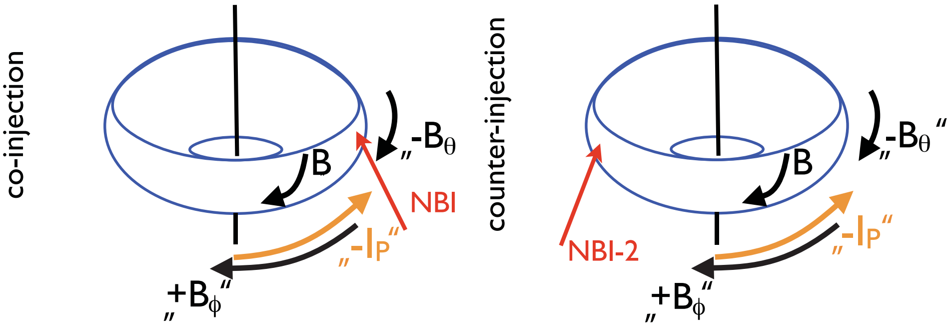

(a) $(+B_T, -I_P)$ co-injection

(b) $(+B_T, -I_P)$ counter-injection

Figure 6.1: The co and counter beam injection at TEXTOR, displayed for the case of the given field and current configuration. The NBI directions are shown in comparison with field and current.

Neutral beam injection is used at TEXTOR for two purposes, firstly in order to apply additional heating (up to 4 MW) to the plasma and secondly to apply external momentum to the plasma. The following example is a series of discharges with constant input power of $1.3\,$MW from two neutral beam injectors (co and counter current), a toroidal field of $2.1\,$T and a plasma current of $410\,$kA. In the course of the different discharges the total torque applied by the two tangentially located heating beams is gradually changed from full co current (-) (#106850) as displayed in figure 6.1(a) via balanced beam (#106848) to full counter current injection (+)(#106846) as shown in figure 6.1(b). The total heating power is kept constant.

This rotation sweep allows it to study the behavior of plasma impurity (C^{6+}) rotation for the poloidal and toroidal direction during external momentum input. It also allows to judge the viability of the measurement procedure. The TEXTOR plasma during this discharges was centered around a major radius of R=1.75 m and had a minor radius of $r = 0.46\ m$, locating the last closed flux surface at $R \simeq 2.21\ m$.

The neutral heating beam was applied during a phase from 1.2 s - 4.8 s. The RuDI diagnostic was operated for 3 s from 1.5 s to 4.5 s. The line-average electron density (n_e) was measured with the HCN interferometer as $\sim 4 \cdot 10^{19} m^{-3}$. The central electron temperature stayed constant at about 900 eV (cf 6.2).

Toroidal Rotation

The first set of data presented in figure 6.3 shows the influence of momentum input on the toroidal rotation in TEXTOR, in addition the contribution to the radial electric field is shown. It is visible that the momentum input from the neutral beam has the biggest impact in the center of the plasma.

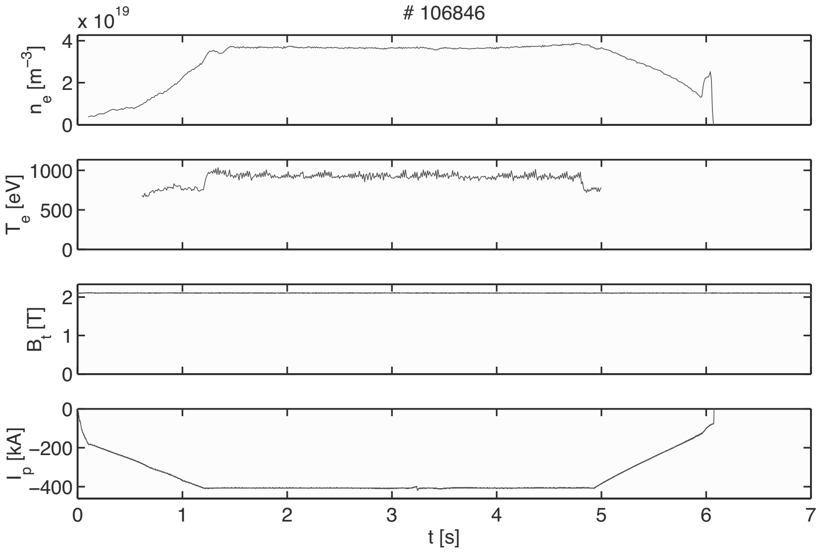

Figure 6.2: Shot parameters during the first discharge of the rotation scan. All following discharges 106847-106850 are similar. Shown are the line-averaged density, the electron temperature, the magnetic field and the plasma current.

The rotation in a tokamak during ohmic or balanced beam injection always tends to be driven slightly into the counter current direction [Kim 91, Rice 97]. The motion is following the toroidal drift of the electrons. A small contribution of the rotation always points in the counter direction, following the elctron drift. The yellow curve in figure 6.3 shows a case with both beams equally contributing to the plasma heating and the rotation still being slightly positive (counter).

The changes in momentum input can be observed across the whole profile except over the Scrape of Layer SOL area beyond R=2.20 m, where the profiles are underlying a general flow into the counter direction [Lehnen 01, Zagorski 02] (cf pp. 77) under standard TEXTOR setup $(-I_p/+B_\phi)$ (cf. figure 3.3 6.1(a)). The rotation is slowed down in the plasma edge caused by friction with neutral particles and is connected to the SOL flow. The profile structure can be explained by the perpendicular viscosity, keeping the outer part connected to the innermost momentum source.

All rotation profiles as well as the profiles for toroidal contribution to the radial electric field $E_r(tor.)$ can be distinguished outside of the one sigma error bars over the whole radial range.

All the systematic corrections applied (Zeeman, fine structure pp. 40 sqq.) including the finite slit height correction (pp. 55 sqq.) are smooth functions of the radius and hence cannot cause sudden changes or unsteady behavior of the profiles.

In the case of the toroidal system the radial channels do not overlap, hence the profiles are not artificially smoothed by gathering light from neighboring channels. In general the toroidal

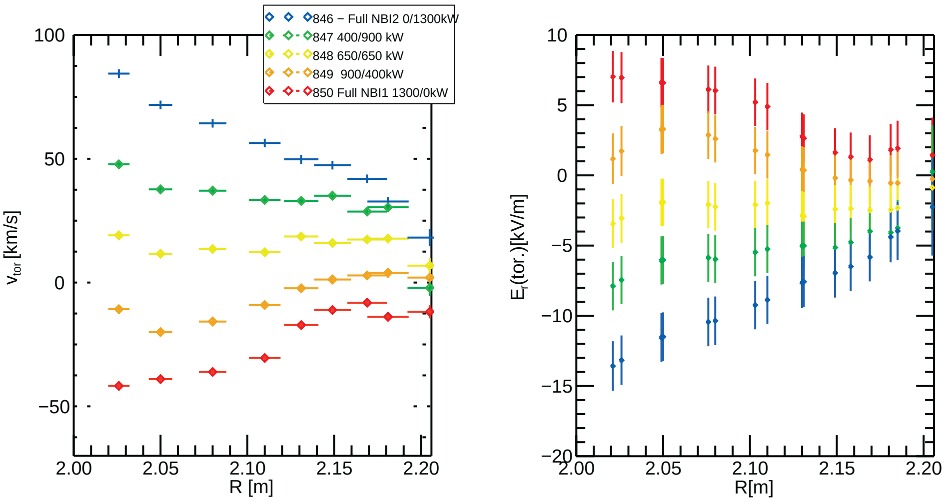

Figure 6.3: Toroidal rotation data during a momentum input / NBI torque scan, changing the momentum fraction between the two neutral beam injectors but keeping the input power constant.

profiles available from the RuDI CXRS system are better resolved with smaller uncertainties when compared to the NBI CXRS system.

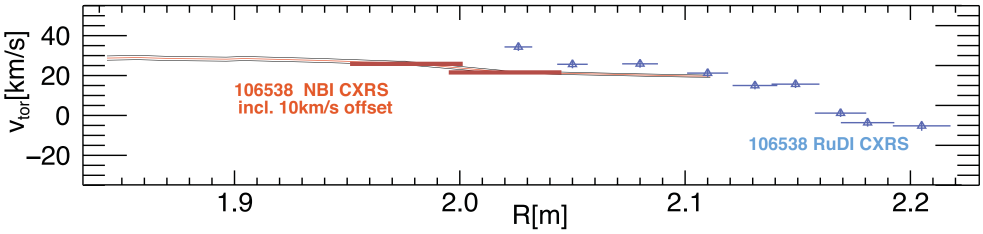

Figure 6.4: Comparison of the NBI and RuDI CXRS regarding the toroidal rotation. #106538.

This NBI CXRS system suffers from a larger systematic uncertainty in the absolute wavelength calibration in the order of 10 km/s [Delabie 08], absolute measurements are thus difficult when needed in the range of 1 km/s. The radial resolution ($\sim$ 5cm) is too large to distinguish local effects, especially in the plasma edge.

From discharge #106538 a comparison of the two systems is available, showing that when considering the systematic offset, both profiles can be brought into agreement (see figure 6.4), especially when considering the large radial uncertainty of the NBI CXRS system. The systematic error for the absolute calibration is not critical for the RuDI CXRS system due to the used mounting method 4.2.3, not causing an angular deviation between measurement and reference channels. Using both systems the whole minor radius is covered.

The shape of contribution to the radial electric field by v_ϕ connects directly to the shape of the toroidal rotation when folding it with the poloidal magnetic field profile. If the plasma rotates more in the counter direction the radial electric field is more negative and vice versa.

The errors bars for the radial electric field and its contributions are originating from the uncertainties of the rotation measurement and mainly from systematic errors determining the magnetic field components (cf. [Testa 06]).

Poloidal Rotation

Figure 6.5 shows the profiles of the poloidal rotation for the NBI torque scan. In the center of the plasma the rotation follows the trend of increased momentum input. Here the ion diamagnetic drift direction corresponds to negative rotation values and the co-direction when talking in terms of toroidal rotation. The poloidal rotation is influenced by the toroidal torque since the beam is not tangential to the flux surfaces. The momentum input has a component into the poloidal direction when performing the flux surface average.

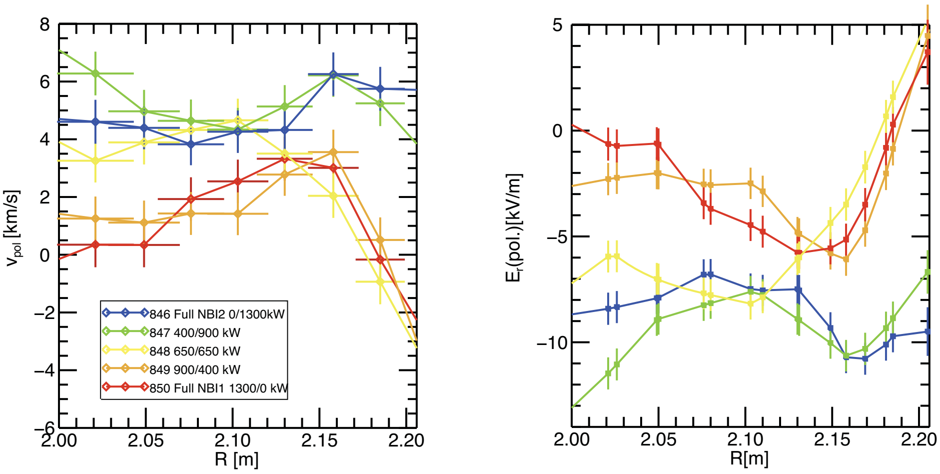

Figure 6.5: Poloidal rotation data for the same momentum input scan as presented in figure 6.3.

In addition to this momentum induced feature a more general feature can be observed which will gain some importance in section 6.1.2: The poloidal rotation is predominant into the electron diamagnetic direction. This has also been seen by previous active hydrogen CXRS measurements at TEXTOR [Busch 06] and is being supported by measurements on intrinsic carbon impurities at other machines [Severo 03, Condrea 99].

While the momentum input might explain the changes in the plasma center from the electron diamagnetic drift direction (edd, Counter(+)) towards the ion diamagnetic drift direction (idd, Co(-)) it can not explain the changes close to the plasma edge.

Only the discharges with dominant NBI 2 injection show the strong increase in edge rotation, hence a connection with the different ion confinements for the two beams can be assumed.

It has been estimated from calculations [Ongena 08b, Ongena 08a] on a similar scenario that about 8 % of the beam ions ($2.6 \cdot 10^{20}$ particles/s) are lost via orbit losses when using the counter beam. The co-beam has a much lower loss rate. Qualitatively this can explain the change in poloidal rotation due to an electron return current and the corresponding change in the radial electric field towards more negative values, counteracting the ion loss.

The Total Radial Electric Field

Following equation (2.32) the radial electric field can be calculated from contributions of the pressure gradient ($\sim$ the ion density times temperature) and the rotation in the toroidal and poloidal direction. This is valid as long as being used on a single ion species since the different field contributions (cf equation 2.32) might differ when deduced from different ion species (carbon, hydrogen, deuterium).

The pressure gradient calculated from the plasma pressure ($p = nk_BT$) is usually negligible. This can be seen in figure 6.6(a) and has already been observed by [Busch 06]. It is typical for TEXTOR and other L-Mode plasmas [Ida 98].

In case of the presented discharges, which have a significant momentum input from neutral heating beam, the toroidal contribution $v_\phi B_\theta$ dominates the radial electric field in terms of absolute value. Especially in the plasma center the E_r profile shape is basically given by the rotation profile. The poloidal contribution, on the other hand, dominates the effects in the plasma edge.

The radial electric field at the plasma edge is mostly determined by the poloidal rotation. The magnetic fields ($B_\phi/B_\theta \simeq 10$) contributing to either component of the electric field differ in one order of magnitude. It is clear that even the small poloidal rotations can have a significant influence at the plasma edge, where the toroidal magnetic field is much larger than the poloidal field.

As can be seen from the poloidal force balance (cf. equation 2.25 p. 18)

$$\begin{aligned}
\alpha(V_\theta - V_\theta^{neo}) \; = & \\
& - \; \langle j_r \rangle B_0 \;\; \text{(radial currents)} \\
& + \; (F_\theta - 2q\langle F_\phi \rangle) \;\; \text{(ext. Forces, NBI)} \\
& - \; (1 + 2q^2) m_i n_i \nu_{i0} V_\theta \;\; \text{(Collisions \& CXRS Friction)}
\end{aligned}$$

the poloidal rotation is governed by several localized momentum sources (and sinks) causing deviations from neoclassical poloidal rotation (cf. section 6.1.2).

The poloidal rotation is only following the neoclassical theory when the right hand part of the above equation is zero. The assumption, obviously not valid, would neglect any momentum sinks and sources. Section 6.1.2 will show the comparison to neoclassical calculations.

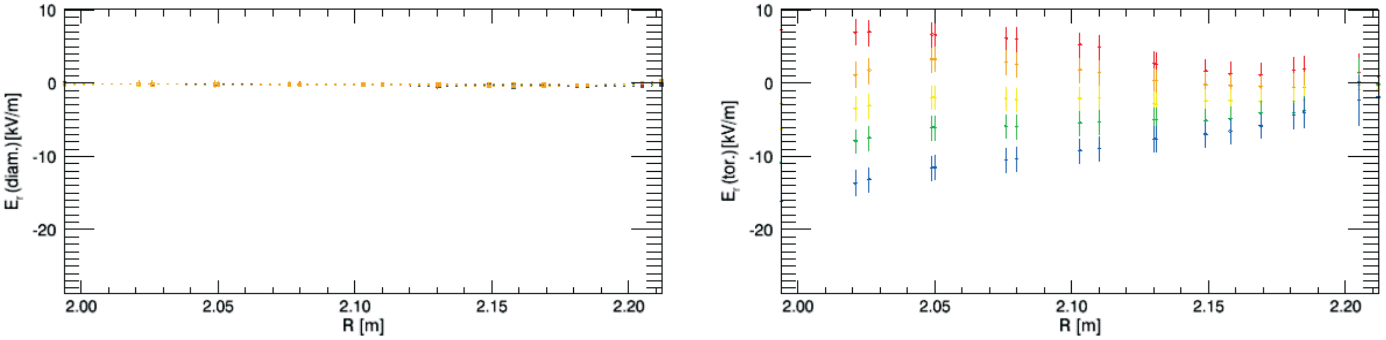

(a) Diamagnetic contribution to E_r as given in equation (2.33)

(b) Toroidal conribution to E_r as given in the radial force balance (cf. equation (2.35))

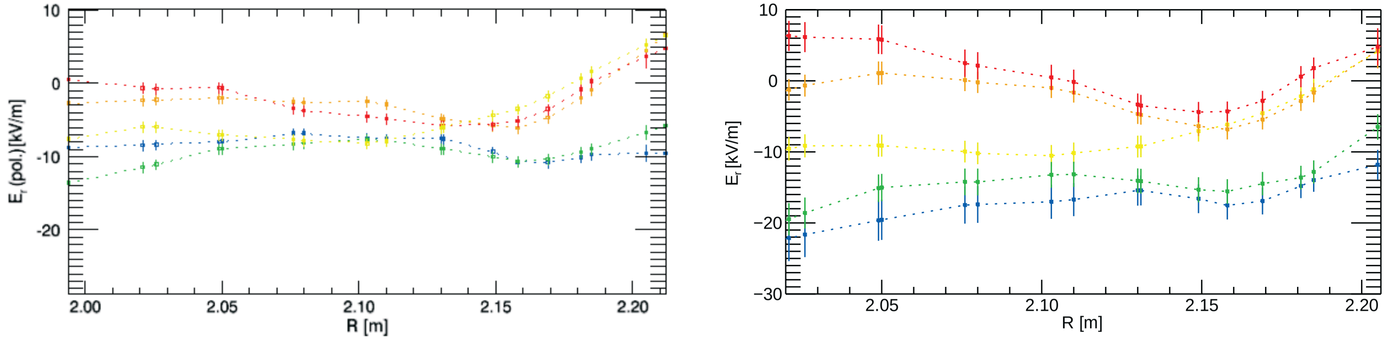

(c) Poloidal contribution to E_r as given in the radial force balance (cf. equation (2.34))

(d) E_r as given in the radial force balance (cf. equation (2.32))

Figure 6.6: Main contributions to the radial electric field during a momentum input scan. Changing the momentum fraction between the two neutral beam injectors, keeping the input power constant.

Taking a closer look at the balanced beam scenario (discharge #105848, central yellow curve in figure 6.6(d)) one can see that even for a scenario with no net momentum input, the rotation values differ from zero and the radial electric field is negative almost over the whole profile. The dominant contribution to the negative E_r again originates from the poloidal term where the rotation is in the electron diamagnetic drift direction. This effect can be explained at least partially, when using the equation for the neoclassical electric field and the neoclassical poloidal rotation 2.24 (cf. section 6.1.2).

The negative E_r can be understood from the qualitative neoclassical approach for deuterium ions:

$$E_r^{neo.} \propto \nabla p_{ion} - v_{\theta,ion}^{neo.} \cdot B_\phi = \nabla p_{ion} - \frac{0.5}{eB} \nabla T_i \cdot B_\phi \qquad (6.1)$$

Taking into account the pressure profile as well as the temperature gradient one can deduce that their values are predominantly negative over most of the plasma profile represented here. This means that for the radial electric field the resulting value is also negative.

6.1.2 Impurity Rotation in Scenarios with Negative field Line Helicity

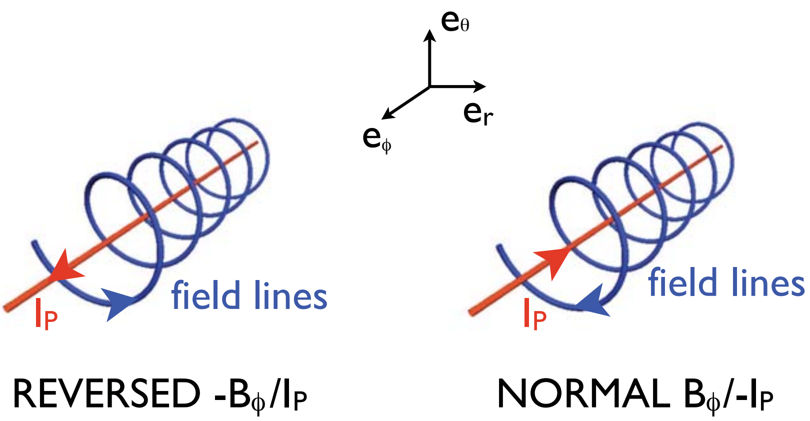

Figure 6.7: Fieldlines at TEXTOR with negative helicity

At TEXTOR it is possible to perform experiments with the REVERSED configuration, meaning positive I_p and negative B_ϕ. In principle this reverses the drift direction, but preserves the magnetic field geometry [Lehnen 00, Lehnen 01] and the helicity $h = sign(I_p \cdot B_\phi) = -1$. This allows a more detailed view on the source and sinks in the poloidal force balance.

For later analysis of the measured data in section 6.2, we have to consider here both the potential differences and similarities between the two setups with $h = -1$. Since especially the poloidal rotation is important for the profile shape of the radial electric field a focus will be laid on the understanding of the poloidal rotation behavior in general and during field reversal in particular.

In order to understand the effect of field and current reversal as well as the different contributions to the plasma rotation a few aspects of momentum input (NBI torque) and plasma edge rotation shall be discussed in detail especially with respect to the neoclassical approach.

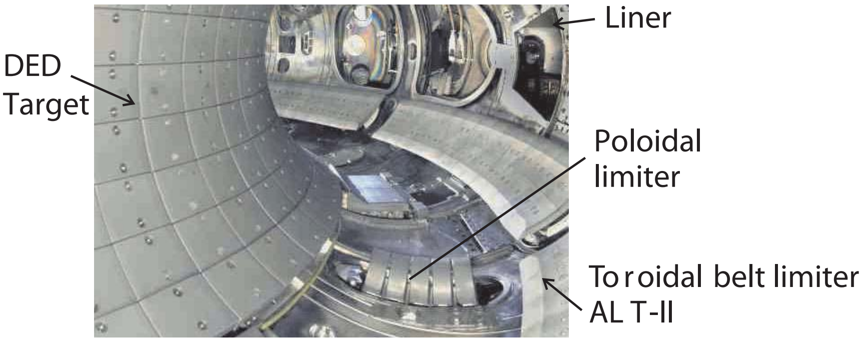

Figure 6.8: In-vessel view of the TEXTOR tokamak, showing the toroidally symmetric ALT-II belt limiter at a poloidal position of -45 °.

A few remarks need to be made about the geometry of the torus itself in order to understand the symmetries applicable at TEXTOR. On the one hand the torus itself is toroidally symmetric, which means that when reversing field and current and —keeping the field geometry identical— nothing should happen except for the drift reversal. On the other hand the TEXTOR tokamak is not poloidally symmetric (In-vessel components such as Limiters), thus an effect of this reversal procedure will manifest itself on density profiles and probably on the rotation of the plasma itself due to the reversal of drifts.

The largest structure inside the tokamak vessel which is causing the non symmetry is the ALT-II toroidal belt limiter (cf. figure 6.8, figure 4.3 - pp. 42).

In the experiments that have been performed for this work, all plasmas have been limited by this structure, causing the scrape off layer (SOL) and the Last Closed Flux Surface (LCFS) to be defined by the ALT-II position at a minor radius of $r = 46\,\text{cm}$.

If one takes two similar discharges (#106584, #106577) differing only in the setup of magnetic field and current as well as a small amount of NBI heating (torque) one will observe two distinctly different behaviors for the poloidal and the toroidal rotation.

Neutral Beam Injection - Coordinates

As seen in section 6.1.1, where it was demonstrated by switching from co to counter beam injection, the momentum input can have a large influence on the rotation profiles when e.g. switching from co to counter beam injection. This is also true of course when reversing the magnetic field configuration. One point needs to be discussed for the further understanding: when reversing the configuration one has obviously to switch to the opposite NB injector. This is due to the fact that in order to compare e.g. two discharges (NORMAL vs REVERSED) on has to make sure they would be both heated in the same direction with respect to the plasma

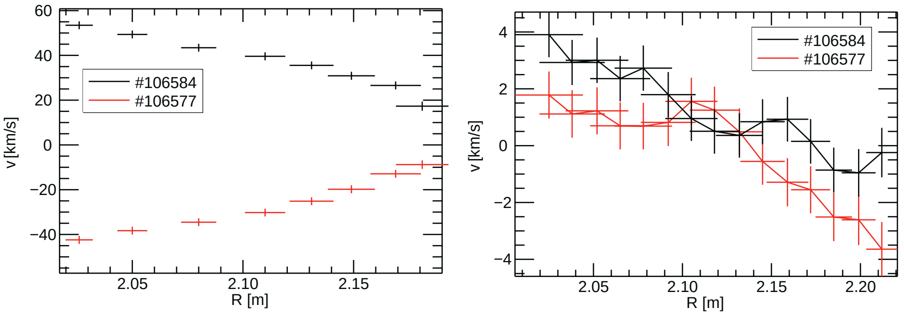

(a) Toroidal rotation

(b) Poloidal rotation

Figure 6.9: Rotation data for NORMAL (B_ϕ, I_P) (black) and REVERSED (B_ϕ, I_P) (red). Discharges differ slightly in the amount of counter NBI heating (NORMAL: 1 MW, REVERSED: 0.6 MW).

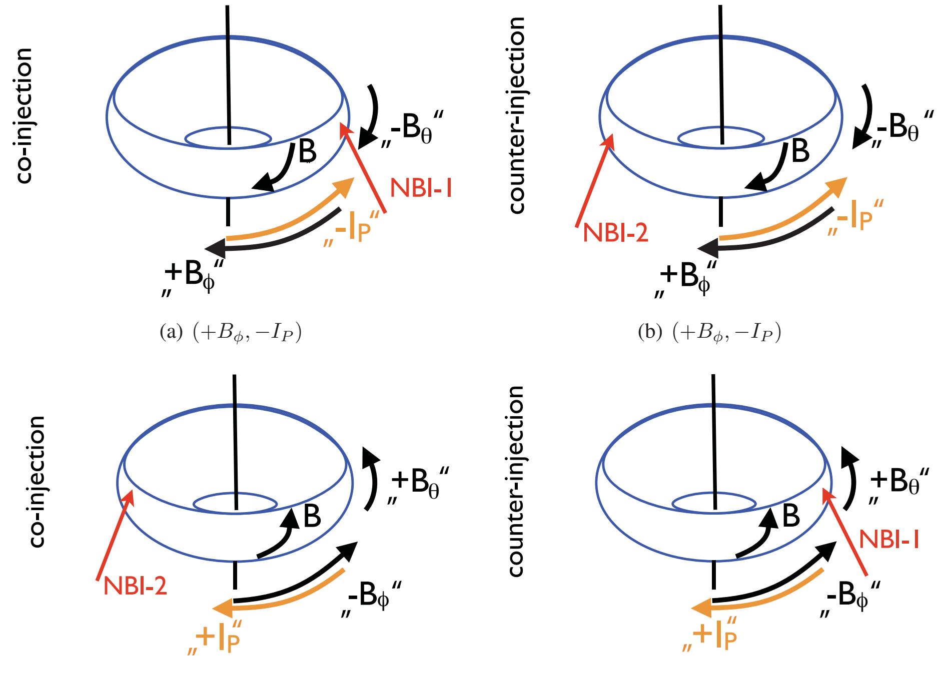

(a) $(+B_\phi, -I_P)$

(b) $(+B_\phi, -I_P)$

(c) $(-B_\phi, +I_P)$

(d) $(-B_\phi, +I_P)$

Figure 6.10: All four possible heating scenarios available with helicity $h = -1$ at TEXTOR.

current and magnetic field. The NBI torque has to be the same. For the toroidal rotation this means a forced reversal of plasma rotation, for the poloidal rotation it means a reversal of the source term (external momentum - NBI) influencing the poloidal rotation, hence contributing to the poloidal rotation in the opposite direction too.

Figure 6.10 demonstrates this in terms of coordinates and NB input directions. The upper row shows sketches for co and counter injection for the NORMAL configuration, while the lower row shows the REVERSED case. NBI-1 injection switches from co to counter injection beam and NBI-2 vice versa. This means that a co-injected beam during the NORMAL scenario would cause a momentum input into the negative direction, while co- injection during the REVERSED scenario would mean momentum input in the positive direction (the coordinate system does not change).

Figure 6.9 demonstrates this effect for the toroidal rotation and in addition shows the poloidal rotation profiles. Both discharges are dominantly heated by the respective counter beam causing the toroidal rotation to turn into the counter direction. The slight difference in absolute amplitude is caused by a difference of about 400 kW in heating power, the REVERSED case getting a slightly lower momentum and heat input. It is seen that the toroidal rotation is very sensitive to momentum changes, and it is mostly dominated by it.

The poloidal rotation also shows changes in rotation when reversing the setup. While neoclassically the rotation remains in the electron diamagnetic drift direction the local changes are due to momentum input from external sources.

In the core the change in rotation is connected to the change in momentum input. When comparing this plot with the torque scan (cf. figure 6.5) the change is consistent with the amount of beam power applied. The change in momentum source changes the poloidal rotation locally in the plasma core. This is a deviation from the neoclassical approach which neglects this kind of momentum sources. In order to understand the deviations from the neoclassical profile shape in the outer edge of the plasma, the effects like SOL flow and drifts have to be considered.

Edge Rotation and SOL flow and Drifts

Inside the SOL the particles are subject to a flow due to a pressure gradient to the nearest target (cf. 2.1.3) parallel to the magnetic field and drifts perpendicular to the field line direction. Both motions have components in the toroidal and poloidal direction [Lehnen 00, Lehnen 01].

Since the observation volume is located on the low field side the nearest target is the ALT-II limiter. This means that the toroidal rotation is forced into the positive direction and the poloidal rotation into the negative direction if considering the flow to the target, as can be seen from figure 6.11. This does correspond well with the data presented in section 6.1.1.

Since we keep the helicity h negative, the simultaneous inversion of field and plasma current does not change the direction of the scrape off layer flow and hence its contribution to the rotation. This can explain the typically negative values of the poloidal rotation in the outer edge as well as the typically positive values of the toroidal rotation in the plasma edge due to viscous coupling to the SOL flow.

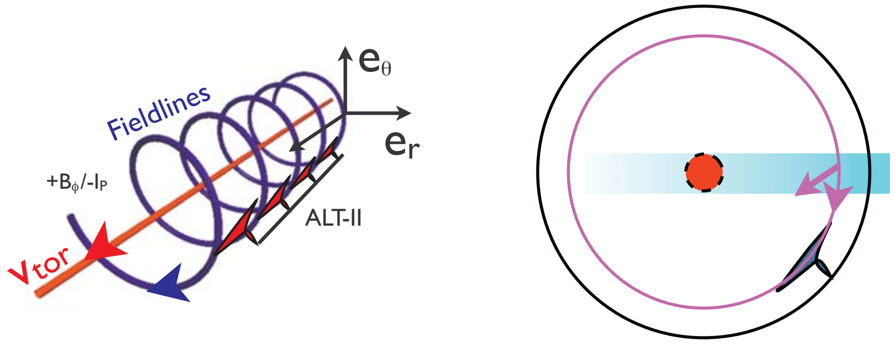

(a) Sketch of field line Configuration at TEXTOR for the NORMAL configuration ($+B_\phi/-I_P$). Field line helicity does not change with simultaneous reversal of field and current, but the arrows change direction. The red arrow shows the toroidal rotation during ohmic discharges. It coincides in this case with the SOL flow direction.

(b) Sketch of flow directions (projections along field lines) inside the SOL, assuming the shortest connection to the target from the observation volume (RuDI Beam, blue). This is independent of the simultaneous (B_ϕ/I_P) reversal which keeps the helicity constant. .

Figure 6.11: Field lines near the ALT-II limiter causing a "constant" SOL Flow to the target..

The differences between the NORMAL and REVERSED case, especially in the poloidal rotation may well be given by different drift direction when reversing magnetic field and current. A comparison with data from [Lehnen 00] shows comparable tendencies, an exact comparison is lacking due to different NBI heating directions. Whereas for the toroidal rotation the external momentum input can play a significant role, as seen before, the poloidal rotation in the edge is most likely dominated by effects originating from the SOL, even though the center is following the NBI momentum input.

Poloidal Rotation Measurements vs. Neoclassical Theory

In section 2.2 a short introduction into the equations describing the plasma rotation has been given including the neoclassical description and the poloidal force balance. The following discussion is based on the work of [Kim 91, Testa 06] where a neoclassical description has been developed for the poloidal and toroidal rotation of carbon and deuterium plasma.

The toroidal rotation, especially the beam induced toroidal rotation, is described satisfactorily by the momentum balance equations and work from [Kim 91, Rice 97, Rice 04, Testa 06, Yoshida 08]. In contrast to this, the behavior of the poloidal rotation lacks the complete neoclassical description of the measured profiles, as already shown in [Testa 06, Solomon 06, Wong 08]. The momentum sources and sinks play an important role for both rotations mostly not covered by the neoclassical approach.

Taking into account equations 2.29 & 2.30 for a two component plasma (D^+, C^{6+}) one can see that keeping the helicity unchanged also keeps the poloidal rotation signs. Differences arise due to different gradient lengths and different collision parameters K_1 and K_2 which might differ

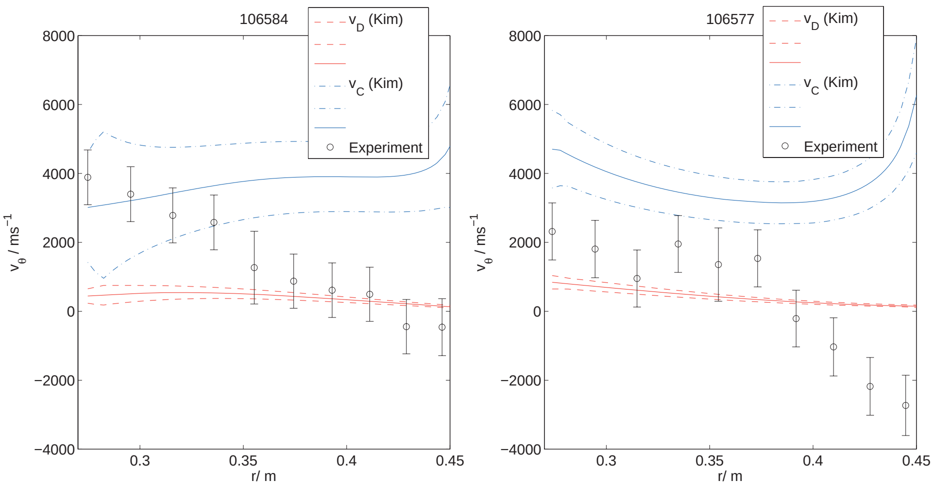

(a) Discharge 106584 with $+B_\phi, -I_P$, NORMAL (b) Discharge 106584 with $-B_\phi, +I_P$, REVERSED

Figure 6.12: This figure presents calculations of the neoclassical poloidal deuterium and carbon rotation (based on [Kim 91, Testa 06]) for both the NORMAL and the REVERSED TEXTOR configurations. The solid lines represent the calculated rotation profiles with the error bar given by broken lines in the according color. (cf. equations 2.29 & 2.30).

for different shots, but should be similar for the two shots compared (only reversal of field and current). The background profiles for the compared discharges are the same.

Figure 6.12 shows the profiles calculated according to equations 2.29 & 2.30) for v_θ. The deuterium and carbon rotation as well as the measured data are shown in comparison. One thing that stands out is that, although neither the profiles for deuterium nor for carbon match the measured data they do however not change sign during simultaneous reversal of the toroidal magnetic field and the plasma current and at least show the correct sign of the rotation into electron diamagnetic drift direction. Carbon as well as deuterium are both rotating in the counter direction, but the deuterium rotation is negligible when being compared to the amount of carbon rotation.

The calculations are based on the profiles of electron and ion temperature (the last supplied by the CXRS RuDI diagnostic) as well as electron density, poloidal and toroidal magnetic field. The uncertainties for the input parameters are reflected by the broken lines.

Only the measurements near the center of the plasma do agree to some extent with the calculations. They do not exactly match with each other (NORMAL vs. REVERSED). The difference between the two shots however may be explained by the small difference in heating power and the different momentum input. The work of Wong et al. [Wong 08] also showed a strong influence of the central momentum input on the calculations for neoclassical poloidal rotation. The edge of the plasma does not agree with model calculations at all. This might have several reasons, of which probably the influence of the SOL due to viscous coupling and the dampening due to neutral particles may be the most important factors.

The model calculations are based on an analytical description of the collision and friction factors for the different collisionality regimes present over the whole plasma radius [Kim 91, Testa 06]. This analytical solutions are most reliable for the banana regimes (cf. 2.1.2) but is most unsuited for estimations in the plateau regime near the plasma edge. This means that the SOL flow as well as the uncertainties in the calculation are the probable reason for the deviations.

Plasma rotation during field reversal In summary the following statements can be put forth. The toroidal rotation changes sign during REVERSED configuration discharges mainly due to the contribution of the reversed neutral beam injector setup.

In ohmic discharges the toroidal rotation would reverse as well since it depends on the sign of the loop voltage considering the approach given by Kim and Rice [Kim 91, Rice 97]:

$$V_\phi^I = 4.19 \times 10^2 f \frac{Z_i}{\sqrt{\mu}} \frac{V_l}{R} \frac{T_i^{3/2}}{n_i} (km/s) \tag{6.2}$$

μ is the atomic mass of the background ions in amu, V_l the loop voltage in volts, R the major radius in cm and T_i the ion temperature in keV. n_i is the ion density in 10^{14}cm^{-3}.

The poloidal rotation however does not change sign in the inner parts of the plasma probably explainable due to neoclassical effects. However, the experimental data shows the importance of sorces and sinks for the poloidal rotation profile (NBI, and in the outer part of the plasma viscous coupling to the SOL flow)

The differences, however, between NORMAL and REVERSED configuration seen in the poloidal rotation at the plasma edge are most probably caused by the changes of drift directions as given in [Lehnen 00] showing a more negative SOL flow during REVERSED setup then for the NORMAL configuration.

6.2 Rotation and Radial Electric Field under the Influence of the DED

6.2.1 Changes in the Radial Electric Field

As we have seen in the last section the measured rotation strongly depends on the magnetic configuration and hence on the changes in the intrinsic coordinate system with respect to the laboratory frame system (co, counter, vs. [+],[-]).

Especially the very small poloidal rotation, which is very sensitive to changes in the plasma transport and magnetic topology due to the low viscosity, is behaving counter intuitively (even though consistent with theory) during field reversal: it does not change sign due to the helicity being preserved (cf. equations 2.29 & 2.30 and figure 6.12).

While the toroidal contribution to the electric field does not changes sign, the poloidal contribution does change sign and changes the whole radial field profile when reversing the configuration. The E_r profiles are not very similar in their shape when compared between NORMAL and REVERSED setup. The poloidal contribution either adds to the radial field or counteracts the toroidal contribution.

In order to judge the influence of the DED to radial electric field we apply a method that eliminates those different behaviors and allows a shot by shot comparison.

In the following discussion of the results we follow a certain procedure when comparing discharges with identical setup, except for the B_ϕ/I_p configuration:

1. Compare general discharge parameters
   - Plasma Position
   - Electron Density (n_e)
   - Electron & Ion Temperature
   - H_α Emission
   - Neutral Beam Heating Power
   - Total Power
   - DED Amplitude (I_{DED})
   - Plasma Current
   - Toroidal Magnetic field

2. If discharges are comparable take the unperturbed discharge (e.g. 0 kA DED) as a reference for the further analysis

3. Use the following quantities for the analysis :
   - $\Delta E_r(all.) = E_r(all.) - E_r^{ref.}(all.)$
   - $\Delta E_r(tor.) = E_r(tor.) - E_r^{ref.}(tor.)$
   - $\Delta E_r(pol.) = E_r(pol.) - E_r^{ref.}(pol.)$

On the one hand the absolute values of the radial electric field are important, on the other hand the changes caused by the DED, including changes in particle confinement and magnetic topology will be very well visible also in the Δ profiles.

The advantage of doing so is twofold. Firstly, taking the radial electric field presents quantities that do not reverse sign during switching between NORMAL and REVERSED setup and secondly taking the delta values produces data which, except for topological or minor transport changes, should be comparable over the two scenarios. This procedure allows to resolve topological effects visible by changes in the poloidal rotation on the one hand caused by increasing the perturbation amplitude and on the other hand by shifting the magnetic topology toroidally due to the field reversal with respect to the DED coils.

6.2.2 DC DED - Stochastic Force

As has been described in section 3.3.1 and [Xu 07, Kramer-Flecken 06, Busch 06, Unterberg 07] the dynamic Ergodic Divertor can have a significant influence on particle transport and rotation in the plasma edge due to strong parallel electron loss in the ergodic zone in the plasma edge.

Even though the focus of this work will be put on the role of the E_r for the Improved Confinement Scenarios presented in section 6.3 a short overview on the general effects of stochastic magnetic fields on the E_r will be given here focussing on the radial electric field and the changes in plasma rotation connected to the amount of magnetic perturbation (amplitude of the DED current). A new data set for the 6/2 DED base mode is shown below.

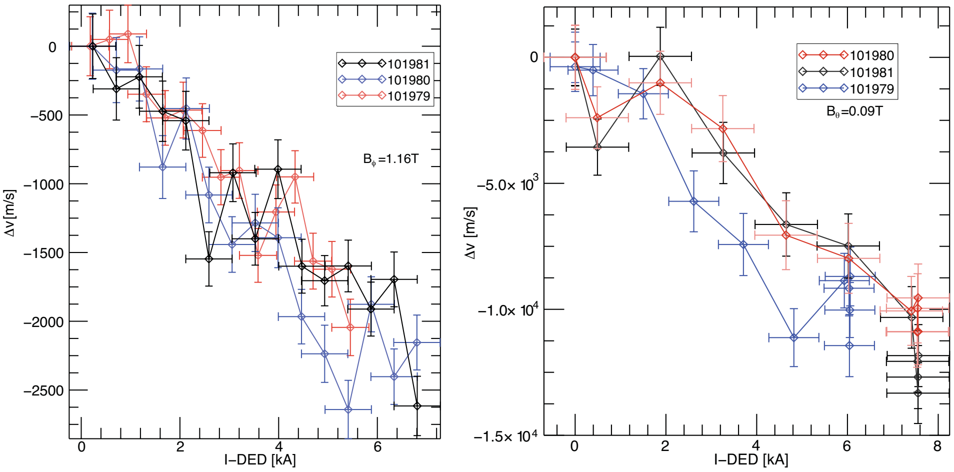

(a) Poloidal rotation

(b) Toroidal rotation

Figure 6.13: Rotation data acquired from CIII emission spectroscopy during DED ramp up, shown in reference to the 0 kA discharge phase.

In order to judge the effects more closely this data will consist of discharges covered by measurements on the intrinsic carbon emission (passive spectroscopy on CIII , $\lambda = 464.7\,\mathrm{nm}$) as described in section 5.2 obtained during 6/2 operation of the Dynamic Ergodic Divertor.

The discharge parameters are : B_ϕ = 1.4 T, $\overline{n_e}$ =1 10^{19} m^{-3} I_P = 200 kA, DED: m/n= $6/2$

This data allows a local, time resolved (30 ms) measurement of the rotation, and hence the radial electric field, when ramping up the perturbation, namely the DED current. The CIII emission is localized inside a small shell just inside the LCFS [Claassen 90]. Figure 6.13 shows for both contributions the influence of increasing perturbation (DED current). The DED amplitude is ramped up within 0.5 s to a maximum amplitude of 7.5 kA.

This effect directly correlates with the simple model put forth in [Busch 06, Unterberg 07], which assumes that, due to the fast loss of electrons a cross field return current is generated that in turn drives a $\vec{j} \times \vec{B}$ force leading to poloidal and toroidal rotation (cf. 3.3).

The torque is exerted perpendicularly to the current and magnetic field and has of course a poloidal and toroidal component with respect to the magnetic field components. This fact is demonstrated in figures 6.13.

The poloidal rotation as well as the toroidal rotation show a stringent trend when increasing the current of the external perturbation coils (DED). With reference to the 0 kA phase the poloidal as well as the toroidal rotation become more negative, hence causing the radial electric field to become more positive.

The poloidal rotation changes towards the ion diamagnetic drift direction and at the same time the toroidal rotation turns towards the co-direction. This rotation is consistent with the direction of the acceleration due to the $\vec{j} \times \vec{B}$ torque. Assuming an ergodic layer of a few centimeter extent the force is in the order of 20 N for the poloidal direction and a 3-4 N for the toroidal direction as has been calculated by Unterberg in [Unterberg 07]. This is consistent with a poloidal spin up of a 2-4 km/s and a toroidal spin up in the order of 10 km/s towards the negative (co) direction as is also visible in the data presented here. With the narrow ergodic layer this would mean a current density in the order of a few $10\,\mathrm{A/m^2}$.

Taking into account this data, the radial electric field E_r is driven towards more positive values. The higher the DED current, the more positive the radial electric field becomes. The maximum excursion is 4 kV/m.

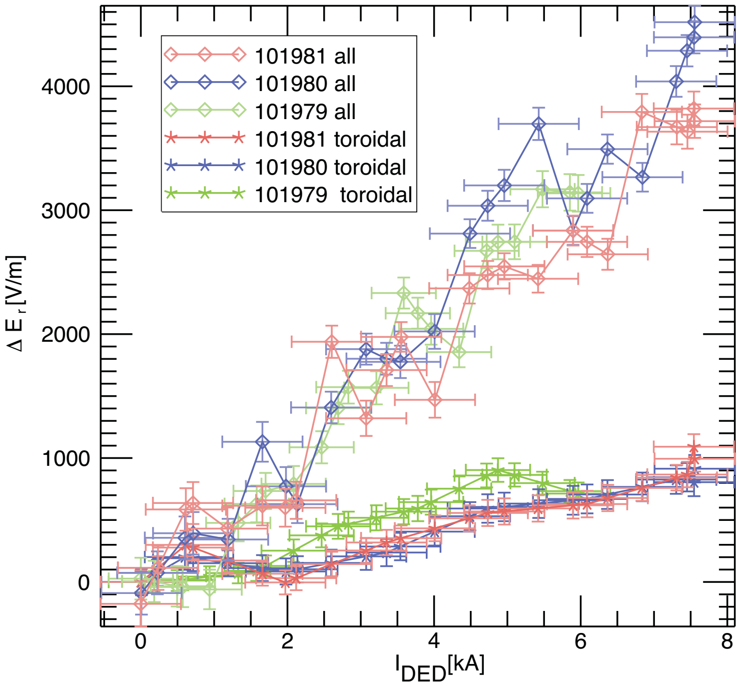

Figure 6.14: Total radial electric field, and its toroidal contribution measured from CIII emission spectroscopy during DED ramp up

The measurements presented here are unique in a sense that the first time they present resolved consistent measurements of the two rotation directions near the LCFS at TEXTOR at the same location and time. They show the effect of ergodization and they do not show significant screening of the perturbation or the equivalent plasma response. The behavior is almost linear for low perturbation but should run into saturation when increasing the perturbation [Unterberg 07].

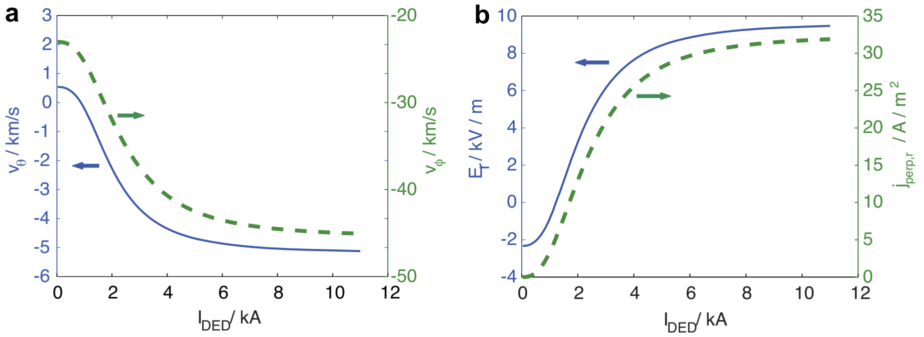

Figure 6.15: Impact of magnetic perturbation expressed as perturbation current I_{DED} on: (a) poloidal (solid line) and toroidal rotation (dashed) and (b) radial electric field (solid line) and transverse current density (dashed)

Field and Current Reversal A set of discharges has been used to check the rotation behavior with DED when being in the REVERSED setup.

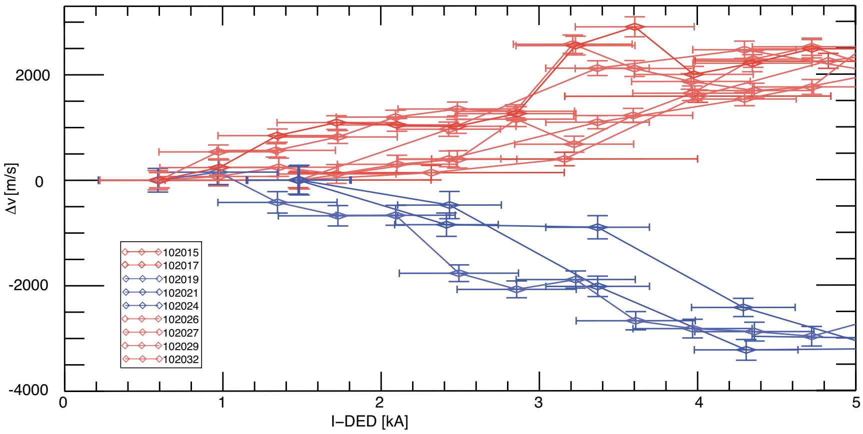

Figure 6.16: Change in poloidal rotation in NORMAL and REVERSED setup, given with reference to the 0 kA phase of the discharge.

The discharge parameters are: B_ϕ = 1.4 T, n_e =1-1.4 10^{19} m^{-3} I_P = 200 kA DED: m/n= $6/2$. Figure 6.16 shows that the electron loss, and there for the ion return current do not change sign, the magnetic field and the direction of the torque change signs.

The poloidal rotation is always directed into the ion diamagnetic drift direction, which for the blue curves (REVERSED) is the positive while for the red curves (NORMAL) the negative direction.

Even the amplitude of the change in rotation is similar, which shows that, even though there is a shift in topologie [Schmitz 08b] when operating in REVERSED setup, the electron losses originating in the ergodic zone remain similar(cf. section 3.2.2), causing the rotation spin up.

The changes between the single discharges are due to the different ramp up times of the DED and the influence of the density changes during that time (bad density control causes different interaction regimes near the LCFS concerning e.g. neutral particle dampening).

The changes in rotation, towards the ion diamagnetic drift direction, are similar to the ones observed in experiments via passive carbon spectroscopy for instance at Tore Supra [Hess 95].

6.3 The Radial Electric Field during Confinement Changes with DED

While in the last section more general effects of the DED onto the rotation and the radial electric field have been discussed this chapter will present two specific scenarios, the so-called Improved Particle Confinement (IPC)[Finken 07a] and as an expansion of this the so-called particle Pump Out (PO)[Schmitz 09]. The application of the DED causes a significant increase or decrease in the particle confinement [Finken 07a, Schmitz 09, Coenen 08] as is sketched in figure 6.17.

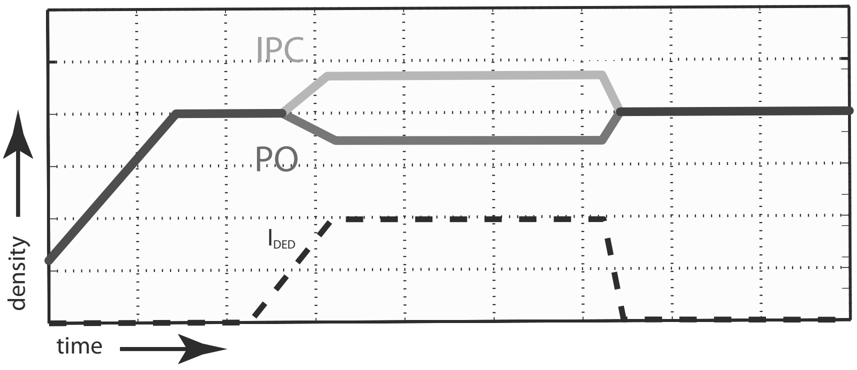

Figure 6.17: Scheme of the density behavior during confinement changes, IPC and PO. Difference between scenarios is in the edge q ($q_a \sim 3.8 \rightarrow q_a \sim 3.4$).

At a threshold amplitude, depending on the value of edge q, plasma current, toroidal B-field and DED configuration, the transition into PO (section 6.3.2) or IPC (section 6.3.1) is triggered.

For this study the DED is operated in 6/2 configuration and the q_a is $q_a = 3.5$ for the PO scenario and $q_a = 3.8$ for the IPC. The transition into IPC or PO occurs at $I_{DED} = 2.5$kA.

Depending on the degree of ergodization, the confinement changes from normal to increased (IPC) or decreased confinement (PO). The two scenarios can even be reached changed into each other (IPC→PO) when applying the perturbation above a certain threshold.

In the following we discuss the role of the radial electric field with respect to local changes connected to the magnetic topology and with respect to the local shear rate $\Omega_{\vec{E}\times\vec{B}}$.

The IPC and PO will be discussed separately. For comparability reasons only data from discharges with negative helicity is considered.

6.3.1 Improved Particle Confinement with Resonant Magnetic Perturbations

The improved particle confinement as such was first described by Finken et al. [Finken 07a] at TEXTOR. It was discovered that when applying the DED several transitions occurred at distinct DED amplitudes ($I_{\text{DED}} = 3.5\text{kA}, 6\text{kA}$). An increase in density can be observed, shown in figure 6.18.

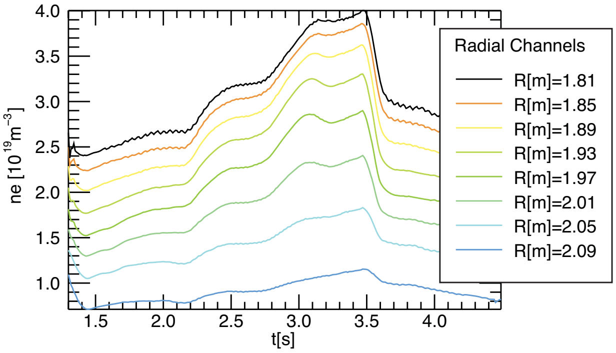

Figure 6.18: Electron density traces during IPC discharge #100972, the DED current is ramped up from 0 kA at 1.5 s to 7.5 kA at 3-3.5 s. Note that the axis zero points are suppressed.

The increase in density was attributed to an increase in particle confinement, caused by the stepwise connection of field lines from deeper island chains to the DED target [Finken 07a, Jakubowski 07]. Later in this section the actual connection between IPC and DED target pattern, hence the magnetic field lines connecting to the target will be made.

Each of the transitions occurs when an island chain is connected via field lines with the DED target, starting at the outermost island chain followed by the next deeper ones. The threshold amplitude (I_{DED}) reproducibly depends on the choice of plasma parameters, especially the horizontal position, meaning the position of the resonant q surface with respect to the perturbation coils (DED)[Schmitz 09].

In the following sections a scan of the DED perturbation current in subsequent discharges is discussed. The discharges are optimized in terms of q-profile and magnetic field to reach IPC

I_{DED}	NORMAL	REVERSED
0.0 kA	106584	106577
2.0 kA	106587	106581
4.0 kA	106586	106580
6.0 kA	106585	106578
7.5 kA	-	106582

Table 6.1: IPC discharges with DED current and shot number

at a certain level of perturbation (I_{DED}=2.5 kA) with only one transition step in the density, connected to only one island chain at around q=5/2. This allows a detailed study of the features connected to the onset of the IPC. The discharges are performed with a set of in total four different currents, 2 kA, 4 kA, 6 kA and in case of the REVERSED setup up one additional discharge with 7.5kA (Table 6.1). The NORMAL and REVERSED discharges are treated as one set of discharges with negative helicity.

General Plasma Parameters and Discharge Conditions

The plasma parameters for both setups (NORMAL, REVERSED) are shown in figure 6.19. Setup: R_0 =1.74 m a =0.47 m, q_a =3.77, R_{sep} =2.21 m with $B_\phi = 2.1$ T and I_P =395 kA and $P_{NBI(counter)}$ =0.6 / 1 MW

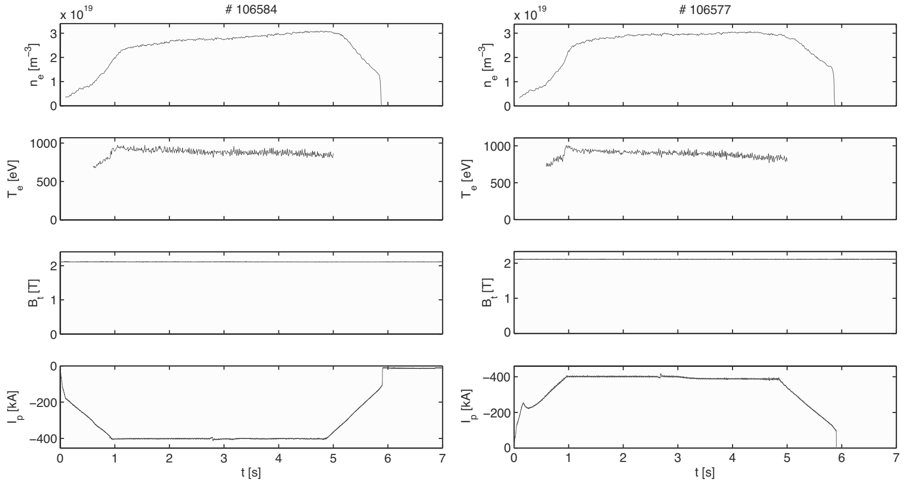

(a) NORMAL SETUP $+B_\phi, -I_P$ (b) REVERSED SETUP $-B_\phi, +I_P$

Figure 6.19: Shot overview for the two IPC reference discharges. Presented are the general plasma parameters including line-averaged density (n_e), the electron temperature (T_e), magnetic field and plasma current (I_P) for the discharges performed during the NORMAL and REVERSED TEXTOR setup.

The overall plasma parameters are kept constant over the whole scan including the switch between NOMRAL and REVERSED discharges. Figure 6.19 shows that this is realized in spite of a slight increase in density is seen. Slight differences in the behavior of the plasma density during the separate discharge are quite common and do not lead to significant changes since it is only in the range of a few percent.

The ergodization of the plasma strongly depends on the edge safety factor [Finken 99a, Jakubowski 04b]. The plasma current and magnetic field are chosen such that the stochastization due to the DED is focussed on the q=5/2 surface (edge q dependence) apart of the already ergodized q=3 surface.

The only difference between NORMAL and REVERSED discharges is the sign of B-field and plasma current as well as the amount of beam heating applied in the respective counter direction. Even though the neutral beam injectors have been operated with the same aperture (V-target) the amount of acceleration voltage was changed slightly in order to allow stable operation of the two beams. The two different heating powers used for the NORMAL and REVERSED setup are presented in figure 6.20(a). The REVERSED discharges are given 400 kW less input power causing slightly different $T_e(\sim 10\%)$ and T_i (Figure 6.20(b)). The total power of the discharge varies between 1MW and 1.4 MW including the ohmic heating power.

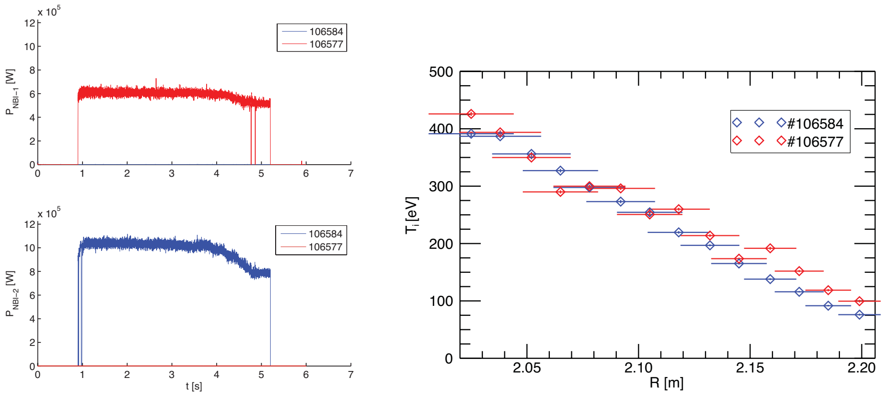

(a) (b)

Figure 6.20: (a) Beam power from both neutral beams during the reference discharge. (b) Ion temperature profile measured with the RuDI Diagnostic (I_{DED} =0 kA). The NORMAL (#106584) and the REVERSED (#106577) setup are presented.

The difference in heating has consequences for the rotation of the plasma, especially the toroidal rotation is being influenced, due to different momentum input. The toroidal rotation is not completely inverted with respect to 0 but has an offset of about 10-20 km/s for balanced torque input. The REVERSED discharges hence rotate less in counter direction than in the NORMAL discharges. This is comparable to the beam induced rotation changes presented in section 6.1. A variation of 400kW changes toroidal rotation in the order of 20 km/s.

The external perturbation is applied via the DED in the so-called 6/2 base mode (cf. figure 3.3, section 3.2), which produces a poloidal mode spectrum with $3 \leq m \leq 9$ centered at m = 5 - 6 and toroidal mode number n = 2. The DED is switched on during a period of 3.5 seconds

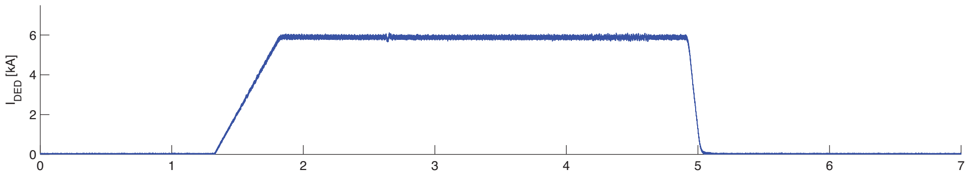

Figure 6.21: Typical I_{DED} development during the presented discharges. Here an example is given, discharge #106578 with 6kA DED current.

as shown in figure 6.21 for the 6 kA case. For each discharge the shape remains, while we systematically scan the DED amplitude. For both the REVERSED and NORMAL setup the perturbation is applied in the same manner. The only difference originates in the phase shift of the perturbation, due to the reversal of the poloidal field component [Schmitz 08a]. The poloidal phase shift is given as $\Phi = 180/n$ (n the toroidal mode number): for the 6/2 case this means $\Phi = 90°$ offset between NORMAL and REVERSED. This effect is visible in the vacuum topology when later comparing the poloidal island position between the NORMAL and REVERSED discharges (figure 6.28).

In the following discussion both discharges scenarios will be treated together, and will only be separated when discussing slight variations in E_r (e.g. island position, phase shift, ΔE_r). The effects caused by this phase shift are minor when compared to the overall changes of E_r during the confinement scenarios.

Plasma Particle Confinement and Particle Balance

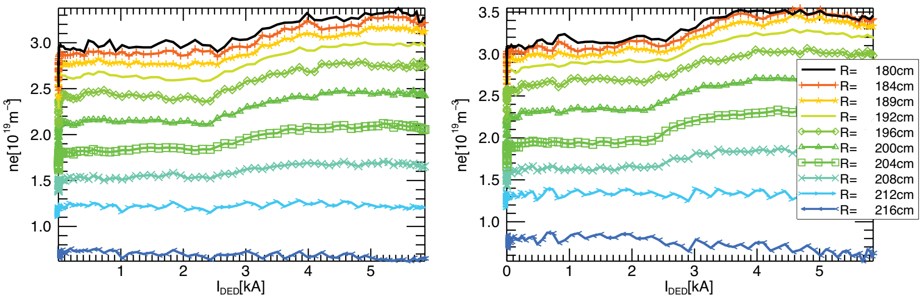

(a) Density(n_e) vs. DED Current # 106585 (b) Density(n_e) vs. DED Current #106578

Figure 6.22: Electron Density time traces for the NORMAL and REVERSED IPC discharges (#106585, #106578) with I_{DED} = 6 kA.

After we have discussed in the last section the general comparability of the NORMAL and REVERSED discharges with respect to plasma parameters and overall setup we will now start to discuss the IPC scenario in more detail. The first step is the measurements of the plasma density increase and its connection to an increase in particle confinement time τ_P.

Figure 6.22 displays the density traces shown against I_{DED} for different radial positions measured with the HCN interferometer [Donne 05] for the 6kA discharges in NORMAL and REVERSED setup respectively. It is observed that in both cases an increase in density can be observed at $I_{DED} = 2.5$ kA. The gradients steepen outside of q=5/2.

The behavior of density and density gradient is demonstrated on the basis of a set of similar discharges where Thomson scattering measurements for profiles with high spatial resolution have been performed.

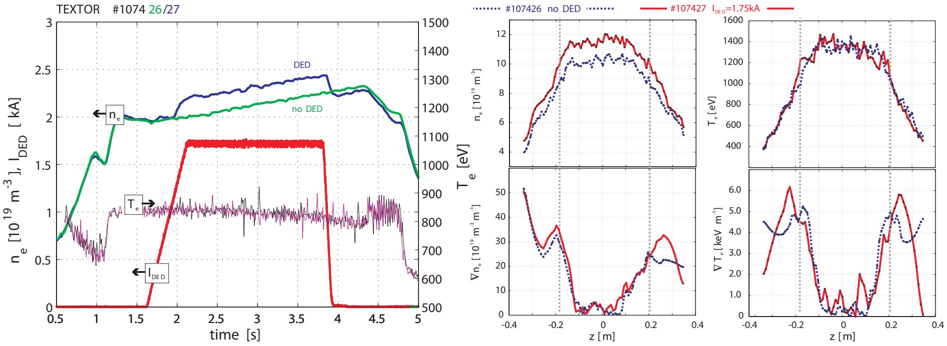

(a) (b)

Figure 6.23: (a) IPC discharge (#107427). Shown are the density traces as well as the two temperature traces and the DED current for the case with and without DED perturbation.(b) IPC discharge (#107427)Thomson profiles of electron density and temperature as well as their gradients.[Schmitz 09]

Figure 6.23(a) shows n_e, T_e, I_{DED} time traces in comparison with a non DED reference discharge, while figure 6.23(b) shows the electron density and electron temperature profiles as well as their respective gradients for the given two discharges. The density evidently rises when comparing the IPC discharges with the non IPC cases. In case of figure 6.23(b) also the increase in the density gradient outside of $z = 0.2$m is visible, $z = 0.2\,$m.

In order to determine whether this density increase an the correlated density gradient increase is an effect of improved confinement or just of changes in the gas influx, wall recycling or pumping behavior, one has to deduce the particle confinement times from a single reservoir particle balance as performed in [Schmitz 09].

The time dependent global particle balance in a single reservoir model reads:

$$\frac{dN_{tot}}{dt} = -\frac{N_{tot}}{\tau_p} + f_{rec}\,\Phi_{rec} + \,\Phi_{ext} = \Phi_{ext} - \Phi_{pump}, \qquad (6.3)$$

with total number of electrons N_{tot}, recycling flux Φ_{rec} with fueling rate f_{rec} and external flux $\Phi_{ext} = f_{NBI}\;\Phi_{NBI} + f_{gas}\Phi_{gas}$ with fueling rate f_{NBI} for the neutral beam influx and f_{gas} for the gas influx. Input parameters are the fueling rates which are subject to changes in edge parameters and as such difficult to assess. As stated in [Schmitz 09], $f_{rec} = 0.7$, $f_{NBI} = 1.0$ and $f_{gas} = 0.1$ are used.

For the calculation of τ_p one needs the recycling flux Φ_{rec} on the TEXTOR wall elements. To gain a quantitative measure of the quantity one can use a tangential view of the TEXTOR plasma given from an external camera (camera 4 with H_α Filter, described in [Schmitz 08a]). This tangential view covers about 1/3 of the plasma facing elements in TEXTOR. This view includes the coverage of the two poloidal limiters and the ALT-II as shown in figure 6.8.

The view covers the carbon target of the Dynamic Ergodic Divertor on the high field side of TEXTOR. The lines of sight allow to cover the three dimensional features of the stochastic edge layer with DED. [Schmitz 08b].

For the studied discharges none of the limiting surfaces extents into the perturbed edge region. Beginning with a small amount of external perturbation the field lines start to diverge outward and intersect with the target elements of the DED. When increasing the DED current further the discharge changes from a limited plasma towards a discharge with a stochastic boundary ([Schmitz 08b],[Jakubowski 06]).

The analysis presented here is described in [Schmitz 09]. The work is based on earlier approaches and atomic data found in [Gray 98] and [Brezinsek 05b].

The CCD camera was calibrated against an calibrated flux Φ_{gas} from a gas inlet during a density ramp. Then the measured CCD intensity signal $I_{CCD}(t)$ in $counts\ s^{-1}$ is converted into the recycling particle influx

$$\Phi_{rec} = \Phi_A + \Phi_M \tag{6.4}$$

as given by the molecular flux Φ_M and the atomic flux Φ_A. With S/XB and D/XB as the conversion factors (see [Brezinsek 05b]) a direct functional has been derived

$$I_{CCD}(\Phi_{gas})(t) = c_{cal} \times \Phi_{gas}(t). \tag{6.5}$$

In order to deduce the calibration factor and the different conversion factors a set of assumption has been made including that both the DED target and the ALT-II similarly are the main limiting elements and are treated similarly with respect e.g. to the used ionization rates (citeSchmitzPSI08. In the end a constant calibration factor is used and only adapted by the ratio of molecular to atomic fluxes ($\sim 2/3$) describing the composition of the gas calibration cloud as given in [Brezinsek 05b].

The particle influx injected by the neutral beams Φ_{beam} was calculated considering the beam voltage, the species composition [Uhlemann 99] and the beams aperture, while the particle influx Φ_{gas} from the three TEXTOR gas inlets was deduced from the pressure measurements in each of the gas feeds.

This analysis shows that particle inventory is build up by gas feed during the plasma build up ($t \lesssim 1.0\,s$) and eventually maintained by a dominant $\Phi_{rec} \simeq 10^{22}s^{-1}$ and the beam injected particles of $\Phi_{beam} \simeq 10^{20}s^{-1}$. The gas injected builds up the plasma density is pumped away to a large fraction ($\sim 98 - 99\%$) as we find $\Phi_{pump} \sim \Phi_{gas}$ during $t \lesssim 1.0\,s$. This was reflected in a low fueling efficiency coefficient $f_{gas} = 0.1$ for Φ_{gas}.

Based on this balance [Schmitz 09] one can calculate

$$\tau_p = N_{tot}/[(-dN_{tot}/dt) + f_{rec}\Phi_{rec} + f_{ext}\Phi_{ext}] \tag{6.6}$$

as particle confinement time and

$$\tau_P^* = N_{tot}/[(-dN_{tot}/dt) + \Phi_{ext}] \tag{6.7}$$

as effective particle confinement time. Both quantities together allow to characterize the particle confinement and to determine the recycling coefficient $R = 1 - (\tau_p/\tau_p^*)$.

Statements regarding the particle confinement and the recycling can only be based on the complete analysis as presented above and shown in figure 6.24.

The τ_P value deduced is related to changes of the perpendicular diffusion coefficient $D_\perp$ in the plasma source region with $\tau_P = \frac{\lambda_{io} \cdot a}{D_\perp}$, where λ_{io} is the ionization length of the fueling neutrals and a is the minor plasma radius [Stangeby 00]. Since for the IPC Scenario calibrated camera signals are available, at least for the REVERSED scenario, one can now calculate the changes in particle confinement connected to the visible density increase.

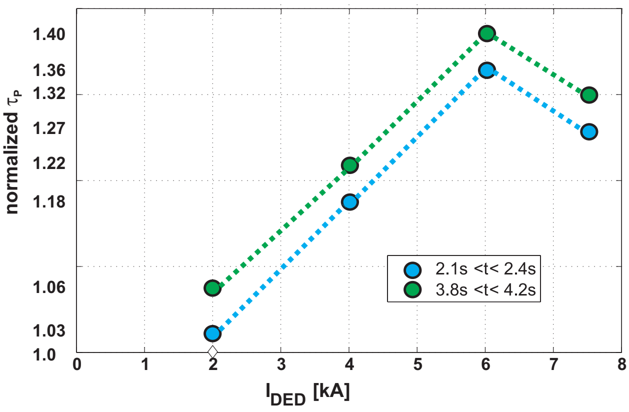

Figure 6.24: Particle Confinement time measured during IPC-REVERSED. Different discharges are used to calculate the values for each DED current separately[Schmitz 09].

Figure 6.24 shows the behavior of the particle confinement times during the different discharges, each representing a different level of ergodization caused by the different amplitude of the DED current. The confinement time is normalized with respect to the 0 kA DED discharge.

For each discharges a calculation has been performed before and after the transformer switch (t=2.8 s), in order to exclude effects caused by a slightly changed discharge behavior. The data presented was acquired during the REVERSED scenario, but shall hold true for both setups. This is suggested by the very similar discharge setup conditions.

With increasing perturbation level (DED current), the particle confinement increases up to 40% at 6 kA which evidently correlates to the increase in density shown in figure 6.22. Only a certain threshold of about 7.5kA the trend changes and the confinement diminishes again. In the following the increase in density and confinement time, as well as the subsequent transition into a lower confinement regime, will be connected to the magnetic topology and the local island structures at q=5/2. The energy confinement follows the density scaling [Finken 07a] and is not effected improved with respect to the non DED reference discharges. With the increase of the density the pressure almost linearly rises up to a certain point (n $= 4 \cdot 10^{19} m^{-3}$) indicating at least for the smaller densities a constant electron temperature during the density rise.

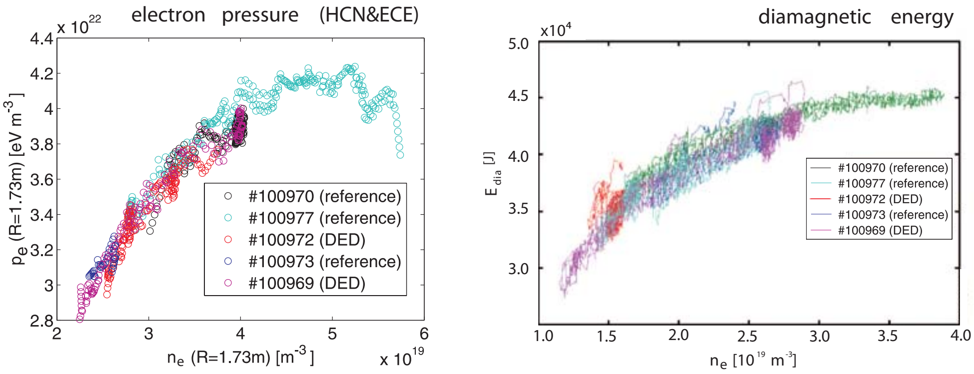

Figure 6.25: Shown are the Scaling of pressure and E_{dia} with the density.

In figure 6.25 the scaling of plasma pressure as well as the comparison with the diamagnetic energy is shown. Compared are shots with IPC and reference shots with increasing density. In addition the left figure shows indisputably that this increase in pressure is correlated with an increase in stored energy (E_{dia}), indicating an improved confinement in this case driven by an improved particle confinement. Increasing the particle confinement and hence the density and the number of particles, while keeping a constant temperature, evidently increases the amount of energy stored in the plasma.

Correlation of Magnetic Topology and Particle Confinement

In this section the variation in particle confinement will be related to changes in magnetic topology and connected to changes in the external perturbation. In this case the relation between the radial profiles and the q-profile is essential. Measured profiles are shown with the q-values on the abscissa. Since the external perturbation is interacting with the rational q-surfaces in a pitch resonant fashion one has to know with some degree of certainty, at which radial position the q surfaces are located. The q-profile can be calculated using TEXTOR input data as well as the equations presented by Wesson in [Wesson 97] and applying an analysis performed for TEXTOR discharges with externally applied heating [Lehnen 08].

The setup as we have seen in the discussion of the general parameters of the IPC discharges is always the same with respect to the magnetic field, the plasma current and for the q-profile. The

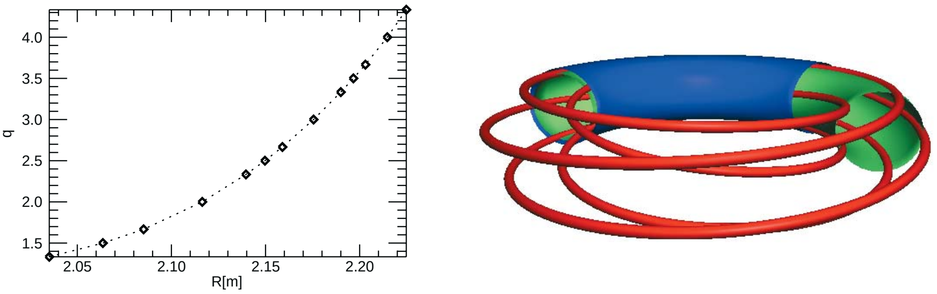

(a)

(b)

Figure 6.26: 6.26(a) q-profile for the IPC discharges. (b) Sketch of a five over two structure lying on a cylindrical q=5/2 surface at R=2.15 (green shell). The blue shell symbolizes the LCFS at R=2.21m.

differences in external heating (400kW) does not influence the poloidal beta ($\sim 10\%, \Delta B_p \sim 0.05$) nor the q-profile significantly.

Shown in figure 6.26 is the q-profile applicable for the IPC discharges discussed here, locating the $q = 5/2$ surface at $R = 2.15\,\mathrm{m}$. This is exactly the location of the density increase and the radial position of the most dominant stochastization. Since the increase of the density is located inside of the $q = 5/2$ surface we imply the hypothesis that the effects are located at this particular resonant surface and the apparent stochastization. Figure 6.26(b) can be used to get some visual sense of what a $5/2$ structure could look like in order to understand the complexity of the magnetic topology. The red tube symbolizes a a 5/2 island. It neglects effects like Shafranov shift but allows to understand the complex way the 5/2 island structure winds through the plasma. The green surface stands for the q=5/2 flux surface in which the unperturbed field line is embedded and around which the island evolves.

In the following discussion vacuum calculations of the perturbed magnetic topology will be connected to the changes in particle confinement using the visualization approach explained in section 3.2. In a first step (cf. figure 6.27) the measured DED target pattern can be used to check for changes in the ergodization of the plasma edge with increasing I_{DED}. This can then be compared to calculations of the field line penetration depth. The penetration depth is a measure for the depth the field line reaches along its path through the plasma, deduced from the LCFS.

In order to calculate this one takes a set of field line,which start at one position, follows those field lines in both direction to the target. The excursion up to their deepest penetration in terms of radius is plotted in figure 6.27(b) [Jakubowski 07](cf. 3.2).

In figure 6.27(a) the measured CII photon flux density ($\frac{photons}{m^2 s}$) is shown. Using a 2d-CCD camera with a filter at 436 nm a part of the DED target was observed during the ramp up of the DED current. Afterwards a poloidal cutout at a known toroidal position is used to follow the development of the target pattern with the change in perturbation(I_{DED}). With no external perturbation applied no pattern is visible. The pattern starts to emerge when a small level of perturbation is applied it evolves and move apart as the current increases.

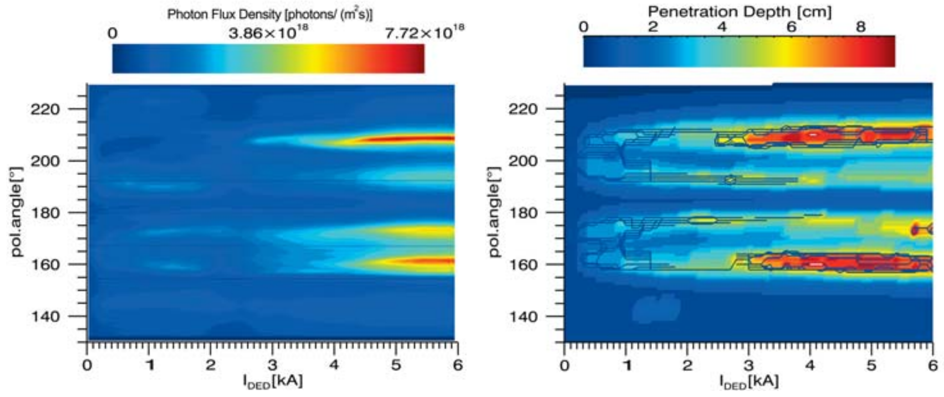

(a) Target Pattern, CII emission (b) Target Pattern, Penetration Depth (calculated)

Figure 6.27: DED target pattern: CII emission from discharge # 106585 and the calculated penetration depth from vacuum calculation.

At $I_{DED} = 2.5$ kA the pattern changes its shape and increases drastically in intensity. A structure arises and keeps steady with increasing perturbation. A similar approach is used to study the behavior of the open field lines by varying the edge safety-factor q_a, the ergodization and the DED target pattern [Jakubowski 07].

The calculation of this target pattern, or in this case the magnetic field lines connected to such a target pattern, can be compared with the measured data. Even though the calculation reveals much more detail than available from the measurements, the behavior is evidently the same. At an amplitude of 2.5 kA DED current the pattern changes, a much more pronounced structure arises with a penetration depth close to 6-7 cm. Taking the radius of the LCFS on the HFS and using the penetration depth one can deduce that the open field lines, hitting the target, are coming from the $q = 5/2$ surface at $R = 2.15$m.

If one compares the measured data and the modeled target pattern, the correlation between the pattern and the transition threshold of $I_{DED} = 2.5$ kA is evident. This change in topology is thus correlated with the stepwise increase in electron density and the steepening of the density gradient at $R = 2.15$ m ($q = 5/2$). As soon as field lines connect to the DED target the density increases, the field lines are called open field lines or tangles.

In order to get a deeper understanding of the magnetic topology applicable to this scenario figure 6.28 shows a set of several plots, representing the footprint of the magnetic topology for different amplitudes of I_{DED}.

As expected from the setup of the discharge, the most prominent structure visible are the 6/2 and $5/2$ island chains. While the $6/2$ island chain at $q = 3$ is influenced already by very small perturbation, the $5/2$ island chains starts to get ergodized at the x-points, just when reaching $I_{DED} = 2.5$ kA. This behavior correlates with the observation of the target pattern, where at first there is only a small structure originating from the $q = 3$ surface. With the onset of the ergodization of the $q = 5/2$ island chain the structure changes and a clear connection

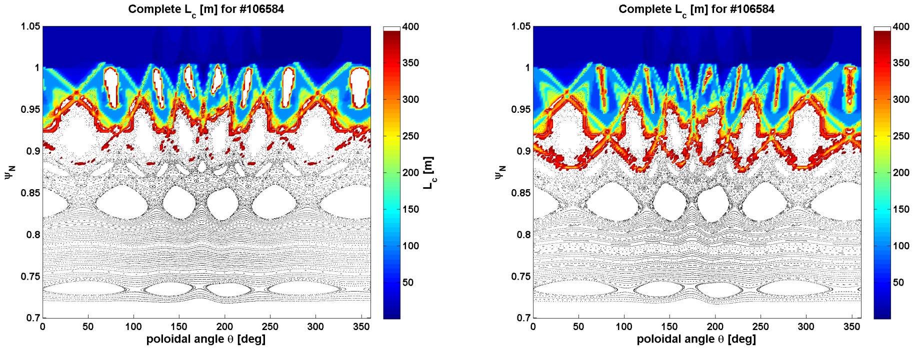

(a) IPC Scenario @ I_{DED}=2.0kA (b) IPC Scenario @ I_{DED}=2.5kA

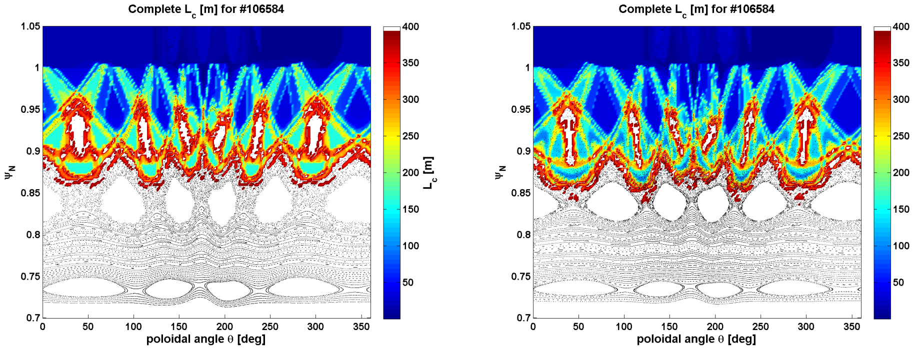

(c) IPC Scenario @ I_{DED}=4.0kA (d) IPC Scenario @ I_{DED}=5.0kA

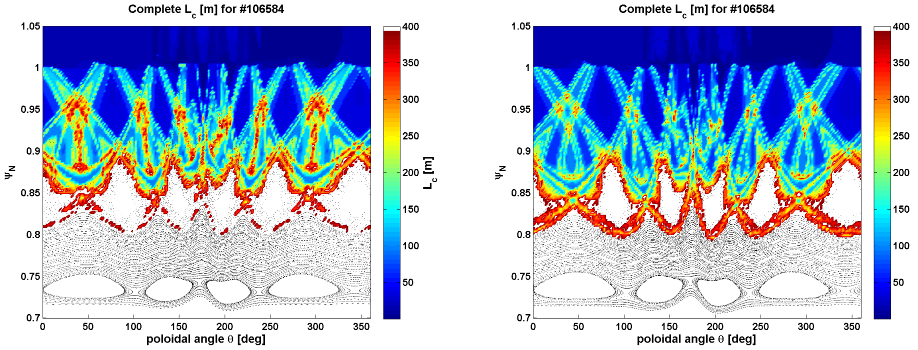

(e) IPC Scenario @ I_{DED}=6.0kA (f) IPC Scenario @ I_{DED}=7.5kA

Figure 6.28: Magnetic topology calculations for the IPC scenario, based on Gourdon calculations. The connection length (color coded laminarplots) as well as the field lines (Poincare plot) are shown for 3 different amplitudes of the external magnetic perturbation (I_{DED}). These plots have been made for the NORMAL setup.

between target and island x-points is established. This provides the same picture as established in [Finken 07a]. The x-points are ergodized without ergodizing the whole island chain.

Figure 6.28(a) shows the 2 kA case just before the onset of the IPC. No ergodization near the q=5/2 surface can be seen in the vacuum topology while the 2.5 kA case shown in figure 6.28(b) shows the onset of ergodization at the island x-point. This correlates with the onset of the target pattern in figure 6.27. With increasing perturbation 4, 5, 6 kA the ergodization of the 5/2 island chains increases further, until at 7.5 kA the ergodization encloses the whole island, de facto breaching the island chain. With increasing DED amplitude the ergodization zone moves deeper into the plasma, while the laminar SOL like behavior, with short connections length, increases as well. The width relative to each other changes while the stochastic zone becomes wider.

The made observations lead to the conclusion that the confinement strongly depends on the level of ergodization of the last island chain and the number of connected tangles to the DED target. Since in section 6.3.1(p.89) a method was described to perform a detailed particle balance for the IPC discharges (cf. figure 6.24) the direct connection between the DED amplitude and the particle confinement was established and can now be quantitatively compared to the stochastic edge layer composition.

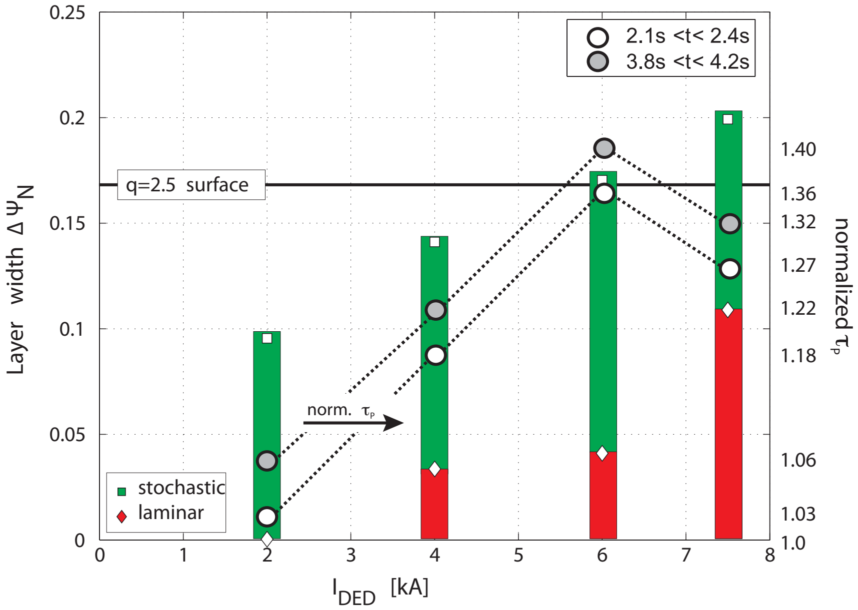

Figure 6.29: Increase of particle confinement time τ_P with I_{DED} and corresponding evolution of laminar and stochastic layer width $\Delta\Psi_N$[Schmitz 09]

As has been described in section 3.2 figure 6.29 shows the results of an analysis regarding the 3D perturbed edge layer in comparison to τ_P for discharges with density build up on different levels of I_{DED}. The left ordinate shows the width of laminar and ergodic layer. The width of both layers are depicted as bars and the length of the complete bar shows the complete extension of the perturbed edge. Red bars with markers as boundary depict the laminar layer width while green bars with markers as boundary depict the ergodic layer width. The width is given in units of normalized flux Ψ_N ($\Delta\Psi_{N laminar} = 1 - \Psi_{N laminar}, \Delta\Psi_{N ergodic} = 1 - \Psi_{N ergodic}$). Ψ_N describes the radial coordinate in terms of the normalized magnetic flux enclosed at the given position.

This approach assumes the simplification as explained in section 3.2.2 regarding the ergodic ($L_c < L_K$) and laminar zones ($L_c > L_K$).

For the low DED current discharge (2 kA) the influence on the τ_P is barely visible. The extension of the perturbed layer is small and the q=5/2 surface, as also visible from figure 6.28(a), is not affected in this case. Increasing the DED current up to 4 kA leads to the extension of the perturbed layer towards the q=5/2 surface and in addition a small laminar zone is established.

The last but one step, increasing the current up to 6 kA is again correlated to an increase in τ_P with an increase in the ergodic zone width and a quite steady laminar zone. This marks the most increase in τ_P seen in this study.

At 7.5 kA the perturbed layer completely extends over the q=5/2 surface and a strong increase in the width of the laminar zone is shown. This level of perturbation marks the transition from improved particle confinement towards the so-called particle pump out scenario (PO) as discussed in 3.2 and 6.3.2. The two mechanism contributing to the loss of confinement are the rather diffusive radial transport in the ergodic region and the scrape of layer like parallel losses in the laminar zone [Schmitz 09].

In summary the IPC is characterized in terms of transport and magnetic field changes by the increase in N$_{tot}$ and τ_P.

The changes in topology and in transport are directly correlated to the amount of stochastization reaching the $q = 5/2$ surface and connecting field lines to the target (field lines are shorter than mean free path for electrons). It is surmisable and plausible that along these field lines the plasma energy is carried outward and a short circuit is formed between island chain (x-points) and the wall. The improvement is tentatively attributed to a modification of the electric potential in the plasma carried by the open field lines. This leads to the need to study the radial electric field and its changes.

From the agreement of measured and modeled target pattern 6.27, one can conclude that the open ergodic structures develops a short field line connection to the target which transfers the plasma flux. These short connection length field lines should also transport efficiently the electric potential from the walls deep into the plasma, in this case, to the perturbed island chains (x-points). This statement is in agreement with a previous observation on the TEXT tokamak[Mccool 90].

Connecting distinct changes in the E_r to the IPC scenario and the different levels of ergodization can lead to a deeper understanding of the underlying plasma behavior. The observed effects and connections to the IPC will be described in the following section.

The Radial Electric Field and its Changes

Improved confinement scenarios (cf. e.g. H-Mode), especially when connected to a transport barrier are connected to changes in the E_r and the $\vec{E} \times \vec{B}$ shearing rate [Moyer 95, Burrell 97, Ida 98, Burrell 05]. What Moyer [Moyer 95] calls the paradigm of shear suppression of turbulence is one of the most prominent effects during the transition into high confinement modes or the onset of transport barriers.

In the following discussion the features of the radial electric field under circumstances of IPC will be discussed in detail for both scenarios with negative helicity. As discussed in section 6.2.1 the profiles will be given in absolute values and in terms of Δ-values, relative to the measurements for the discharge without DED.

As discussed in section 6.1.1 the radial electric field contributions from the poloidal and toroidal rotations are relevant, the diamagnetic contribution is small and can be neglected.

For the discussion of the case of IPC during negative helicity discharges the set under NORMAL field and current configuration is chosen. A comparison between NORMAL and REVERSED scenario is considered later in section 6.3.1 (pp. 103)

For reasons of simplicity and clarity the plots are shown without explicitly showing the error bars. As has been described (section 5.3) the measurement uncertainties are in the order of ± 0.7 km/s for the poloidal rotation and ± 4 km/s for the toroidal rotation, leading to an uncertainty on the radial electric field of ~ 1 kV/m taking into account the local magnetic fields. In addition typical systematic uncertainties for the poloidal, the toroidal field and the local safety factor q have to be considered.

Accounting for a typical uncertainty of 5% for the toroidal field, 15% for the poloidal field and 10 % for the safety factor [Busch 06, Testa 06] one reaches total error bars of ~ 5 kV/m for E_r, ~ 3 kV/m for the toroidal contribution and ~ 1.5 kV/m for the poloidal contribution.

In order to understand the changes in the radial electric field and distinguish effects connected to the IPC from effects originating in the return current concept discussed in sections 3.3 & 6.2.1 the poloidal $E_r(pol)$ as well as the toroidal $E_r(tor)$ contributions to the radial electric field are discussed before turning to the description of total radial electric field E_r.

Figure 6.31 & 6.30 give a detailed insight into the trends for the two E_r contributions as well as the behavior with respect to the 0 kA reference discharge.

Toroidal Contribution $E_r(tor)$, (figure 6.30) The toroidal contribution has very stiff profiles due to the radial viscosity. With the increases of the perturbation amplitude, the DED current, the radial electric field increases consistently with the approach discussed in section 3.3 & 6.2.1. Even though the absolute shape has a tendency towards negative values in the plasma center caused by the counter current NBI torque the relative approach clearly shows that the whole profile is affected quite homogeneously. The $\vec{j} \times \vec{B}$ force is causing the general spin up in the ergodic zone, and the radial viscosity causing the whole profile to follow this momentum input.

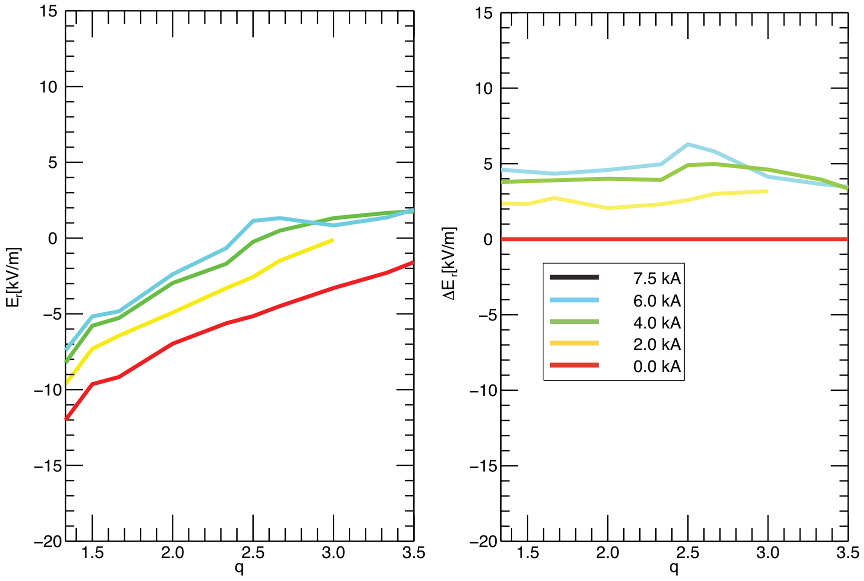

(a) $E_r(tor)$ contribution (b) $\Delta E_r(tor)$ contribution

Figure 6.30: Profiles of the toroidal contribution to the radial electric field contributions in case of the NORMAL setup. Absolute values and relative values (with respect to the unperturbed case) are shown

The evolution of the DED induced rotation shows the effect also seen in theory. A tendency of saturation is observed for the later steps in DED amplitude. Less increase of $E_r(tor)$ per kA is manifested. The largest increase is 2-3 kV/m for the first 2 kA DED amplitude.

The homogeneity is only broken at the highest perturbation amplitudes locally at $q = 5/2$. A structure evolves in the radial profile exactly at the location of the $5/2$ island chain. The IPC is fully developed at this point, which again demonstrated the strong correlation of local effects at $q = 5/2$ and the localization of the IPC.

Poloidal Contribution $E_r(pol)$, (figure 6.31) The poloidal contribution is responsible for most of the localized structures in the total E_r profile, dominating the shape, while the toroidal rotation adds an overall offset as seen in figure 6.30.

The poloidal rotation is subject to strong neoclassical dampening and thus is affected by localized changes. This means that e.g. the $\vec{j} \times \vec{B}$ force originating in the ergodic zone between q=5/2 and q=3 is the driving force changing the poloidal contribution towards more positive E_r values.

The profile of the poloidal contribution shown in figure 6.31 as well as the relative profiles are clearly much more inhomogeneous when comparing to the toroidal contribution. The reference discharge is following the tendency of the central poloidal rotation into the electron diamagnetic direction, meaning a negative electric field and negative poloidal rotation (following the SOL flow) in the plasma edge, results in a positive contributions to the E_r.

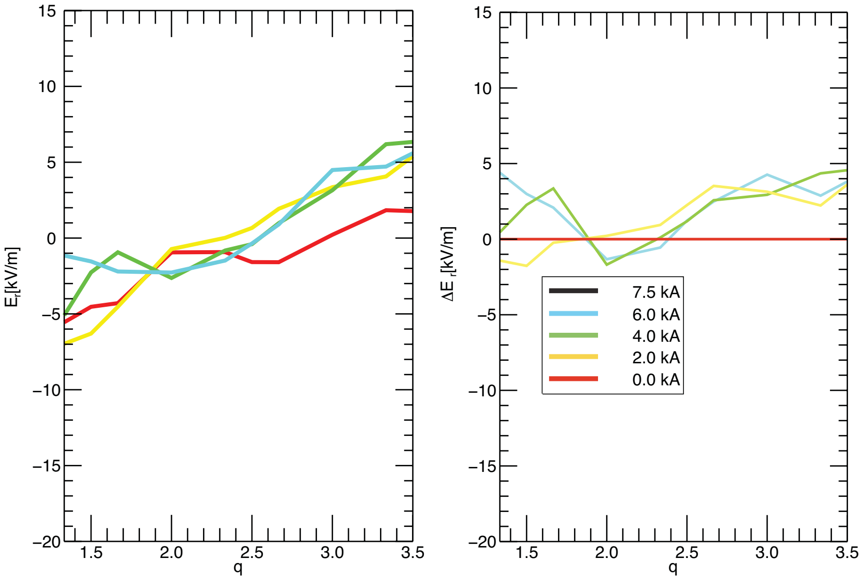

(a) $E_r(pol)$ (b) $\Delta E_r(pol)$

Figure 6.31: Profiles of the poloidal contribution to the radial electric field contributions in case of the NORMAL setup. Absolute values and relative values (with respect to the unperturbed case) are shown

When switching on the perturbation the outer part instantaneously reacts on even the smallest perturbation amplitude increasing the $E_r(pol)$ already to almost the maximum excursion. The $q = 2$ surface does not react at all and the innermost part of the profile only react when increasing the DED amplitude well beyond the IPC threshold (2.5 kA). The deepest penetration for the perturbation is achieved at very high amplitudes, the $E_r(pol)$ is then increasing within $q < 2$.

The gradient of the radial electric field at $q = 5/2$ is directly connected to the steepening of the poloidal contribution, when comparing the different discharges for different DED amplitudes.

Total E_r After the discussion of the seperate contributions figure 6.32 displays the total E_r. An overview on all discharges used during the IPC in NORMAL configuration is given. In figure ((a) the absolute profiles are shown including the 0kA case, while figure (b) represents the relative profiles with respect to the 0 kA reference discharge.

The profile shape with the negative values in the plasma center and the positive values close to the plasma edge is the combination of both the toroidal and poloidal contribution in respective directions. The toroidal contribution and the underlying NBI torque is dominating the negative radial electric field in the plasma center while the positive values from the poloidal contributions are responsible for the overall positive radial electric field at $q \geq 5/2$.

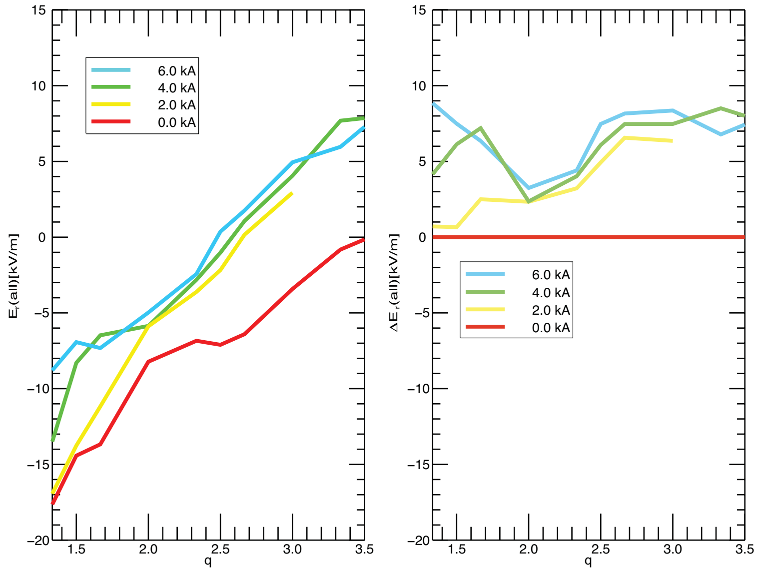

(a) E_r - NORMAL

(b) ΔE_r - NORMAL

Figure 6.32: Profiles of the radial electric field and relative changes with respect to the $I_{DED} = 0$ kA reference discharge). Shown for the NORMAL configuration.

As can be seen already from the separate contributions the radial electric field increases with increasing DED amplitude. The maximum change with respect to the reference discharge is reached with 9 kV/m. The E_r profile follows the strong reaction of the poloidal contribution outside of $q = 5/2$ and shows a reaction of the E_r profiles inside of the $q = 2$ surface only for high amplitudes. The toroidal contribution gives an overall offset.

Outside of $q = 5/2$ the tendency is visible that would be expected from the return current model discussed in 3.3 and shown on local rotations measurements in 6.2.2 as well during the discussion of the toroidal and poloidal contribution. At the level of 2 kA the total E_r is already increased almost to its maximum since the zone around $q = 3$ is completely ergodized (cf. figure 6.28(a)), increasing the current further leads to the improved particle confinement and local changes of the E_r at $q = 5/2$, the steepening of the gradient.

It is only with additional amplitude of the perturbation that effects are manifesting inside of the $q = 2$ surface, probably due to deeper penetration of the perturbation. Those effects may be connected to topology like the formation of a $3/2$ island with higher perturbation which are then manifested in the poloidal rotation changing toward the ion diamagnetic drift direction. The calculations in the vacuum approximation gives a clear island chain at $q = 3/2$. This is not included in the presentation in figure 6.28.

The radial electric field steepens at $q = 5/2$ as an effect of the local changes in the toroidal and especially the poloidal contribution. The more DED is applied the steeper the radial electric field becomes. This effect becomes particularly visible when taking the relative changes in to account. The gradient is further discussed in terms of the shearing rate $\Omega_{\vec{E}\times\vec{B}}$ after establishing the comparability of negative helicity scenarios (NORMAL and REVERSED).

IPC Scenarios with Negative Helicity

In order to underline the universality of the IPC scenario in the following the comparison between the IPC in NORMAL and REVERSED configurations shall be given.

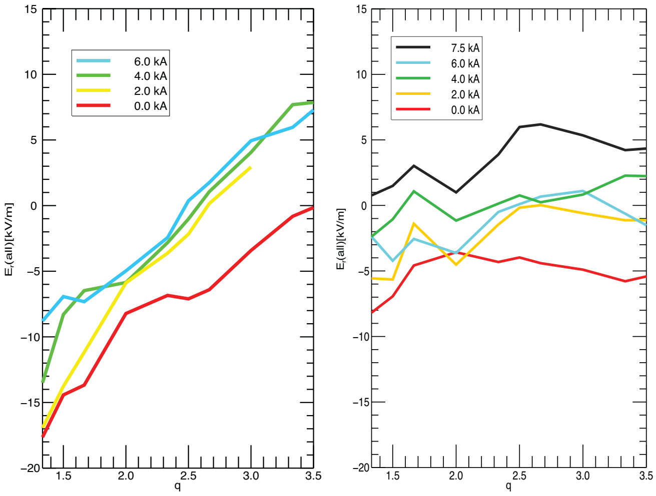

(a) E_r - NORMAL (b) E_r - REVERSED

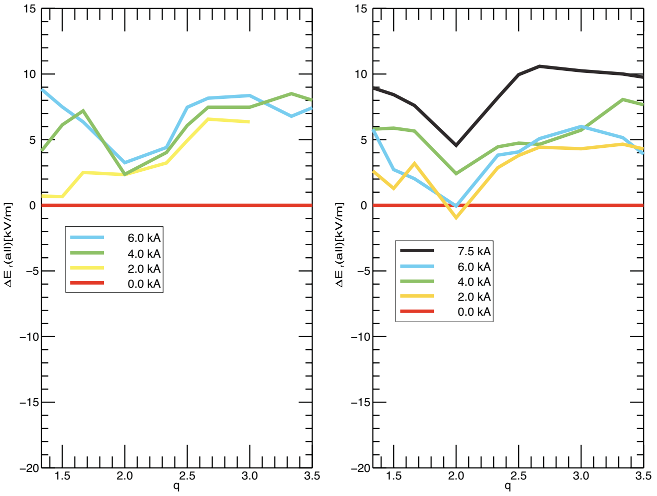

(c) ΔE_r - NORMAL (d) ΔE_r - REVERSED

Figure 6.33: Profiles of the radial electric field, shown for both setups with negative helicity.

As discussed in section 6.1.2 the reversal of magnetic field and plasma current while preserving the helicity is connected to distinct effects on the rotation. The poloidal rotation does not change sign as has been shown in section 6.1.2 (figure 6.12, equation 2.29 & 2.30), while the toroidal rotation, driven by external momentum input (NBI torque), does.

This causes distinct differences in the absolute values and profile shape of the E_r when comparing the two configurations as can be seen in figure 6.33

The obvious differences between the two sets of profiles can be seen in Figure 6.33. While the profiles for the E_r in the NORMAL setup are visibly oriented from negative values in the plasma core ($q \leq 2$), corresponding to strong counter rotation due to the NBI, the profiles representing the REVERSED setup are seen to be flat. This feature can be explained due to the difference in behavior of the toroidal and poloidal contribution, when switching from NORMAL to REVERSED setup. The poloidal contribution is not changed with I_p/B_ϕ reversal and thus now complements the toroidal contribution with opposite sign, flattening out the total E_r.

The structure of the profiles when comparing both setups in figure 6.33 is not comparable when taking the absolute values into account even though the steepening of the gradients at q=5/2 is seen as well. Only when subtracting the respective contributions for the 0kA reference discharges the profiles become similar.

The ΔE_r plots for the NORMAL and REVERSED configuration show the same distinctive dent at $q = 2$, the rise of the E_r at low perturbation for $q \geq 5/2$ as well as the late increase of E_r in the plasma center.

Absolute Values The absolute values as been seen from the overview in figure 6.33 are quite different when comparing NORMAL and REVERSED configuration. A deeper look at this behavior is available from figure 6.34.

The toroidal contribution for both configurations are very similar only differing slightly by 2 kV/m or about 10-20 km/s due to the difference in applied external heating and momentum input. With increasing DED amplitude the radial electric field contribution becomes more positive in both configurations, the agreement remains, as for the unperturbed case, over the whole profile.

The poloidal contribution however differs completely when comparing the red and blue curves. The Poloidal Rotation profile remains mostly unchanged when keeping the helicity constant, hence reversing the toroidal magnetic field causes the contribution to the radial electric field to change sign. The two curves are not overlapping at all. With increasing DED amplitude the structure of the profiles change differently since the influence due to the $\vec{j} \times \vec{B}$ points always towards the ion diamagnetic drift direction, towards more positive E_r.

At last the contributions can be used to calculate the total radial electric field shown in the bottom row figure 6.34. The total radial electric field is flat for the REVERSED configuration and steeply inclined to the plasma center for the NORMAL configuration. The curves do not agree, with one exception, the gradients around the $q = 5/2$ surface are very similar, hence giving one indication for the IPC occurring in both configurations.

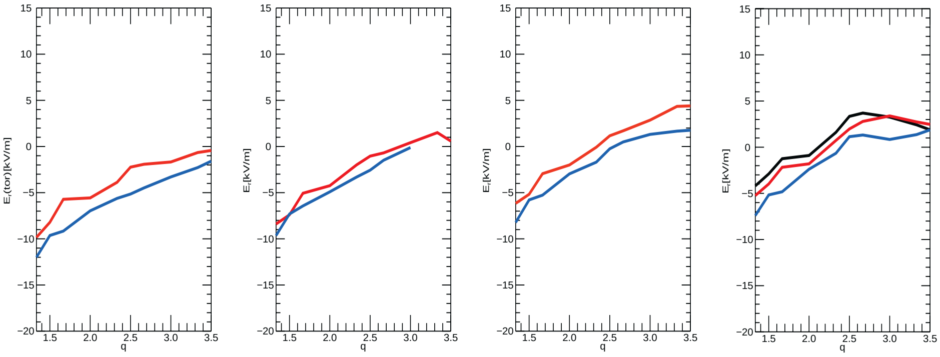

(a) 0 kA - $E_r(tor)$ (b) 2 kA - $E_r(tor)$ (c) 4 kA - $E_r(tor)$ (d) 6 & 7.5 kA - $E_r(tor)$

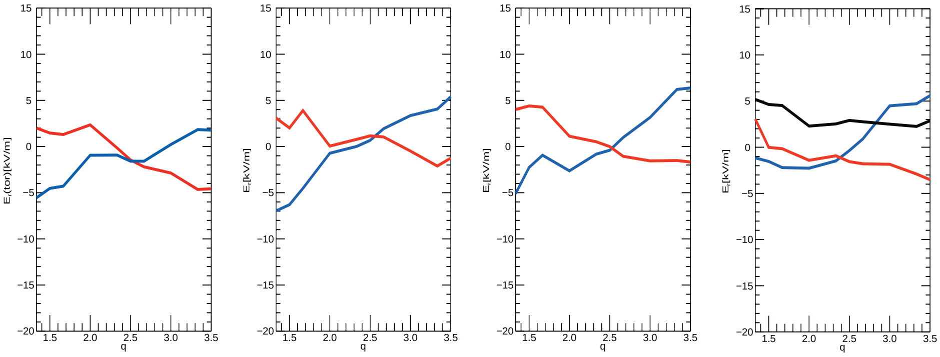

(e) 0 kA - $E_r(pol)$ (f) 2 kA - $E_r(pol)$ (g) 4 kA - $E_r(pol)$ (h) 6 & 7.5 kA - $E_r(pol)$

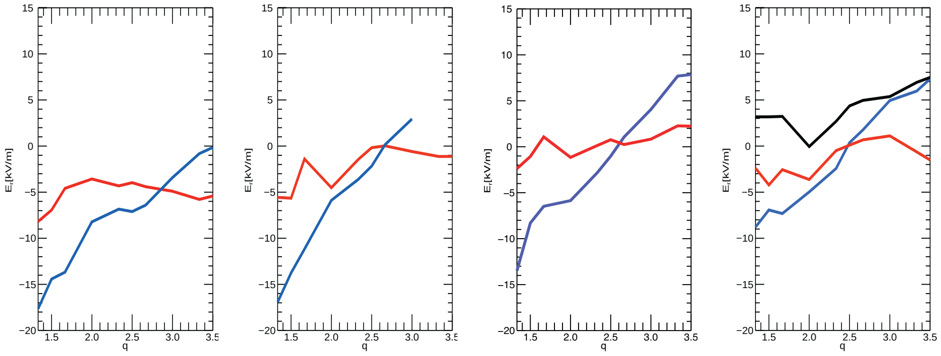

(i) 0 kA - E_r (j) 2 kA - E_r (k) 4 kA - E_r (l) 6 & 7.5 kA - E_r

Figure 6.34: Profiles presented are comparing the absolute values of the contribution to the E_r as well as its total value with respect to changes occuring when studying IPC in NORMAL and REVERSED configuration. Black is the 7.5 kA discharge in the REVERSED setup.

Relative Values Already the absolute values show similarities at the $q = 5/2$ surface for both configurations, in order to study those agreements in more detail and resolve possible difference causes by the changes in magnetic perturbation one can plot the relative changes with respect to the unperturbed case. For each discharge and DED amplitude the comparison between the two configurations is made.

This method will remove the influence of the different behavior originating from the rotation and allow the resolution of the changes caused by the increase of the DED amplitude in both scenarios (cf 6.2.1). In figure 6.35 the relative profiles for the toroidal contribution, the poloidal contribution as well as the total radial electric field are shown.

All three comparisons show that the profiles after removing the background behavior are quite comparable for the REVERSED and NORMAL configuration, the effect of the DED on the radial electric field is comparable in all discharges with negative helicity.

Minor changes however are visible, when comparing the profiles at rational surfaces. The Toroidal rotation profiles are comparable in amplitude and increase with DED, however at q=3/2 and q=5/2 the profiles deviate slightly upwards for the NORMAL and downwards for the REVERSED configuration. Regarding the poloidal contribution a similar effect is observed at rational surfaces q=3/2, q=5/2 and q=3 which is even increasing with rising DED amplitude in contrast to the constant effect in the toroidal rotation.

The overall effects of the IPC such as density transition and confinement improvement increase of E_r and steepening of the E_r at q=5/2 do not vary between the NORMAL and REVERSED configurations. This is also valid for the overall increase of the E_r. It can, however, be seen that the magnetic topology does vary (figure 6.36).

While one of the island x-points for the NORMAL case lies just at $0°$ it is moved by $90°$ when reversing B_ϕ and I_P. This has no indication for the analysis presented in figure 6.29 or on the general effects regarding the E_r but it can have indications for the local measurements of the E_r and the observation of the slight variations. The RuDI diagnostic beam is located in the equatorial plane, meaning poloidal angle $0°$. At the $q = 5/2$ island chain the $360°$ are divided onto 5 islands ($\sim 360/5$) meaning that, with a phase shift of $90°$ and approximately 36 degree between x-point and o-point of the island, the observation volume is shifted from the o-point to the x-point of the island.

This behavior might explain the variations between the NORMAL and REVERSED scenario. While the dominant radial viscosity is probably smoothing this effect in case of the toroidal rotation the poloidal rotation can be affected more locally and hence is showing an evolution of the deviation with increasing DED. Especially at the q=3/2 the vacuum topology is typically thought to be failing. The observed behavior is showing indications for the vacuum topology to be true even this deep inside plasma.

The overall influence of the DED remains the same, with increasing DED the profiles become more positive and the E_r steepens. Since those features are the one most prominently connected to the IPC scenario a more detailed look at the $q = 5/2$ surface and its connection to the radial electric field shear or better the $\vec{E} \times \vec{B}$ shearing rate $\Omega_{\vec{E}\times\vec{B}}$ is given in the following section.

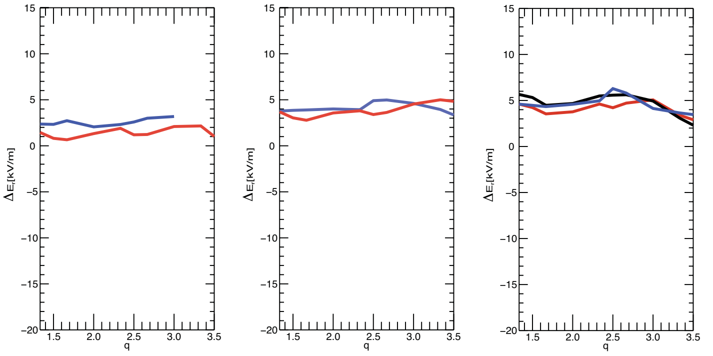

(a) 2 kA - $\Delta E_r(tor)$ (b) 4 kA - $\Delta E_r(tor)$ (c) 6 & 7.5kA - $\Delta E_r(tor)$

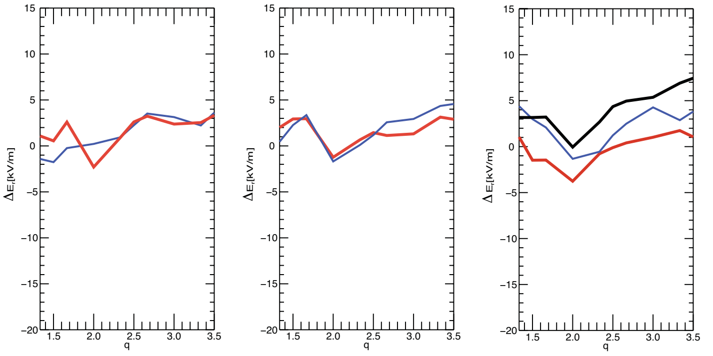

(d) 2 kA - $\Delta E_r(pol)$ (e) 4 kA - $\Delta E_r(pol)$ (f) 6 & 7.5kA - $\Delta E_r(pol)$

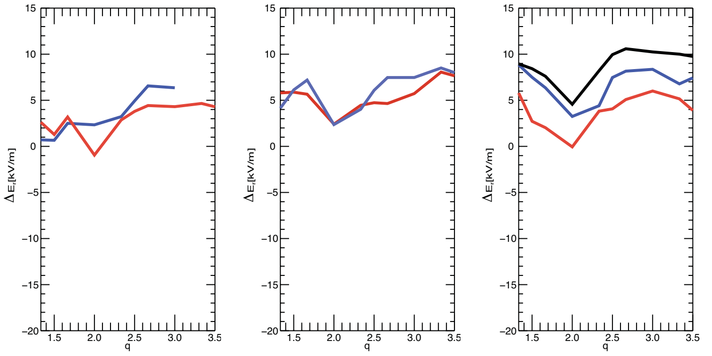

(g) 2 kA - ΔE_r (h) 4 kA - ΔE_r (i) 6 & 7.5kA - ΔE_r

Figure 6.35: Profiles are showing the different contributions to the E_r as well as the E_r itself with respect to the 0kA reference discharge(comparing NORMAL, REVERSED configuration). Black is the 7.5 kA discharge in the REVERSED setup.

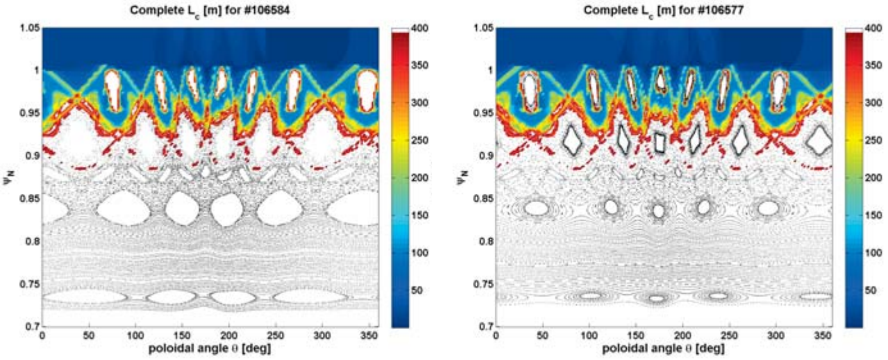

(a) IPC Scenario @ I_{DED}=2.0kA, NORMAL (b) IPC Scenario @ I_{DED}=2.0kA,REVERSED

Figure 6.36: Magnetic topology represented as overlay of laminar and Poincare plot calculations for the IPC scenario, based on Gourdon calculations. Comparing the NORMAL(a) and the REVERSED(b) setup.

$\vec{E} \times \vec{B}$ shearing Rate $\Omega_{\vec{E}\times\vec{B}}$

The quantity discussed in the following is directly connected to the electric field gradient as discussed above and called the $\vec{E} \times \vec{B}$ shearing rate (cf. equation 2.37). Similar to the approach chosen for the presentation of the radial electric field data, the shearing rate is presented in terms of the actual values as well as the Δ-values. In order to allow a clear presentation of the data the error bars again are suppressed. The error bars are in the order of $1.75 \cdot 10^5 s^{-1}$ for Ω including systematic uncertainties, the error bars for the delta values follow according to gaussian uncertainty propagation.

Typically the absolute value of $\Omega_{\vec{E}\times\vec{B}}$ is used as the parameter judging upon turbulent suppression and hence transport suppression during improved confinement scenarios like the H-Mode [Wagner 82]. $\Omega_{\vec{E}\times\vec{B}}$ exceeding the turbulence growth rate is taking as the criterion. Taking the H-Mode as an example one applies external heating up to a threshold to initiate the improvement, or applies external biasing as been done at for example at TEXTOR [Weynants 92] to reach the state of improved confinement. This is typically connected with an edge transport barrier and strong gradients of edge plasma pressure, hence shearing

It is assumed that in case of the H-Mode the edge pressure gradient becomes the dominant driving term of the E_r and hence local shearing of the E_r occurs. This shearing can when being large enough tear up turbulence [Biglari 90, Moyer 95], leading to decreased radial transport.

When comparing with H-mode or biasing experiments [Biglari 90, Wagner 82, Moyer 95, Weynants 92] the data discussed here provides another insight in the universality [Burrell 97] of the shearing rate Ω as the parameter defining the improvement for confinement in tokamaks.

In Figure 6.37 the shearing rate and the relative shearing rate for the NORMAL and REVERSED scenario are shown. In both cases the shearing rate increases locally inside or at q=5/2 again making the connection to the previously discussed effects at this rational surface (density increase and gradients, magnetic topology and E_r gradients and profile similarities).

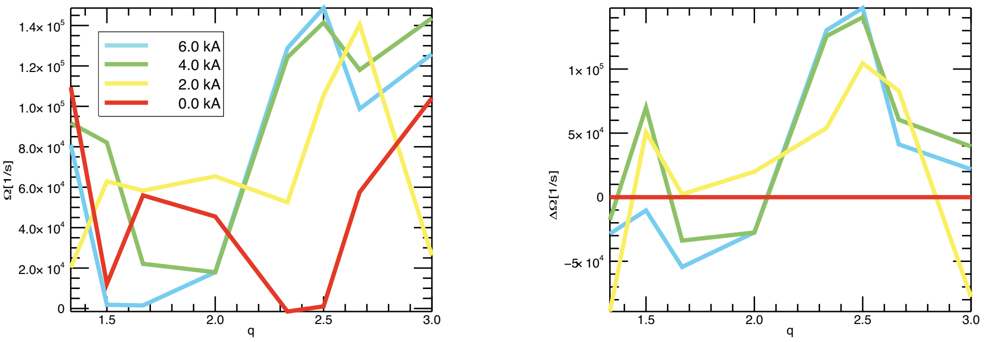

(a) $\Omega_{\vec{E}\times\vec{B}}$ and $\Delta\Omega_{\vec{E}\times\vec{B}}$ calculated from the Profiles acquired during NORMAL setup

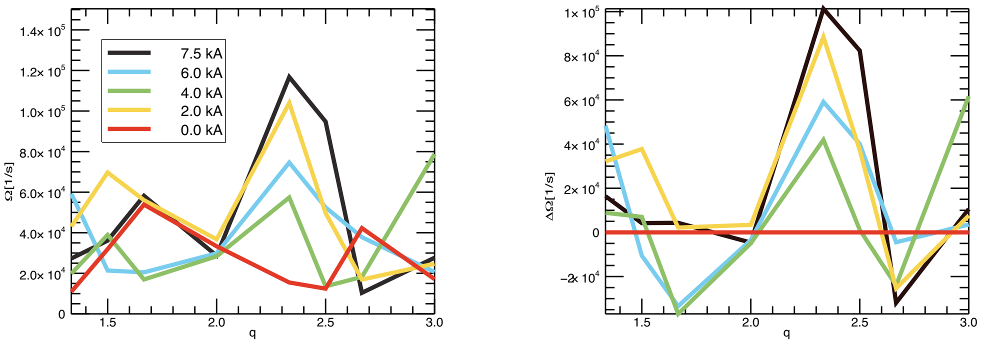

(b) $\Omega_{\vec{E}\times\vec{B}}$ and $\Delta\Omega_{\vec{E}\times\vec{B}}$ calculated from the Profiles acquired during REVERSED setup

Figure 6.37: $\vec{E} \times \vec{B}$ shearing rate Ω. Figure 6.37(a) and 6.37(b) shows all discharges available for the IPC scenario (cf. section 6.3.1). Black gives the 7.5 kA discharge in REVERSED configuration.

The shearing rate changes very locally up to a absolute value of $1.4 \cdot 10^5 s^{-1}$ and $1.2 \cdot 10^5 s^{-1}$ for the NORMAL and REVERSED case respectively. The shearing rate increases drastically and only at the rational surface. When observing the relative changes of Ω it even becomes more clear that the effect is localized to this particular resonance and the shearing rate increases with the amplitude of the DED.

Comparing the curves in figure 6.37 for each step the trend is clear for the NORMAL and REVERSED, the data correlates with the localization and the tendency of the increase of the particle confinement time as seen in figure 6.29.

The density increases, the τ_P rises, the magnetic topology changes and the local shear is increased in both setups. This leads to the conclusion that localized at this particular resonance the improved particle confinement is connected to a resonant change of magnetic topology and a connected change in E_r as observed in other improved confinement scenarios.

Since this behavior in the case of the IPC is reached with means quite different from those seen in e.g H-Mode experiments it might permit the conclusion that indeed the shear of the E_r is not only one of the features connected to improved confinement modes, but the feature connecting all the different approaches to reach improved confinement scenarios in tokamak machines.

However the question of causality remains, which could only be solved by a far higher time resolution that is not available with the current setup.

6.3.2 Pump Out Scenario with DED

In order to contrast the findings of the IPC one can ask the opposite question: Is there a scenario with decreased particle confinement available during DED operation? And what separates such a scenario from the IPC?

This question in part was answered already taking figure 6.29 into consideration where at a certain value of the perturbation (7.5kA) a decrease in particle confinement correlated with a large increase in laminar zone width was seen. This means that when reaching a scenario where the laminar zone becomes large at very low perturbation current a so-called Pump Out (PO) scenario with decreased particle confinement can be established.

The data considered was obtained in the REVERSED configuration, since only here a profile coverage over the whole radial range was achieved.

With respect to the IPC scenario the general setup of the PO discharges is only marginally changed. The main change is in plasma position and edge safety factor q_a in such a way that the resonant surface $q = 5/2$ is more closely located to the perturbation coils (DED).

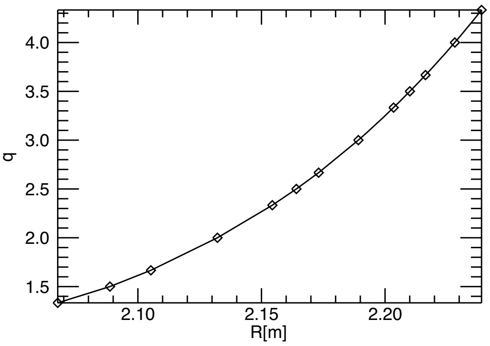

Figure 6.38: q-profile for the PO discharges

I_{DED}	NORMAL	REVERSED
0.0 kA	106541	106544
2.5 kA	106539	106547
5.0 kA	106538	106546
7.5 kA	106540	106545

Table 6.2: PO discharges with DED current and shot number

The discharge parameters are : R_0 =1.755 m, a =0.458m, q_a =3.4 , R_{sep} =2.213 m with B_ϕ =2.1 T and I_P =410kA and $P_{NBI(counter)}$ =1.6 / 2 MW

The edge q was reduced by about 0.4 in comparison to the IPC case moving e.g. the $q = 5/2$ surface closer to the DED coils by 1-2 cm. This can be seen when comparing the q-profile for the PO discharges shown in figure 6.38 with the one given for the IPC discharges in figure 6.26. The resonant rational flux surfaces are shifted more towards larger minor radii.

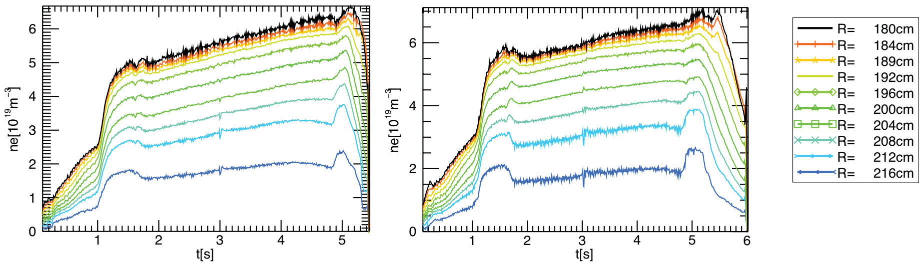

(a) Density(n_e) vs. time # 106540

(b) Density(n_e) vs. time # 106545

Figure 6.39: Density time traces for the NORMAL and REVERSED PO discharges (#106540, #106545) with I_{DED} = 7.5 kA.

This slight change of the q-profile caused by the changes in plasma current has drastic consequences for the particle confinement. Figure 6.39 displays the density traces for the 7.5 kA discharge in PO scenario. A drop in density can be observed for the phase of DED operation, between 1.8 s and 4.8 s. The line average density drops, and the density traces outside of 2.15 m are effected by a drop of at most 30% of density decrease.

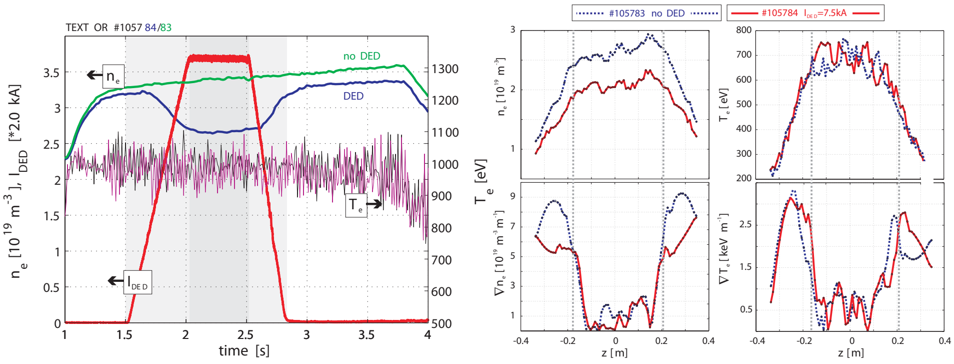

(a) Shot comparison

(b) Thomson profiles for n_e and T_e

Figure 6.40: PO discharge (#105784). Shown are density traces of DED and reference discharge as well as the temperature values and the DED current. PO discharge (#105784)Thomson profiles of electron density and temperature as well as their gradients.[Schmitz 09]. z is the vertical position, and the broken lines indicate the affected q-surface

Since figure 6.39 can only supply Abel-inverted measurements of the density for the PO scenario, figure 6.40 is supplying a much more detailed picture for a comparable discharge with available high resolution n_e and T_e from Thomson scattering measurements. For the discharges presented in table 6.1 the threshold for reaching the PO is at 2.5 kA DED current for the additional discharge the scenario was adapted to reach PO already at 1.5 kA.

Again the drop in density can be observed when comparing the perturbed and unperturbed discharge. In addition the highly resolved density and temperature profiles show the flattening of the edge gradients outside of the q=5/2 surface. This stands in clear contrast to the IPC scenario, where the gradients in the edge increased, showing the afore mentioned improvement of particle confinement.

Since the density loss and the onset of the PO at 2.5 kA are similarly connected to each other an analysis of the particle confinement as performed for the IPC has been carried out. This analysis is presented in figure 6.41 together with the zone widths for the ergodic and laminar zone (cf. section 3.2.2).

At 0kA DED the layer widths are zero and the normalized particle confinement time is unity.

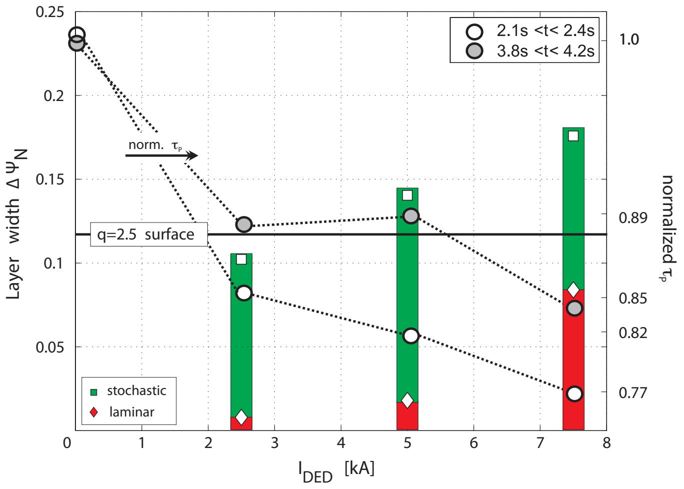

Figure 6.41: Decrease of particle confinement time τ_P with I_{DED} and corresponding evolution of laminar and ergodic layer width $\Delta\Psi_N$[Schmitz 09]

When increasing the DED amplitude the picture changes, the particle confinement time drops and the ergodic zone immediately jumps towards the q=5/2 surface. While the increase towards 5 kA is indifferent for the two measurements of the particle confinement time, the trend towards 7.5 kA and a drop of about 22 % in τ_P is evident. For this last step again the laminar zone again increases drastically, increasing the particle transport in the edge by SOL parallel particle and energy flows in the laminar flux tubes.

The description of the layer width corresponds to the evolution of the structures and the stochastization of the field lines shown in figure 6.42. The q=5/2 surface is almost reached by the perturbation at the low amplitude of the DED while the higher amplitudes cause stochastization of the island chain up to a level of complete stochastization. In contrast to the IPC the island chain is reached far earlier, the ergodiszation is significantly larger and hence the PO is caused immediately.

The early stages correspond to what has been seen in the high amplitude discharge presented during the IPC discharges. This means that the IPC and PO are two phases of the changes in magnetic topology due to influence of the DED.

While the low levels of stochastization and small doses of field lines connecting DED target and resonant island chain are causing the IPC, the increase in stochastization and in the end the increase in the laminar zone width is causing a decrease in particle confinement.

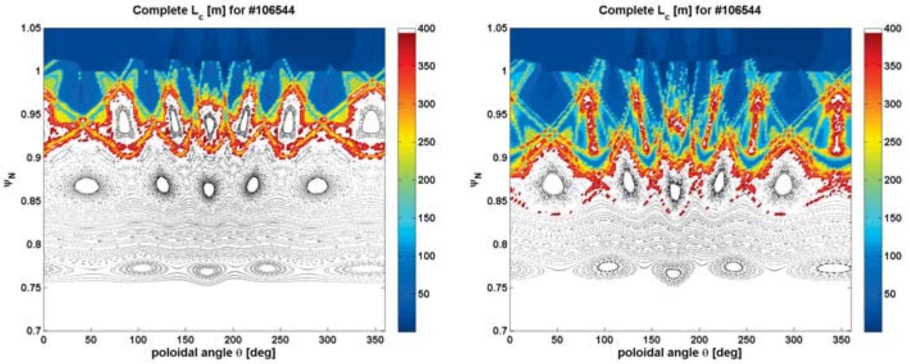

(a) PO Scenario @ I_{DED}=2.5kA (b) PO Scenario @ I_{DED}=5.0kA

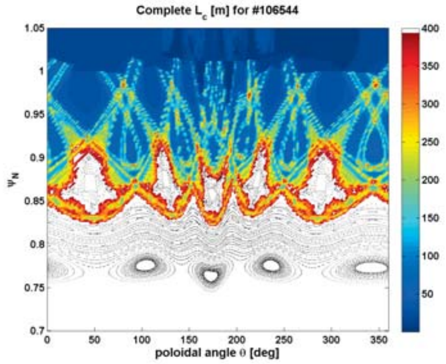

(c) PO Scenario @ I_{DED}=7.5kA

Figure 6.42: Magnetic topology calculations for the REVERSED PO scenario, based on Gourdon calculations. The connection length (color coded) as well as the Poincare plot is shown for three different amplitudes of the external magnetic perturbation (I_{DED}).

Without going into the details of the radial electric field behavior it can be said for the Pump Out the radial electric field is becoming more positive with increasing DED amplitude while the gradient remains flat at $q = 5/2$.

The shearing rate $\Omega_{\vec{E}\times\vec{B}}$ The gradient of the radial electric field and hence the shearing rate as given in equation 2.37 is much different in two aspects when compared to the IPC case.

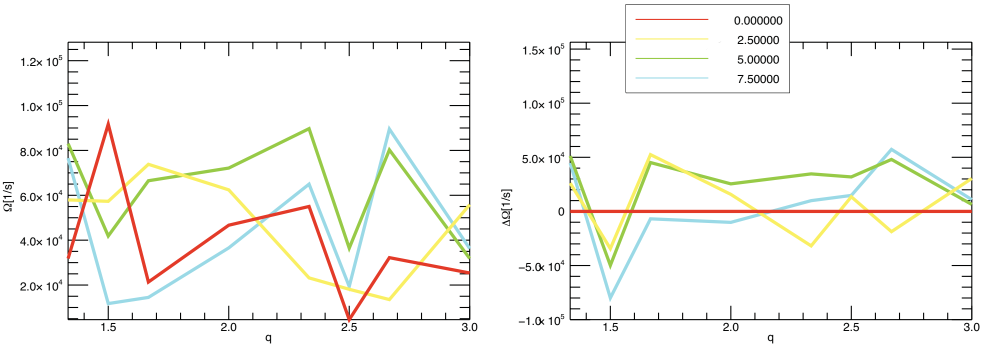

Figure 6.43: $\Omega_{\vec{E}\times\vec{B}}$ and $\Delta\Omega_{\vec{E}\times\vec{B}}$ calculated from the profiles acquired during PO in REVERSED configuration.

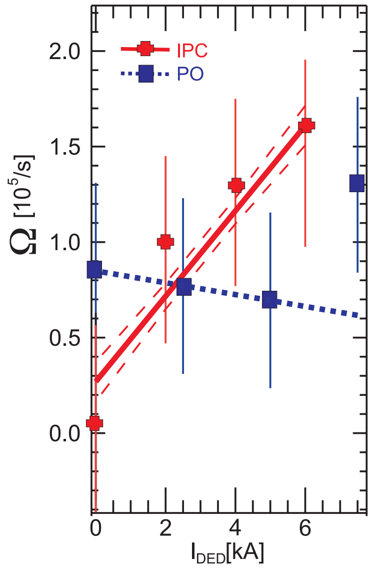

Figure 6.44: $\vec{E}\times\vec{B}$ shear rate vs. I_{DED} at the $q = 5/2$ surface for PO and IPC scenario.

Figure 6.43 is showing on the left side the absolute values of the shearing rate and on the right side the relative behavior with respect to the 0 kA discharge. Firstly, the absolute value close to the q=5/2 surface is low compared to the IPC case, secondly, the absolute shearing rate is an order of magnitude lower and is not showing the clear increase connected to the IPC. This is even clearer, when taking the relative values for the shearing rate. The profile is flat, not showing any increase or change around the q=5/2 surface.

This means that even though the general tendency, the increase in E_r, is similar between IPC and PO, the local changes of the shearing rate are not similar (fig. 6.44). While the small amount of field line connections in case of the IPC cause the potential to change locally at the resonant surface, the PO is dominated by the stochastic field lines and the large extend of the short connection length field lines present in the laminar zone.

In one case small amounts of field lines connect target and island chains and cause steep gradients in the E_r and density, improving the confinement, while in the other case (PO) the parallel transport along the field lines decreases the confinement due to strongly enhanced SOL like transport.

To complement the picture the following section will give a short overview on the influence of the DED onto the turbulent transport. Indications of suppressed or enhanced turbulent transport are found to be correlated with the existence of IPC and PO respectively.

6.3.3 Turbulent Transport and Plasma Fluctuations

The following section presents a comparison with turbulence measurements, during a IPC like discharges, derived via reflectometry at TEXTOR[Kramer-Flecken 06]. Data is available for a scenario similar to the IPC in DED m/n=3/1 configuration and for the presented PO discharges. The multi-horn antenna setup at TEXTOR allows measurement of correlation properties of the turbulence and its rotation.

As was seen in the discussion before, the IPC as well as the PO are connected to a local change in the transport. In the case of the IPC probably a zone of decreased transport is build up by a local change in $\vec{E} \times \vec{B}$ shear or poloidal flow. The understanding of local turbulence, its influence on the transport and the methods influencing it are of uttermost concern for the understanding of the IPC and PO scenarios.

A description of a plasma scenario, similar to the IPC discharges, can be found in [Kramer-Flecken 06] together with the methods used to deduce the turbulence correlation data and its detailed description.

The discharges [Kramer-Flecken 06] similar to the IPC are performed with 1.3 MW of counter heating and 0.3 MW of co NBI heating. The DED amplitude during the flat top phase is 2.5kA in 3/1 mode. During those discharge the diamagnetic energy increases as a sign of improved confinement in conjunction with an increase in density as shown before for the 6/2 base mode.

The toroidal rotation shows a change in amplitude towards the co-direction, effectively decreasing the predominant counter rotation, when comparing to the non DED discharges. The amount of 30 km/s is comparable to effects observed during the IPC discharges(see above). For the investigation of turbulence characteristics in [Kramer-Flecken 06] spectral and correlation analyses has been performed. Details of the procedure can be found in [Kramer-Flecken 06].

The lifetime of density fluctuations can be considered as a measure of the growth rate of instabilities. The developed instabilities lifetime can be deduced by the cross-correlation coefficients (γ) for several spatially distributed antennas and known turbulence velocity. Measuring the distribution of (γ) at different poloidal distances ($\Delta\Theta_i$) gives a gaussian line shape of which the FWHM l_c allows the average lifetime of the fluctuations to be determined as

$$\tau_{dc} = \frac{l_c}{v_{turb}}, \tag{6.8}$$

with v_{turb} being the linear turbulence velocity deduced by reflectometry.

In contrast to the fluctuations lifetime the density fluctuations can be deduced by single antenna data as given in [Kramer-Flecken 06, Kramer-Flecken 04] :

$$\frac{\langle|\partial n|^2\rangle^{0.5}}{n_c} \approx \langle\tilde{\Phi}\rangle \cdot \frac{\lambda_0}{4\pi \cdot 1.5 \cdot 2^{3/4}\sqrt{L_n \lambda_\perp}} \tag{6.9}$$

Here $\tilde{\Phi}$ is the phase fluctuation level in radians, λ_0 is the vacuum wavelength of the probing microwave and L_n is the density scale length. $\lambda_\perp$ is the poloidal wavelength of the turbulence , n_c the cut-off density.

So to answer the question regarding the connection of turbulence, transport and IPC a simple model regarding the transport, assuming a random walk process, is used [Liewer 85, Kramer-Flecken 06]. The diffusion coefficient (D_{RW}) is related to the turbulence properties by

$$D_{RW} = \frac{\lambda_r^2}{\tau_{dc}} \tag{6.10}$$

where λ_r and τ_{DC} can be determined from reflectometry measurements.

Figure 6.45(a) shows the properties deduced by reflectometry for the discharges as discussed above while figure 6.45(b) shows the diffusion coefficient D_{RW}. Evidence for the formation of a transport barrier were taken in [Kramer-Flecken 06] by the measurement of the quantities in shown figure 6.45(a). The density fluctuation in the upper part of the figure are decreasing outside of r/a=0.8 whereas they remain similar within this radius. The density fluctuation drop in absolute numbers 0.2 % points, meaning a decrease of about $\sim 15\%$.

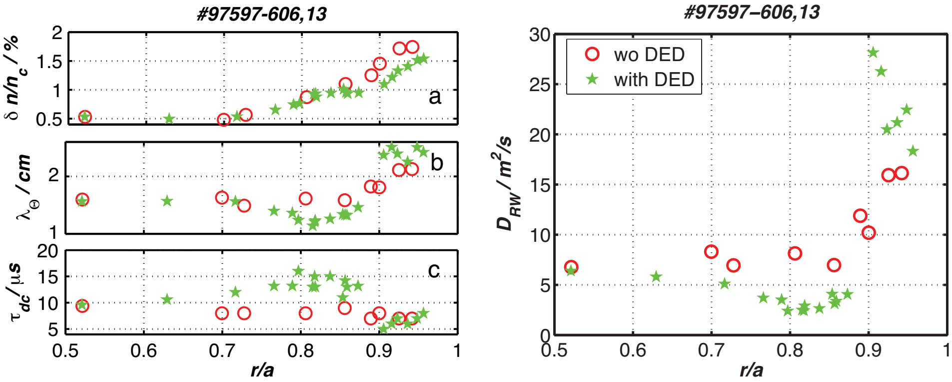

(a) Turbulence Properties, including density fluctuations poloidal wavelength and de-correlation time, deduced for DED and non-DED discharges

(b) Diffusion coefficients determined from the turbulence properties and compared for DED and non-DED discharges.

Figure 6.45: Plasmas similar to IPC, during 3/1 mode. Discharges with DED are denoted by ★ and those without by ○.[Kramer-Flecken 06].

Regarding the poloidal wavelength the situation is also correlated to changes inside and outside this radius (coinciding with the rational q surface). While the wavelength decreases around the radius of r/a 0.8 the wavelength even increases outside of r/a = 0.9, which then translates into the measure of density fluctuations observed.

The analysis of the turbulence lifetime, estimated from the different antenna correlation measurements presents a constant lifetime of 8 microseconds for the non-DED cases while the lifetime increases to 13 micro seconds during the DED operation in the region around r/a = 0.8 (figure 6.45(a)). When comparing this, or more exact $1/\tau_{DC}$, to the measured shear rate [Kramer-Flecken 06] and the shearing rate in 6.37(a) and 6.37(b) the turbulence life time is superseded by the shearing rate, hence strengthening the arguments for turbulent suppression.

Coming back to the random walk model one can then calculate the diffusion coefficient for the discharges in question. And compare this between the DED and non-DED discharges and the calculated topologies. Applying the DED reduces D_{RW} in the region $0.75 \leq r/a \leq 0.85$. In the laminar zone, D_{RW} increases again. This effect is in good agreement with the observation made in the IPC discharges, since at the rational q-surface the transport is changed towards better confinement while in the outward plasma edge $r/a \geq 0.9$ the laminar zone is taking effect.

Those observations — even though available only for the 3/1 configuration of the DED — confirm the observations made during the 6/2 IPC experiments presented here and show good agreement with the analyses made in [Biglari 90, Moyer 95, Burrell 97, Ida 98, Burrell 05]. The forming of a zone with reduced transport, or the increase in plasma confinement coincides with the increase in $\vec{E} \times \vec{B}$ shearing rate and hence a decrease in turbulent transport if and when the turbulent lifetime or its growth rate is superseded by the shearing rate.

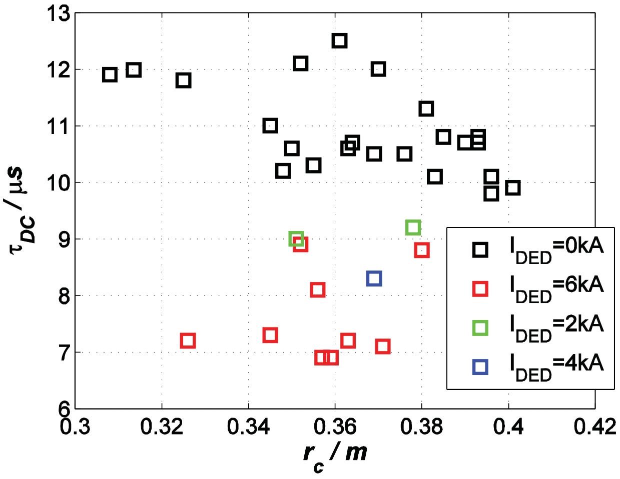

Figure 6.46: Turbulence life time for the discharges used in the PO analysis [Kraemer-Flecken 08]

To complement this, the turbulent lifetime was also measured for the PO scenario. The life time shown in figure 6.46 decreases by 30 % hence probably causing an increase in D_{RW} and coinciding with the drop in particle confinement time visible during the PO scenario presented in figure 6.41. Increasing the DED amplitude reduces the turbulent transport.

Chapter 7

Summary & Outlook

The aim of this work is the characterization of the radial electric field E_r at the tokamak TEXTOR under the influence of external Resonant Magnetic Perturbations (RMP) imprinted onto the helical tokamak field by means of the Dynamic Ergodic Divertor (DED). With respect to the influence of RMP the aspects of transport control in future fusion devices such as ITER, understanding improved confinement and control transient heat loads (ELMS) are some of the most prominent ones today. This work contributes to the understanding of how RMPs are changing the magnetic topology, the E_r as well as the plasma rotation to hence realize changes in confinement. High confinement modes in divertor tokamaks are typically connected to changes in the E_r and its shear . The DED provides a flexible tool to control plasma edge transport. The DED can be operated at different toroidal(m) and poloidal(n) mode configurations, m/n= 3/1, 6/2, 12/4. The 12/4 mode leads to a very shallow stochastic zone, while for 3/1 operation a deeper penetration is anticipated. At TEXTOR two scenarios are achieved with the DED (m/n=6/2): The Improved Particle Confinement (IPC) as well as the particle Pump Out (PO). The role of the E_r during confinement transitions with RMP is investigated.

In order to perform this work a diagnostic has been developed using Charge Exchange Recombination Spectroscopy (CXRS) on C^{6+}ions, induced by an active hydrogen diagnostic beam, observing the most intense visible transition. Doppler shift and spectral width are measured and from this poloidal and toroidal rotation as well as ion temperature and density are deduced.

For the measurement of rotation and temperature profiles a high spatial resolution is required. The hydrogen diagnostic beam used is of low divergence ($0.5°$) allowing a small radial resolution of 1-2 cm and is used in a modulated fashion (10Hz) in order to subtract the background. To ensure a radial calibration for the diagnostic a method was devised using active Beam Emission Spectroscopy (BES). The diagnostic beam interacting with hydrogen gas emits doppler shifted H_α light, hence allows the deduction of the radial position (by angle).

Signal intensity and hence photon statistics is one of the optimization criteria used in the course of diagnostic development and improvement. The beam performance was optimized by installing a new arc-discharge plasma box, improving the beam composition, while the optical systems were optimized for high transmission. Increased intensity improves the velocity resolution: ≥ 5km/s $\rightarrow\geq 0.7$km/s (poloidal); ≥ 10km/s $\rightarrow\geq 5$km/s(toroidal).

The poloidal observation was optimized by installing a direct imaging system on top of the tokamak vessel, improving transmission by a factor of 40, complementing the fiber transmitted channels observing from the bottom of the vessel. Together both systems utilize the differential Doppler shift approach to measure the reference wavelength. The toroidal observation system was developed with one optical fiber per radial channel and in course of the installation improved by a second set of fibers increasing the intensity by a factor of two. Measurements require a minimum integration time of 1.5 s (3 s modulated)(flat top of one TEXTOR discharge).

The capabilities of this new diagnostic are used in this work in order to consistenly measure and resolve even small changes in the E_r and its contributions under the influence of the DED.

The toroidal and poloidal rotation have been studied in this work under the influence of momentum input from Neutral Beam Injection as well as under the simultaneous inversion of toroidal field and plasma current. Both methods are used to establish a picture of the effects of external torque and magnetic configuration causing changes in the E_r before studying global confinement changes under the influence of the DED. The plasma current and toroidal field have opposite signs (helicity -1). The Neutral Beam can be injected in the direction of the plasma current (co) and in the opposite direction (counter) causing a spin up of the toroidal rotation accordingly, the poloidal rotation follows according to the flux surface averaged contribution to the poloidal force balance. Full co or counter heating means fast toroidal rotation (100 km/s) in the respective direction symmetrically between co and counter injection, while the poloidal rotation is symmetric ($\pm$3km/s) around an offset value of +3 km/s close to the plasma center following the neoclassical prediction for negative helicity.

The E_r as determined by the radial force balance consists of terms given by the toroidal and poloidal rotation as well as term given by the pressure gradient each being measured via CXRS. Besides the magnetic field the E_r is one of the crucial parameters determining radial transport of ions and electrons. Transport perpendicular to the field lines as well as open ergodic structures can influence the E_r, shear the rotation and change the confinement. Depending on the scenario each of the E_r contribution can be significant.

With respect to the presented study regarding global confinement effects under RMP, the contributions from toroidal and poloidal rotation to the E_r are the dominating ones, while the pressure gradient is negligible in TEXTOR plasmas. Contributions to the E_r are driven by external momentum input from NBI as well as by the ergodisation of the plasma edge via the DED.

Whereas in this work the role of the E_r and its shear during the transition into IPC and PO plays the most prominent role, the influence of the DED in general, without IPC and PO, is discussed as well. Those changes in E_r are the underlying contribution to the E_r with RMP (DED).

When increasing the DED current amplitude the toroidal rotation and poloidal rotation are changing towards the co direction or the so-called ion diamagnetic drift direction, respectively causing the E_r to change towards more positive values. This effect is caused by a $\vec{j} \times \vec{B}$ force originating in the ergodic zone close to the plasma edge (open field lines → electron loss → ion return current), spinning up the rotation.

During the operation of the DED the maximum observed change of E_r from toroidal rotation is $+6\,$kV/m over the whole observed profile ($0.5 \leq r/a \leq 1; 1.3 \leq q \leq 3.8$), while the poloidal rotation contributes up to $+6\,$kV/m depending on the local q. The total radial electric field is in the range between $-1\,$kV/m and $+10\,$kV/m for a typical TEXTOR plasma. The toroidal contribution is changed homogeneously over the whole profiles due to strong radial viscous coupling, while the neoclassical dampening for the poloidal contribution accentuates local changes (at rational q surfaces, especially $q = 5/2, q = 3$).

The transition into IPC is characterized by an increase in density ($\Delta n_e = 40\%$) and density gradients as well as particle confinement time ($\Delta\tau_p = 30\%$). The density increases inside of $q = 5/2$ with the gradients steepening outside of $q = 5/2$. The energy confinement follows the density, scaling with the increase in particles confined.

In the presented scenario the transition occurs at 2.5 kA (for $q_a = 3.8$), the stochastic zone is still not reaching the $q = 5/2$ surface and the laminar zones contribution to the parallel transport remains small. Field lines are connecting the ergodized island x-points with the DED target, thus the plasma flux is directed to the DED target. This causes the sheath potential to be changed and hence local changes deep inside the plasma (q=5/2). The onset of the IPC is consequently correlated with the $\vec{E} \times \vec{B}$ shearing rate increasing locally at $q = 5/2$. The shearing rate is probably connected to a suppression of turbulent transport when exceeding the actual turbulence growth rate at $q = 5/2$ and would directly contribute to improved confinement as seen also in H-Mode and biasing experiments performed previously at several machines.

After the transition into IPC the confinement increases further when increasing the external perturbation up to a point where the ergodization completely engulfs the island chain, effectively destroying the localization effect at $q = 5/2$.A broad ergodic and in addition a much broader laminar zone now causes enhanced outward transport, weakening the confinement.

The transition appearing at high perturbation amplitude is changing the effect of the DED towards the PO scenario. This scenario can be achieved by changing the position of the q=5/2 island chain with respect to the DED coils by changing the edge q. The PO scenario is showing a decrease in density and particle confinement time in the order of 30 %, while also showing an increase in turbulent transport. In contrast to the IPC no local increase in E_r shearing is observed. The transition is triggered already at low perturbation ($I_{DED} = 2.5$kA) with the stochastic behavior extends already to the resonant q surfaces (island chain) enhancing parallel transport. At higher perturbation the laminar zone grows causing further confinement degradation.

This work contributes to the knowledge assembled regarding RMPs influencing plasma transport as well as the underlying changes of magnetic topology and the consequences for plasma confinement. It allows to study the behavior of tokamak confinement with changing E_r using the DED as the controlling tool. It presents evidence for the forces originating from an ergodic plasma boundary as well as evidence for the connection between $\vec{E} \times \vec{B}$ shearing rate $\Omega_{\vec{E}\times\vec{B}}$, turbulent transport and confinement transitions.

Using the DED as a tool influencing dedicated rational surfaces evidently causes a transition into IPC via increased shearing. Especially the poloidal rotation is changed and thus is causing the increase in $\Omega_{\vec{E}\times\vec{B}}$ shear. This shearing phenomenon during the IPC is similar to the pressure gradient driven $\vec{E} \times \vec{B}$ shear during H-Mode in divertor machines or experiments with actively controlled H-mode via E_r biasing. Even though all three modes (IPC, H-Mode, ”Biasing”) reach a sheared E_r and confinement improvement under different circumstances, the study of sheared E_r in this work allows to deliver a very detailed picture of IPC properties and development which evidently connects the changes in magnetic topology directly with the increase in $\vec{E} \times \vec{B}$ shear and τ_p. The question of causality remains, the balance between E_r, rotation and confinement is prohibiting the question to be actually answered. This study again stresses the relevance of E_r shear for the transition.

The study is very conclusive when it comes to the experimental results, so far a detailed model has not been applied to the findings. A more detailed database would be required. Since the changes to the E_r and the confinement can be gradually controlled by the DED this allows a deep insight into the confinement transition. In the future a more detailed scan (I_{DED}, q_a, Heating, DED configuration) for the IPC and PO scenarios, including turbulence diagnostics, should be conducted. A detailed model would allow a prediction of the global confinement scenarios available in ITER and in a future fusion power plant.

Beyond the fact that the E_r shear is evidently one of the major contribution to confinement transitions the question remains what different collisionality regimes together with different turbulence behavior in devices such as ITER or DEMO mean for the actual confinement transitions and the suppression of turbulent energy and particle transport.

Bibliography

[Abdullaev 99] S. S. Abdullaev, K. H. Finken & K. H. Spatschek. *Asymptotical and mapping methods in study of ergodic divertor magnetic field in a toroidal system*. Physics Of Plasmas, vol. 6, no. 1, pages 153–174, 1999.

[Abdullaev 03] S.S. Abdullaev. *Overview of magnetic structure induced by the TEXTOR-DED and the related transport*. Nuclear fusion, vol. 43, no. 5, pages 299–313, 2003.

[Aymar 02] R. Aymar, P. Barabaschi, Y. Shimomura & The ITER Team. *The ITER design*. Plasma Physics And Controlled Fusion, vol. 44, no. 5, pages 519–565, 2002.

[Becoulet 03] M. Becoulet, G. Huysmans, Y. Sarazin, X. Garbet, P. Ghendrih, F. Rimini, E. Joffrin, X. Litaudon, P. Monier-Garbet, J. M. Ane, P. Thomas, A. Grosman, V. Parail, H. Wilson, P. Lomas, P. DeVries, K. D. Zastrow, G. F. Matthews, J. Lonnroth, S. Gerasimov, S. Sharapov, M. Gryaznevich, G. Counsell, A. Kirk, M. Valovic, R. Buttery, A. Loarte, G. Saibene, R. Sartori, A. Leonard, P. Snyder, L. L. Lao, P. Gohil, T. E. Evans, R. A. Moyer, Y. Kamada, A. Chankin, N. Oyama, T. Hatae, N. Asakura, O. Tudisco, E. Giovannozzi, F. Crisanti, C. P. Perez, H. R. Koslowski, T. Eich, A. Sips, L. Horton, A. Hermann, P. Lang, J. Stober, W. Suttrop, P. Beyer, S. Saarelma & JET-EFDA Workprogramme. *Edge localized mode physics and operational aspects in tokamaks*. Plasma Physics And Controlled Fusion, vol. 45, pages A93–A113, 2003.

[Biglari 90] H. Biglari, P. H. Diamond & P. W. Terry. *Influence of sheared poloidal rotation on edge turbulence*. Physics of Fluids B: Plasma Physics, vol. 2, no. 1, pages 1–4, 1990.

[Biot 20] J.-B. Biot & F. Savart. *Note sur le Magnétisme Note de la pile de Volta*. Annales Chim. Phys., vol. 15, pages 222–223, 1820.

[Bogen 95] P. Bogen, J. D. Hey, E. Hintz, Y. T. Lie, D. Rusbuldt & U. Samm. *Spectroscopic Measurements Of The Ion Temperature In Front Of A Tokamak Limiter*. Journal Of Nuclear Materials, vol. 220, pages 472–477, 1995.

[Brezinsek 05a] S. Brezinsek, A. Huber, S. Jachmich, A. Pospieszczyk, B. Schweer & G. Sergienko. *Plasma edge diagnostics for TEXTOR*. Fusion Science And Technology, vol. 47, no. 2, pages 209–219, 2005.

[Brezinsek 05b] S. Brezinsek, G. Sergienko, A. Pospieszczyk, P. Mertens, U. Samm & P. T. Greenland. *Characterization of the deuterium recycling flux in front of a graphite surface in the TEXTOR tokamak*. Plasma Physics And Controlled Fusion, vol. 47, no. 4, pages 615–634, 2005.

[Burrell 94] K. H. Burrell, E. J. Doyle, P. Gohil, R. J. Groebner, J. Kim, R. J. Lahaye, L. L. Lao, R. A. Moyer, T. H. Osborne, W. A. Peebles, C. L. Rettig, T. H. Rhodes & D. M. Thomas. *Role Of The Radial Electric-Field In The Transition From L (Low) Mode To H (High) Mode To VH (Very High) Mode In The DIII-D Tokamaks*. Physics Of Plasmas, vol. 1, no. 5, pages 1536–1544, May 1994.

[Burrell 97] K. H. Burrell. *Effects of ExB velocity shear and magnetic shear on turbulence and transport in magnetic confinement devices*. Physics Of Plasmas, vol. 4, no. 5, pages 1499–1518, 1997.

[Burrell 05] K. H. Burrell. *Role of E x B shear and magnetic shear in the formation of transport barriers in DIII-D*. Fusion Science And Technology, vol. 48, pages 1021–1041, 2005.

[Busch 05] C. Busch, B. Unterberg, U. Samm & B. Schweer. *Impact of the DED on ion transport and poloidal rotation at TEXTOR*. Europhysics Conference Abstracts, 2005.

[Busch 06] C. Busch. Spektroskopische untersuchungen der poloidalen plasmarotation unter dem einfluss statischer und dynamischer ergodisierung am tokamak textor, volume 50 of *”Schriften des Forschungszentrums Juelich”*. Forschungszentrum Juelich GmbH, ”energy technology” edition, 2006. ISBN 3-89336-433-1.

[Carmona 06] J. M. Carmona, K. J. McCarthy, R. Balbin & S. Petrov. *Charge-exchange spectroscopic diagnostic for the TJ-II stellarator*. Review Of Scientific Instruments, vol. 77, no. 10, 2006.

[Chen 85] Francis F. Chen. Introduction to plasma physics and controlled fusion, volume 1. Plenum Press (New York & London), 2 edition, 1985.

[Claassen 90] H. A. Claassen, R. P. Schorn, H. Gerhauser & E. Hintz. *Radial Density Profiles Of Highly Charged Carbon-Ions In Textor*. Journal Of Nuclear Materials, vol. 176, pages 398–403, 1990.

[Coenen 08] J.W. Coenen, M. Clever, K. H. Finken, H. Frerichs, M.W. Jakubowski, M. Lehnen, M. Mitri, U. Samm, B. Schweer, O. Schmitz, H. Stoschus, B Unterberg & the Textor-Team. *”Spectroscopic Measurements of the radial electric field under conditions of improved particle cofinement*

(IPC) with the Dynamic Ergodic Divertor (DED) in the Tokamak TEXTOR”. In Europhysics Conference Abstracts, volume 32D of *ECA*, pages P–4016, 2008. ”Spectroscopic Measurements of the radial electric field under conditions of improved particle cofinement (IPC) with the Dynamic Ergodic Divertor (DED) in the Tokamak TEXTOR”.

[Coenen 09] J.W. Coenen, B. Unterberg, U. Samm, B. Schweer, M. Clever & O. Schmitz. *Charge Exchange Recombination Spectroscopy on a Hydrogen Diagnostic Beam for Measurements of Impurity Rotation and Radial Electric Field at the Tokamak TEXTOR*. submitted to Review Of Scientific Instruments, 2009.

[Cole 06] A. Cole & R. Fitzpatrick. *Drift-Magnetohydrodynamical Model of Error-field Penetration in Tokamak Plasmas*. Physics Of Plasmas, vol. 13, page 032503, 2006.

[Condrea 99] I. Condrea, E. Haddad, B. C. Gregory, D. Lafrance, J. L. Lachambre, G. Pacher, F. Meo & H. H. Mai. *Ion temperature and plasma rotation velocity measurements using visible spectroscopy on TdeV*. Review Of Scientific Instruments, vol. 70, no. 1, pages 387–390, 1999.

[Conway 04] G. D. Conway, J. Schirmer, S. Klenge, W. Suttrop, E. Hozhauer & ASDEX Upgrade Team. *Plasma rotation profile measurements using Doppler reflectometry*. Plasma Physics And Controlled Fusion, vol. 46, no. 6, pages 951–970, 2004.

[Cornelis 94] J. Cornelis, R. Sporken, G. VanOost & R. R. Weynants. *Predicting The Radial Electric-Field Imposed By Externally Driven Radial Currents In Tokamaks*. Nuclear Fusion, vol. 34, no. 2, pages 171–183, 1994.

[de Blank 08] H. J. de Blank. *Guiding center motion*. Fusion Science And Technology, vol. 53, no. 2T, pages 59–67, 2008.

[De Bock 08] M. F. M. De Bock, I. G. J. Classen, C. Busch, R. J. E. Jaspers, H. R. Koslowski, B. Unterberg & TEXTOR Team. *The interaction between plasma rotation, stochastic fields and tearing mode excitation by external perturbation fields*. Nuclear Fusion, vol. 48, no. 1, 2008.

[deGrassie 03] J. S. deGrassie, D. R. Baker, K. H. Burrell, P. Gohil, C. M. Greenfield, R. J. Groebner & D. M. Thomas. *Toroidal rotation in neutral beam heated discharges in DIII-D*. Nuclear Fusion, vol. 43, no. 2, pages 142–156, 2003.

[Deichuli 05] P. P. Deichuli, A. A. Ivanov, V. V. Mishagin, A. V. Sorokin, N. V. Stupishin & G. I. Shulzhenko. *Multi-seconds diagnostic neutral beam injector based on arc-discharge with LaB6 hollow cathode*. Fusion Science And Technology, vol. 47, no. 1T, pages 330–332, 2005.

[Delabie 08] E. Delabie. *Private Communication*, January 2008.

[DeMichelis 95] C. DeMichelis, A. Grosman, X. Garbet, P. Ghendrih, M. Goniche, W. Hess, C. Laviron, T. Loarer, M. Mattioli, P. Moniergarbet, B. Saoutic, F. Clairet, D. Guilhem, R. Guirlet, G. T. Hoang & J. Lasalle. *Characteristics Of Ergodic Divertor Plasmas In The Tore Supra Tokamak*. Nuclear Fusion, vol. 35, no. 9, pages 1133–1153, 1995.

[Donne 05] A. J. H. Donne, M. F. M. De Bock, I. G. J. Classen, M. G. Von Hellermann, K. Jakubowska, R. Jaspers, C. J. Barth, H. J. Van der Meiden, T. Oyevaar, M. J. Van de Pol, S. K. Varshney, G. Bertschinger, W. Biel, C. Busch, K. H. Finken, H. R. Koslowski, A. Kramer-Flecken, A. Kreter, Y. Liang, H. Oosterbeek, O. Zimmermann, G. Telesca, G. Verdoolaege, C. W. Domier, N. C. Luhmann, E. Mazzucato, T. Munsat, H. Park, M. Kantor, D. Kouprienko, A. Alexeev, S. Ohdachi, S. Korsholm, P. Woskov, H. Bindslev, F. Meo, P. K. Michelsen, S. Michelsen, S. K. Nielsen, E. Tsakadze & L. Shmaenok. *Overview of core diagnostics for TEXTOR*. Fusion Science And Technology, vol. 47, no. 2, pages 220–245, 2005.

[Doppler 42] Ch. Doppler. *Ueber das farbige Licht der Doppelsterne und einiger anderer Gestirne des Himmels*. Boehmische Gesellschaft der Wissenschaften, Prag, 1842.

[Dreval 08] M. Dreval, C. Xiao, D. Trembach, A. Hirose, S. Elgriw, A. Pant, D. Rohraff & T. Niu. *Simultaneous evolution of plasma rotation, radial electric field, MHD activity and plasma confinement in the STOR-M tokamak*. Plasma Physics And Controlled Fusion, vol. 50, no. 9, page 095014, September 2008.

[Duval 07] B. P. Duval, A. Bortolon, A. Karpushov, R. A. Pitts, A. Pochelon, A. Scarabosio & Tcv Team. *Bulk plasma rotation in the TCV tokamak in the absence of external momentum input*. Plasma Physics And Controlled Fusion, vol. 49, pages B195–B209, 2007.

[Einstein 05] A. Einstein. *Zur Elektrodynamik bewegter Koerper*. Annalen der Physik und Chemie, vol. 17, pages 891–921, 1905.

[Evans 04] T. E. Evans, R. A. Moyer, P. R. Thomas, J. G. Watkins, T. H. Osborne, J. A. Boedo, E. J. Doyle, M. E. Fenstermacher, K. H. Finken, R. J. Groebner, M. Groth, J. H. Harris, R. J. La Haye, C. J. Lasnier, S. Masuzaki, N. Ohyabu, D. G. Pretty, T. L. Rhodes, H. Reimerdes, D. L. Rudakov, M. J. Schaffer, G. Wang & L. Zeng. *Suppression of large edge-localized modes in high-confinement DIII-D plasmas with a stochastic magnetic boundary*. Physical Review Letters, vol. 92, no. 23, 2004.

[Evans 06a] T. E. Evans, K. H. Burrell, M. E. Fenstermacher, R. A. Moyer, T. H. Osborne, M. J. Schaffer, W. P. West, L. W. Yan, J. A. Boedo, E. J. Doyle, G. L. Jackson, I. Joseph, C. J. Lasnier, A. W. Leonard, T. L. Rhodes,

P. R. Thomas, J. G. Watkins & L. Zeng. *The physics of edge resonant magnetic perturbations in hot tokamak plasmas*. Physics Of Plasmas, vol. 13, no. 5, 2006.

[Evans 06b] T. E. Evans, R. A. Moyer, K. H. Burrell, M. E. Fenstermacher, I. Joseph, A. W. Leonard, T. H. Osborne, G. D. Porter, M. J. Schaffer, P. B. Snyder, P. R. Thomas, J. G. Watkins & W. P. West. *Edge stability and transport control with resonant magnetic perturbations in collisionless tokamak plasmas*. Nature Physics, vol. 2, no. 6, pages 419–423, June 2006.

[Finken 98] K. H. Finken. *The Dynamic Ergodic Divertor*. Fusion Technology, vol. 33, no. 2T, pages 291–296, 1998.

[Finken 99a] K. H. Finken, S. S. Abdullaev, T. Eich, G. Mank & A. Rogister. *Electric field generation in the plasma boundary by the Dynamic Ergodic Divertor (DED)*. Czechoslovak Journal Of Physics, vol. 49, pages 93–101, 1999.

[Finken 99b] K. H. Finken, S. S. Abdullaev, A. Kaleck & G. H. Wolf. *Operating space of the Dynamic Ergodic Divertor for TEXTOR-94*. Nuclear Fusion, vol. 39, no. 5, pages 637–662, 1999.

[Finken 01] K. H. Finken, S. S. Abdullaev, T. Eich, D. W. Faulconer, M. Kobayashi, R. Koch, G. Mank & A. Rogister. *Plasma rotation induced by the Dynamic Ergodic Divertor*. Nuclear Fusion, vol. 41, no. 5, pages 503–511, 2001.

[Finken 04] K. H. Finken, S. S. Abdullaev, M. Jakubowski, M. Lehnen & G. Sewell. *Modelling of the field line penetration and force transfer by the dynamic ergodic divertor of TEXTOR*. Nuclear Fusion, vol. 44, no. 6, pages S55–S63, 2004.

[Finken 05a] K. H. Finken, S. S. Abduallaev, M. Jakubowski, M. Lehnen, A. Nicolai & K. H. Spatschek. The structure of magnetic field in the textor-ded. Energietechnik / Energy Technology. Forschungszentrum Juelich GmbH, 2005.

[Finken 05b] K. H. Finken, S. S. Abdullaev, M. F. M. de Bock, M. von Hellermann, M. Jakubowski, R. Jaspers, H. R. Koslowski, A. Kramer-Flecken, M. Lehnen, Y. Liang, A. Nicolai, R. C. Wolf, O. Zimmermann, M. de Baar, G. Bertschinger, W. Biel, S. Brezinsek, C. Busch, A. J. H. Donne, H. G. Esser, E. Farshi, H. Gerhauser, B. Giesen, D. Harting, J. A. Hoekzema, G. M. D. Hogeweij, P. W. Huttemann, S. Jachmich, K. Jakubowska, D. Kalupin, F. Kelly, Y. Kikuchi, A. Kirschner, R. Koch, M. Korten, A. Kreter, J. Krom, U. Kruezi, A. Lazaros, A. Litnovsky, X. Loozen, N. J. L. Cardozo, A. Lyssoivan, O. Marchuk, G. Matsunaga, P. Mertens, A. Messiaen, O. Neubauer, N. Noda, V. Philipps, A. Pospieszczyk, D. Reiser, D. Reiter, A. L. Rogister, M. Sakamoto, A. Savtchkov, U. Samm, O. Schmitz, R. P. Schorn, B. Schweer, F. C.

Schuller, G. Sergienko, K. H. Spatschek, G. Telesca, M. Tokar, R. Uhlemann, B. Unterberg, G. Van Oost, T. Van Rompuy, G. Van Wassenhove, E. Westerhof, R. Weynants, S. Wiesen & Y. H. Xu. *Toroidal plasma rotation induced by the Dynamic Ergodic Divertor in the TEXTOR tokamaks*. Physical Review Letters, vol. 94, no. 1, 2005.

[Finken 07a] K. H. Finken, S. S. Abdullaev, M. W. Jakubowski, M. F. M. de Bock, S. Bozhenkov, C. Busch, M. von Hellermann, R. Jaspers, Y. Kikuchi, A. Kramer-Flecken, M. Lehnen, D. Schega, O. Schmitz, K. H. Spatschek, B. Unterberg, A. Wingen, R. C. Wolf, O. Zimmermann & TEXTOR Team. *Improved confinement due to open ergodic field lines imposed by the dynamic ergodic divertor in TEXTOR*. Physical Review Letters, vol. 98, no. 6, 2007.

[Finken 07b] K. H. Finken, B. Unterberg, Y. Xu, S. S. Abdullaev, M. Jakubowski, M. Lehnen, M. F. M. de Bock, S. Bozhenkov, S. Brezinsek, C. Busch, I. G. J. Classen, J. W. Coenen, D. Harting, M. von Hellermann, S. Jachmich, R. J. E. Jaspers, Y. Kikuchi, A. Kramer-Flecken, Y. Liang, M. Mitri, P. Peleman, A. Pospieszczyk, D. Reiser, D. Reiter, U. Samm, D. Schega, O. Schmitz, S. Soldatov, M. Van Schoor, M. Vergote, R. R. Weynants, R. Wolf, O. Zimmermann & TEXTOR Team. *Influence of the dynamic ergodic divertor on transport properties in TEXTOR*. Nuclear Fusion, vol. 47, pages 522–534, 2007.

[Fonck 84] R. J. Fonck, D. S. Darrow & K. P. Jaehnig. *Determination Of Plasma-Ion Velocity Distribution Via Charge-Exchange Recombination Spectroscopy*. Physical Review A, vol. 29, no. 6, pages 3288–3309, 1984.

[Gangadhara 06] S. Gangadhara, D. Craig, D. A. Ennis & D. J. Den Hartog. *Modeling fast charge exchange recombination spectroscopy measurements from the Madison Symmetric Torus*. Review Of Scientific Instruments, vol. 77, no. 10, 2006.

[Geissler 08] H. Geissler. *Geissler Tube*. Encyclopedia Britannica Online, 2008.

[Geskus 03] D. Geskus. Design of a new system for spectroscopic measurements of the species fractions in the diagnostic hydrogen beam at textor. Forschungszentrum Juelich GmbH, 2003.

[Ghendrih 96] P. Ghendrih, A. Grosman & H. Capes. *Theoretical and experimental investigations of stochastic boundaries in tokamaks*. Plasma Physics And Controlled Fusion, vol. 38, no. 10, pages 1653–1724, 1996.

[Gourdon 70] C. Gourdon. *Programme Optimise de Calculs Numeriques Dans le Configurations Magnetique Toroidales*. CEN, Fontenay aux Roses, 1970.

[Gray 98] D. S. Gray, J. A. Boedo, M. Baelmans, R. W. Conn, R. A. Moyer, K. H. Dippel, K. H. Finken, A. Pospieszczyk, D. Reiter, R. P. Doerner, D. L. Hillis, G. Mank, G. H. Wolf & TEXTOR Team. *Plasma exhaust and* *density control in tokamak fusion experiments with neutral beam or ICRF auxiliary heating*. Nuclear Fusion, vol. 38, no. 11, pages 1585–1606, 1998.

[Groebner 90] R. J. Groebner, K. H. Burrell, P. Gohil & R. P. Seraydarian. *Spectroscopic Study Of Edge Poloidal Rotation And Radial Electric-Fields In The Diii-D Tokamak*. Review Of Scientific Instruments, vol. 61, no. 10, pages 2920–2925, 1990.

[Hahm 95] T. S. Hahm & K. H. Burrell. *Flow Shear-Induced Fluctuation Suppression In Finite Aspect Ratio Shaped Tokamak Plasma*. Physics Of Plasmas, vol. 2, no. 5, pages 1648–1651, 1995.

[Hawkes 92] N.C. Hawkes & N. Peacock. *A novel multichord spectrometer for plasma velocity measurements*. Reviews of Plasma Physics, vol. 63, no. 11, page 5164, 1992.

[Helander 01] P. Helander & D.J. Sigmar. Collisional transport in magnetized plasma. Cambridge monographs on plasma physics ; 4. Cambridge University Press, 2001.

[Hess 95] W. R. Hess, C. Demichelis, M. Mattioli, F. Clairet, M. Druetta, A. Grosman, R. Guirlet, T. Hutter, J. Lasalle & P. Moniergarbet. *Experimental-Study Of Ergodic Edge Plasmas With Marfes In Tore-Supra*. Plasma Physics And Controlled Fusion, vol. 37, no. 9, pages 951–973, 1995.

[Hey 93] J.D. Hey, T. Lie, D. Ruesbult & Hintz.E. . In Proc. 20th EPS Conference on Controlled Fusion and Plasma Physics, volume 17C, pages 1111 , Part III, Lisbon, 1993.

[Hey 94] J. D. Hey, Y. T. Lie, D. Rusbuldt & E. Hintz. *Doppler Broadening And Magnetic-Field Effects On Some Ion Impurity Spectra Emitted In The Boundary-Layer Of A Tokamak Plasma*. Contributions To Plasma Physics, vol. 34, no. 6, pages 725–747, 1994.

[Horton 08] L. D. Horton. *Physics issues for demo*. Fusion Science And Technology, vol. 53, no. 2T, pages 468–473, 2008.

[Huber 00] A. Huber, A. Pospieszczyk, B. Unterberg, M. Brix, P. Mertens, V. Philipps & B. Schweer. *Spectroscopic measurements of the ion temperature profile in front of a limiter in TEXTOR-94*. Plasma Physics And Controlled Fusion, vol. 42, no. 5, pages 569–578, 2000.

[Ida 90] K. Ida, S. Hidekuma, Y. Miura, T. Fujita, M. Mori, K. Hoshino, N. Suzuki & T. Yamauchi. *Edge Electric-Field Profiles Of H-Mode Plasmas In The Jft-2m Tokamak*. Physical Review Letters, vol. 65, no. 11, pages 1364–1367, 1990.

[Ida 98] K. Ida. *Experimental studies of the physical mechanism determining the radial electric field and its radial structure in a toroidal plasma*. Plasma Physics And Controlled Fusion, vol. 40, no. 8, pages 1429–1488, August 1998.

[Isler 94] R. C. Isler. *An Overview Of Charge-Exchange Spectroscopy As A Plasma Diagnostic*. Plasma Physics And Controlled Fusion, vol. 36, no. 2, pages 171–208, 1994.

[Ivanov 04] A. A. Ivanov, P. P. Deichuli, A. Kreter, V. V. Maximov, B. Schweer, I. V. Shikhovtsev, N. V. Stupishin, D. V. Usoltsev, A. A. Podminogin & R. Uhlemann. *Characterization of ion species mix of the TEXTOR diagnostic hydrogen beam injector with a rf and arc-discharge plasma box*. Review Of Scientific Instruments, vol. 75, no. 5, pages 1822–1825, 2004.

[Jakubowski 04a] M. W. Jakubowski. Magnetic field topology and heat flux patterns under the influence of the dynamic ergodic divertor of the textor tokamak, volume Juel-4143 of *Berichte des Forschungszentrums Juelich*. Forschungszentrum Juelich GmbH, 2004. PHDthesis.

[Jakubowski 04b] M. W. Jakubowski, S. S. Abdullaev, K. H. Finken & TEXTOR Team. *Modelling of the magnetic field structures and first measurements of heat fluxes for TEXTOR-DED operation*. Nuclear Fusion, vol. 44, no. 6, pages S1–S11, 2004.

[Jakubowski 06] M. W. Jakubowski, O. Schmitz, S. S. Abdullaev, S. Brezinsek, K. H. Finken, A. Kramer-Flecken, M. Lehnen, U. Samm, K. H. Spatschek, B. Unterberg, R. C. Wolf & TEXTOR Team. *Change of the magnetic-field topology by an ergodic divertor and the effect on the plasma structure and transport*. Physical Review Letters, vol. 96, 2006.

[Jakubowski 07] M. W. Jakubowski, A. Wingen, S. S. Abdullaev, K. H. Finken, M. Lehnen, K. H. Spatschek, R. C. Wolf & TEXTOR Team. *Observation of the heteroclinic tangles in the heat flux pattern of the ergodic divertor at TEXTOR*. Journal Of Nuclear Materials, vol. 363, pages 371–376, 2007.

[Kaganovich 98] I. Kaganovich & V. Rozhansky. *Transverse conductivity in a braided magnetic field*. Physics Of Plasmas, vol. 5, no. 11, pages 3901–3909, 1998.

[Kim 91] Y. B. Kim, P. H. Diamond & R. J. Groebner. *Neoclassical Poloidal And Toroidal Rotation In Tokamaks*. Physics Of Fluids B-Plasma Physics, vol. 3, no. 8, pages 2050–2060, 1991.

[Koch 08] R. Koch. *The coupling of electromagnetic power to plasmas*. Fusion Science And Technology, vol. 53, no. 2T, pages 184–193, 2008.

[Kraemer-Flecken 08] A. Kraemer-Flecken, D. Reiser, Y. Liang, O. Schmitz & The TEXTOR Team. *Interaction between Turbulence and Resonant Magnetic Perturbations*. In 13th EU-US TTF Workshop, 2008.

[Kramer-Flecken 04] A. Kramer-Flecken, V. Dreval, S. Soldatov, A. Rogister, V. Vershkov & TEXTOR-team. *Turbulence studies with means of reflectometry at TEXTOR*. Nuclear Fusion, vol. 44, no. 11, pages 1143–1157, 2004.

[Kramer-Flecken 06] A. Kramer-Flecken, S. Soldatov, C. Busch, Y. Liang, M. von Hellermann, R. Wolf, O. Zimmermann & TEXTOR-Team. *Reflectometry measurements during operation of the dynamic ergodic divertor at TEXTOR*. Nuclear Fusion, vol. 46, no. 9, pages S730–S742, 2006.

[Kreter 01] A. Kreter. Ladungsaustauschspektroskopie mit hilfe des wasserstoffdiagnostiksrahls am tokamak textor-94, volume Juel-3860 of *Berichte des Forschungszentrum Juelich*. Forschungszentrum Juelich GmbH, 2001.

[Last 03] A. Last & J Mohr. *Fehllicht in LIGA-Mikrospektrometern*. Wissenschaftliche Berichte FZKA, vol. 6885, page 31, 2003. Institut fuer Mikrostrukturtechnik.

[Lehnen 00] M. Lehnen. Untersuchungen der plasmarandschichtstruktur im tokamak textor-94 mittels der heliumstrahldiagnostik, volume 3835 of *Berichtes des Forschungszentrum Juelich*. Forschungszentrum Juelich GmbH, 2000.

[Lehnen 01] M. Lehnen, M. Brix, H. Gerhauser, B. Schweer & R. Zagorski. *Investigations on density and temperature asymmetries due to drift motions in the boundary layer of TEXTOR-94*. Journal of Nuclear Materials, vol. 290-293, pages 663–667, March 2001.

[Lehnen 05a] M. Lehnen, S. Abdullaev, W. Biel, M. F. M. de Bock, S. Brezinsek, C. Busch, I. Classen, K. H. Finken, M. von Hellermann, S. Jachmich, M. Jakubowski, R. Jaspers, H. R. Koslowski, A. Kramer-Flecken, Y. Kikuchi, Y. Liang, A. Nicolai, A. Pospieszczyk, T. Van Rompuy, U. Samm, O. Schmitz, G. Sergienko, B. Unterberg, R. Wolf, O. Zimmermann & TEXTOR Team. *Transport and divertor properties of the dynamic ergodic divertor*. Plasma Physics And Controlled Fusion, vol. 47, pages B237–B248, 2005.

[Lehnen 05b] M. Lehnen, S. S. Abdullaev, W. Biel, S. Brezinsek, K. H. Finken, D. Harting, M. von Hellermann, M. Jakubowski, R. Jaspers, M. Kobayashi, H. R. Koslowski, A. Kramer-Flecken, G. Matsunaga, A. Pospieszczyk, D. Reiter, T. Van Rompuy, U. Samm, O. Schmitz, G. Sergienko, B. Unterberg, R. Wolf, O. Zimmermann & TEXTOR team. *First results from the dynamic ergodic divertor at TEXTOR*. Journal Of Nuclear Materials, vol. 337, no. 1-3, pages 171–175, 2005.

[Lehnen 08] M. Lehnen. *”The Real Major Radius at Textor”*. private communication, 2008.

[Leonard 99] A. W. Leonard, A. Herrmann, K. Itami, J. Lingertat, A. Loarte, T. H. Osborne, W. Suttrop, ITER Divertor Modeling, Database Expert Grp & ITER Divertor Physics Expert Grp. *The impact of ELMs on the ITER divertor*. Journal Of Nuclear Materials, vol. 269, pages 109–117, 1999.

[Liang 07] Y. Liang, H. R. Koslowski, P. R. Thomas, E. Nardon, B. Alper, P. Andrew, Y. Andrew, G. Arnoux, Y. Baranov, M. Becoulet, M. Beurskens, T. Biewer, M. Bigi, K. Crombe, E. De La Luna, P. de Vries, W. Fundamenski, S. Gerasimov, C. Giroud, M. P. Gryaznevich, N. Hawkes, S. Hotchin, D. Howell, S. Jachmich, V. Kiptily, L. Moreira, V. Parail, S. D. Pinches, E. Rachlew & O. Zimmermann. *Active Control of Type-I Edge-Localized Modes with n = 1 Perturbation Fields in the JET Tokamak*. Phys. Rev. Lett., vol. 98, no. 26, pages 265004–5, June 2007.

[Liewer 85] P. C. Liewer. *Measurements Of Microturbulence In Tokamaks And Comparisons With Theories Of Turbulence And Anomalous Transport*. Nuclear Fusion, vol. 25, no. 5, pages 543–621, 1985.

[Linke 08] J. Linke. *High heat flux performance of plasma facing materials and components under service conditions in future fusion reactors*. Fusion Science And Technology, vol. 53, no. 2T, pages 278–287, 2008.

[Loarte 07] A. Loarte, G. Saibene, R. Sartori, V. Riccardo, P. Andrew, J. Paley, W. Fundamenski, T. Eich, A. Herrmann, G. Pautasso, A. Kirk, G. Counsell, G. Federici, G. Strohmayer, D. Whyte, A. Leonard, R. A. Pitts, I. Landman, B. Bazylev & S. Pestchanyi. *Transient heat loads in current fusion experiments, extrapolation to ITER and consequences for its operational*. Physica Scripta, vol. T128, pages 222–228, 2007.

[Markwardt 03] C.B. Markwardt. *”http://cow.physics.wisc.edu/∼craigm/idl/idl.html”*. MPFITPEAK.pro, 2003.

[Mccool 90] S. C. Mccool, A. J. Wootton, M. Kotschenreuther, A. Y. Aydemir, R. V. Bravenec, J. S. Degrassie, T. E. Evans, R. L. Hickok, B. Richards, W. L. Rowan & P. M. Schoch. *Particle-Transport Studies With Applied Resonant Fields On Text*. Nuclear Fusion, vol. 30, no. 1, pages 167–173, January 1990.

[Moyer 95] R. A. Moyer, K. H. Burrell, T. N. Carlstrom, S. Coda, R. W. Conn, E. J. Doyle, P. Gohil, R. J. Groebner, J. Kim, R. Lehmer, W. A. Peebles, M. Porkolab, C. L. Rettig, T. L. Rhodes, R. P. Seraydarian, R. Stockdale, D. M. Thomas, G. R. Tynan & J. G. Watkins. *Beyond Paradigm - Turbulence, Transport, And The Origin Of The Radial Electric-Field In Low To High Confinement Mode Transitions In The Diii-D Tokamak*. Physics Of Plasmas, vol. 2, no. 6, pages 2397–2407, 1995.

[Neubauer 05] O. Neubauer, G. Czymek, B. Giesen, P. W. Huttemann, M. Sauer, W. Schalt & J. Schruff. *Design features of the Tokamak TEXTOR*. Fusion Science And Technology, vol. 47, no. 2, pages 76–86, 2005.

[Nimoy 91] Leonard Nimoy, Lawrence Konner, Mark Rosenthal, Nicholas Meyer, Denny Martin Flinn & Gene Roddenberry. The undiscovered country, volume VI of *Star Trek*. Paramount Pictures, 1991.

[Ongena 08a] J. Ongena. *Private Communication*, August 2008.

[Ongena 08b] J. P. H. E. Ongena, M. Evrard & D. McCune. *Numerical transport codes*. Fusion Science And Technology, vol. 53, no. 2T, pages 367–376, 2008.

[Pluecker 58] Pluecker. *Ueber die Einwirkung des Magneten auf die elektrischen Entladungen in verduennten Gasen*. Annalen der Physik und Chemie, vol. 103, page 88, 1858.

[Press 92] W.H. Press, S.A. Flannery B.P.Teukolsky & W.T. Vetterling. ”numerical recipes in c”. Cambridge University Press, 2nd edition, 1992.

[Reimerdes 06] H. Reimerdes, T. C. Hender, S. A. Sabbagh, J. M. Bialek, M. S. Chu, A. M. Garofalo, M. P. Gryaznevich, D. F. Howell, G. L. Jackson, R. J. La Haye, Y. Q. Liu, J. E. Menard, G. A. Navratil, M. Okabayashi, S. D. Pinches, A. C. Sontag, E. J. Strait, W. Zhu, M. Bigi, M. de Baar, P. de Vries, D. A. Gates, P. Gohil, R. J. Groebner, D. Mueller, R. Raman, J. T. Scoville & W. M. Solomon. *Cross-machine comparison of resonant field amplification and resistive wall mode stabilization by plasma rotation*, May 2006.

[Rice 97] J. E. Rice, E. S. Marmar, F. Bombarda & L. Qu. *X-ray observations of central toroidal rotation in ohmic Alcator C-Mod plasmas*. Nuclear Fusion, vol. 37, no. 3, pages 421–426, 1997.

[Rice 04] J. E. Rice, W. D. Lee, E. S. Marmar, N. P. Basse, P. T. Bonoli, M. J. Greenwald, A. E. Hubbard, J. W. Hughes, I. H. Hutchinson, A. Ince-Cushman, J. H. Irby, Y. Lin, D. Mossessian, J. A. Snipes, S. M. Wolfe, S. J. Wukitch & K. Zhurovich. *Toroidal rotation and momentum transport in Alcator C-Mod plasmas with no momentum input*. Physics Of Plasmas, vol. 11, no. 5, pages 2427–2432, 2004.

[Rozhansky 96] V. Rozhansky & M. Tendler. *Plasma Rotation in Tokamaks*. Reviews of Plasma Physics, vol. 19, page 147, 1996.

[Savitzky 64] A. Savitzky & M. J. E. Golay. *Smoothing + Differentiation Of Data By Simplified Least Squares Procedures*. Analytical Chemistry, vol. 36, no. 8, pages 1627–&, 1964.

[Schmitz 07] O. Schmitz, D. Harting, S. S. Abdullaev, S. Brezinsek, K. H. Finken, H. Frerichs, M. Jakubowski, M. Lehnen, X. Loozen, P. Mertens, D. Reiter, U. Samm, B. Schweer, G. Sergienko, M. Z. Tokar, B. Unterberg & R. C. Wolf. *Characterization of transport in the stochastic edge layer of TEXTOR by analysis of the radial and poloidal distribution of electron density and temperature*. Journal Of Nuclear Materials, vol. 363, pages 680–685, June 2007.

[Schmitz 08a] O. Schmitz, S. Brezinsek, I. Classen, M. Clever, J. W. Coenen, E. Delabie, K. H. Finken, M. W. Jakubowski, M. Kantor, A. Kramer-Flecken, U. Kruezi, M. Lehnen, Y. Liang, D. Reiter, U. Samm, B. Schweer, G. W. Spakman, H. Stoschus, G. Telesca, B. Unterberg, E. Uzgel, Y. Xu & TEXTOR Team. *Application of advanced edge diagnostics for transport studies in the stochastic boundary of TEXTOR-DED*. Plasma 2007, vol. 993, pages 135–142, 2008.

[Schmitz 08b] O. Schmitz, M. W. Jakubowski, H. Frerichs, D. Harting, M. Lelmen, B. Unterberg, S. S. Abduallaev, S. Brezinsek, I. Classen, T. Evans, Y. Feng, K. H. Finken, M. Kantor, D. Reiter, U. Samm, B. Schweer, G. Sergienko, G. W. Spakman, M. Tokar, E. Uzgel, R. C. Wolf & TEXTOR Team. *Identification and analysis of transport domains in the stochastic boundary of TEXTOR-DED for different mode spectra*. Nuclear Fusion, vol. 48, no. 2, 2008.

[Schmitz 09] O. Schmitz, J.W. Coenen, H. Frerichs, M. Kantor, M. Lehnen, B. Unterberg, S. Brezinsek, M. Clever, T. Evans, K.H. Finken, M. Jakubowski, A. Kraemer-Flecken, V. Phillips, D. Reiter, U. Samm, G.W. Spakman & G. Telesca. *Particle Confinement Control with Resonant Magnetic Perturbations at TEXTOR*. Journal of Nuclear Materials, 18th International Conference on Plasma Surface Interaction in Controlled Fusion Devices (PSI), vol. In Press, Accepted Manuscript, pages –, 2009.

[Schorn 92] R. P. Schorn, E. Wolfrum, F. Aumayer, E. Hintz, D. Rusbuldt & H. Winter. *Radial Temperature Distributions Of C-6+ Ions In The Textor Edge Plasma Measured With Lithium Beam Activated Charge-Exchange Spectroscopy*. Nuclear Fusion, vol. 32, no. 3, pages 351–359, 1992.

[Schweer 08] B. Schweer. *Application of atomic beams in combination with spectroscopic observation for plasma diagnostic*. Fusion Science And Technology, vol. 53, no. 2T, pages 425–432, 2008.

[Severo 03] J. H. F. Severo, I. C. Nascimento, V. S. Tsypin & R. M. O. Galvao. *Plasma residual rotation in the TCABR tokamak*. Nuclear Fusion, vol. 43, no. 10, pages 1047–1056, 2003.

[Soldatov 07] S. Soldatov, A. Kraemer-Flecken, M. van Wassenhoven G. de Bock & the TEXTOR team. *The poloidal asymmetry in perpendicular plasma rotation and radial electric field measured with Correlation Reflectometry at TEXTOR*. Europhysics Conference Abstracts, vol. 31F, 2007.

[Solomon 06] W. M. Solomon, K. H. Burrell, R. Andre, L. R. Baylor, R. Budny, P. Gohil, R. J. Groebner, C. T. Holcomb, W. A. Houlberg & M. R. Wade. *Experimental test of the neoclassical theory of impurity poloidal rotation in tokamaks*. Physics Of Plasmas, vol. 13, no. 5, 2006.

[Stacey 05] Weston M. Stacey. Fusion plasma physics. WILEY-VCH Verlag GmbH & Co. KGaA, Weinheim, 2005.

[Stangeby 00] P.C. Stangeby. The plasma boundary of magnetic fusion devices. IoP, 2000.

[Summers 94] H. P. Summers. *Atomic Data and Analysis Structures*. JET-IR, vol. (94)06, 1994.

[Synakowski 97] E. J. Synakowski, S. H. Batha, M. A. Beer, M. G. Bell, R. E. Bell, R. V. Budny, C. E. Bush, P. C. Efthimion, G. W. Hammett, T. S. Hahm, B. LeBlanc, F. Levinton, E. Mazzucato, H. Park, A. T. Ramsey, G. Rewoldt, S. D. Scott, G. Schmidt, W. M. Tang, G. Taylor & M. C. Zarnstorff. *Roles of electric field shear and Shafranov shift in sustaining high confinement in enhanced reversed shear plasmas on the TFTR Tokamak*. Physical Review Letters, vol. 78, no. 15, pages 2972–2975, April 1997.

[Testa 06] D. Testa, L. Garzotti & C. Giroud. *The role of the radial electric field for the transition to high confinement regimes*. Nuclear Fusion, vol. 46, no. 5, pages 562–579, May 2006.

[Trier 08] E. Trier, L. G. Eriksson, P. Hennequin, C. Fenzi, C. Bourdelle, G. Falchetto, X. Garbet, T. Aniel, F. Clairet & R. Sabot. *Radial electric field measurements in a tokamak with magnetic field ripple*. Nuclear Fusion, vol. 48, page 092001, 2008.

[Uhlemann 93] R. Uhlemann, R. S. Hemsworth, G. Wang & H. Euringer. *Hydrogen And Deuterium Ion Species Mix And Injected Neutral Beam Power Fractions Of The Textor-Pinis For 20-60 KV Determined By Doppler-Shift Spectroscopy*. Review Of Scientific Instruments, vol. 64, no. 4, pages 974–982, 1993.

[Uhlemann 99] R. Uhlemann & J. Ongena. *Variation of injected neutral beam power at constant particle energy by changing the beam target aperture of the textor neutral beam injectors*. Fusion Technology, vol. 35, no. 1, pages 42–53, 1999.

[Unterberg 07] B. Unterberg, C. Busch, M. de Bock, J. W. Coenen, K. H. Finken, S. Jachmich, M. W. Jakubowski, Y. Kikuchi, A. Kramer-Flecken, M. Lehnen, U. Samm, O. Schmitz, S. Soldatov, M. Z. Tokar, M. von Hellermann, R. C. Wolf, Y. Xu & TEXTOR-team. *Impact of stochastic magnetic fields on plasma rotation and radial electric fields in the plasma edge of the tokamak TEXTOR*. Journal Of Nuclear Materials, vol. 363, pages 698–702, 2007.

[Unterberg 08] B. Unterberg. *Transport processes in the plasma edge*. Fusion Science And Technology, vol. 53, no. 2T, pages 229–242, 2008.

[Unterberg 09] B Unterberg, S.S. Abdullaev, J.W. Coenen, K. H. Finken, H. Frerichs, M.W. Jakubowski, D. Kalupin, M. Kantor, A. Kraemer-Flecken, Y. Liang, M. Lehnen, U. Samm, O. Schmitz, G. Sergienko, S. Soldatov, H. Stoschus, M. Tokar, G. W. Spakman, E. Uzgel, G. van Wassenhoven, O. Zimmermann, Y. Xu & the TEXTOR team. *The Influence of Resonant Magnetic Perturbations on Edge Transport in Limiter H-mode Plasmas in TEXTOR*. Journal of Nuclear Materials, 18th International Conference on Plasma Surface Interaction in Controlled Fusion Devices (PSI), 2009.

[Van Oost 03] G. Van Oost, J. Adamek, V. Antoni, P. Balan, J. A. Boedo, P. Devynck, I. Duran, L. Eliseev, J. P. Gunn, M. Hron, C. Ionita, S. Jachmich, G. S. Kirnev, E. Martines, A. Melnikov, R. Schrittwieser, C. Silva, J. Stockel, M. Tendler, C. Varandas, M. Van Schoor, V. Vershkov & R. R. Weynants. *Turbulent transport reduction by E x B velocity shear during edge plasma biasing: recent experimental results*. Plasma Physics And Controlled Fusion, vol. 45, no. 5, pages 621–643, 2003.

[von Hellermann 00] M. von Hellermann. *A brief descriptin of the JET Charge Exchange Spectroscopy Software*. JET Internal Page , Experimental Department, Core Spectroscopy Group, 2000.

[von Hellermann 08] M. G. von Hellermann, E. Delabie, R. J. E. Jaspers, W. Biel, O. Marchuk, H. P. Summers, A. Whiteford, C. Giroud, N. C. Hawkes & K. D. Zastrow. *Active beam spectroscopy*. Burning Plasma Diagnostics, vol. 988, pages 165–176, 2008.

[Wagner 82] F. Wagner, G. Becker, K. Behringer, D. Campbell, A. Eberhagen, W. Engelhardt, G. Fussmann, O. Gehre, J. Gernhardt, G. Vongierke, G. Haas, M. Huang, F. Karger, M. Keilhacker, O. Kluber, M. Kornherr, K. Lackner, G. Lisitano, G. G. Lister, H. M. Mayer, D. Meisel, E. R. Muller, H. Murmann, H. Niedermeyer, W. Poschenrieder, H. Rapp, H. Rohr, F. Schneider, G. Siller, E. Speth, A. Stabler, K. H. Steuer, G. Venus, O. Vollmer & Z. Yu. *Regime Of Improved Confinement And High-Beta In Neutral-Beam-Heated Divertor Discharges Of The Asdex Tokamak*. Physical Review Letters, vol. 49, no. 19, pages 1408–1412, 1982.

[Wagner 84] F. Wagner, G. Fussmann, T. Grave, M. Keilhacker, M. Kornherr, K. Lackner, K. Mccormick, E. R. Muller, A. Stabler, G. Becker, K. Bernhardi, U. Ditte, A. Eberhagen, O. Gehre, J. Gernhardt, G. Vongierke, E. Glock, O. Gruber, G. Haas, M. Hesse, G. Janeschitz, F. Karger, S. Kissel, O. Kluber, G. Lisitano, H. M. Mayer, D. Meisel, V. Mertens, H. Murmann, W. Poschenrieder, H. Rapp, H. Rohr, F. Ryter, F. Schneider, G. Siller, P. Smeulders, F. Soldner, E. Speth, K. H. Steuer, Z. Szymanski & O. Vollmer. *Development Of An Edge Transport*

Barrier At The H-Mode Transition Of Asdex. Physical Review Letters, vol. 53, no. 15, pages 1453–1456, 1984.

[Wesson 97] John Wesson. Tokamaks. Oxford University Press, 1997.

[Weynants 92] R. R. Weynants, G. Vanoost, G. Bertschinger, J. Boedo, P. Brys, T. Delvigne, K. H. Dippel, F. Durodie, H. Euringer, K. H. Finken, D. S. Gray, J. D. Hey, D. L. Hillis, J. T. Hogan, L. Konen, R. Leners, A. M. Messiaen, A. Pospieszczyck, U. Samm, R. P. Schorn, B. Schweer, G. Telesca, R. Vannieuwenhove & P. E. Vandenplas. *Confinement And Profile Changes Induced By The Presence Of Positive Or Negative Radial Electric-Fields In The Edge Of The Textor Tokamak*. Nuclear Fusion, vol. 32, no. 5, pages 837–853, 1992.

[Weynants 08] R. R. Weynants. *Fusion machines*. Fusion Science And Technology, vol. 53, no. 2T, pages 37–43, 2008.

[Wiese 96] W. L. Wiese, J. R. Fuhr & T. M. Deters. Atomic transition probabilities of carbon, nitrogen, and oxygen - a critical data compilation. 1996.

[Williams 02] C. H. Williams, L. A. Dudzinski, S. K. Borowski & A. J. Juhasz. *Realizing "2001: A space odyssey": Piloted spherical torus nuclear fusion propulsion*. Journal Of Spacecraft And Rockets, vol. 39, no. 6, pages 874–885, 2002.

[Wong 08] S. K. Wong, V. S. Chan & W. M. Solomon. *Poloidal velocity of impurity ions in neoclassical theory*. Physics Of Plasmas, vol. 15, no. 8, page 082503, August 2008.

[Xu 06] Y. Xu, R. R. Weynants, S. Jachmich, M. Van Schoor, M. Vergote, P. Peleman, M. W. Jakubowski, M. Mitri, D. Reiser, B. Unterberg & K. H. Finken TEXTOR team. *Influence of the Static Dynamic Ergodic Divertor on Edge Turbulence Properties in TEXTOR*. Physical Review Letters, vol. 97, no. 16, page 165003, 2006.

[Xu 07] Y. Xu, M. Van Schoor, R. R. Weynants, S. Jachmich, M. Vergote, M. W. Jakubowski, P. Beyer, M. Mitri, B. Schweer, D. Reiser, B. Unterberg, K. H. Finken, M. Lehnen, R. Jaspers & TEXTOR Team. *Edge turbulence during the static dynamic ergodic divertor experiments in TEXTOR*. Nuclear Fusion, vol. 47, no. 12, pages 1696–1709, 2007.

[Yang 91] X. Z. Yang, B. Z. Zhang, A. J. Wootton, P. M. Schoch, B. Richards, D. Baldwin, D. L. Brower, G. G. Castle, R. D. Hazeltine, J. W. Heard, R. L. Hickok, W. L. Li, H. Lin, S. C. Mccool, V. J. Simcic, L. P. Ritz & C. X. Yu. *The Space Potential In The Tokamak Text*. Physics Of Fluids B-Plasma Physics, vol. 3, no. 12, pages 3448–3461, 1991.

[Yoshida 08] M. Yoshida, Y. Kamada, H. Takenaga, Y. Sakamoto, H. Urano, N. Oyama, G. Matsunaga & The JT-60 Team. *Physics Mechanisms* *of Toroidal Rotation Profile and Properties of Momentum Transport in JT-60 Using*. Plasma and Fusion Research, vol. 3, page 1007, 2008.

[Zagorski 02] R. Zagorski, H. Gerhauser, M. Lehnen & T. Loarer. *Investigations of Radial Electric Field and Global Circulation Layer in Limiter Tokamaks*. Contributions to Plasma Physics, vol. 42, no. 2-4, pages 247–252, 2002.

[Zehrfeld 99] H.P. Zehrfeld. *Resisitive Equilibrium States of Axissymmetric Plasmas with Compressible Viscous Filuid Flow*. Europhysics Conference Abstracts, vol. 23J, pages 1421–1424, 1999.

[Zemax-EE 06] Zemax-EE. *Optical Design Programm*, 2006.

[Zohm 92] H. Zohm, F. Wagner, M. Endler, J. Gernhardt, E. Holzhauer, W. Kerner & V. Mertens. *Studies Of Edge Localized Modes On Asdex*. Nuclear Fusion, vol. 32, no. 3, pages 489–494, 1992.

[Zohm 96] H. Zohm. *Edge localized modes (ELMs)*. Plasma Physics And Controlled Fusion, vol. 38, no. 2, pages 105–128, 1996.

List of Figures

List of Tables

Acknowledgement

First of all, I would like to express my deepest gratitude to my parents who had never any doubt in my abilities and always supported me in life and work. Even during the hardest of times both of them always found the right words and strength.

My special thank you goes to Prof.Dr. U.Samm, who offered me the possibility to work and perform in this remarkable work environment, not to mention the many different opportunities to step into the world of plasma physics.

Without a doubt my Huge gratitude goes to Bernhard Unterberg, Bernd Schweer and Oliver Schmitz, who with their knowledge, ideas and support were one of the foundations of my successful work. They always were able to help with patience and fruitful contributions and insights.

I would like to extend my thank you Prof. Dr. Pretzler for agreeing to be the second thesis examiner.

For the great advice and support of my colleagues in the local group i am very grateful: Oliver Schmitz who always inspired with his insight and helped whenever necessary, Meike Clever who in the last years was a great companion and support, Henning Stoschus, who helped not only by motivating me but for being there whenever possible and necessary. Mikhael Mitri who with his humor and energy made work interesting and fun. My gratitude extends to all my colleagues at the institute especially my fellow PhD Students.

A great thank you also goes to the whole technical staff, Günther Herpers, Kalle von Bovert, Klaus Klören and Dieter Schüller for their support of my work with the diagnostic development. In addition I'd like to thank the whole TEXTOR Team for their efforts and participation in the experiments.

A special thank you goes to all the people who read my work for the purpose of correcting my orthography, especially Phillipe Mertens, it must have been hard.

I owe special thanks to my twin-brother Björn for his ongoing support and help during the last years. Without him I would have never gotten that far. My gratitude also goes my friends especially to Patrick Marche and Jan F. Schorr, one couldn't have a better friends.

My most deeply felt gratitude goes to Oxana, I wouldn't have made it without her, giving me the patience and the strength to enjoy the last years. Thank you for all the hours and days we spend together. Not to forget little Vincent, he brightened my day with every step.

A somewhat outstanding and unusual 'Thank You' goes to Eugene W. Roddenberry for his inspirational work enabling me 'to boldly go" where i have "never gone before".

The future is an "undiscovered country"[Nimoy 91], lets see what it keeps in store for us.

huih

Die hier vorgelegte Dissertation habe ich eigenhändig und ohne unerlaubte Hilfe angefertigt. Die Dissertation wurde in der vorgelegten oder in ähnlicher Form noch bei keiner anderen Institution eingereicht. Ich habe bisher keine erfolglosen Promotionsversuche unternommen.

Jan W. Coenen, Düsseldorf, den 24.02.2009

Schriften des Forschungszentrums Jülich
Reihe Energie & Umwelt / Energy & Environment

1. **Einsatz von multispektralen Satellitenbilddaten in der Wasserhaushalts- und Stoffstrommodellierung – dargestellt am Beispiel des Rureinzugsgebietes**
   von C. Montzka (2008), XX, 238 Seiten
   ISBN: 978-3-89336-508-1

2. **Ozone Production in the Atmosphere Simulation Chamber SAPHIR**
   by C. A. Richter (2008), XIV, 147 pages
   ISBN: 978-3-89336-513-5

3. **Entwicklung neuer Schutz- und Kontaktierungsschichten für Hochtemperatur-Brennstoffzellen**
   von T. Kiefer (2008), 138 Seiten
   ISBN: 978-3-89336-514-2

4. **Optimierung der Reflektivität keramischer Wärmedämmschichten aus Yttrium-teilstabilisiertem Zirkoniumdioxid für den Einsatz auf metallischen Komponenten in Gasturbinen**
   von A. Stuke (2008), X, 201 Seiten
   ISBN: 978-3-89336-515-9

5. **Lichtstreuende Oberflächen, Schichten und Schichtsysteme zur Verbesserung der Lichteinkopplung in Silizium-Dünnschichtsolarzellen**
   von M. Berginski (2008), XV, 171 Seiten
   ISBN: 978-3-89336-516-6

6. **Politikszenarien für den Klimaschutz IV – Szenarien bis 2030**
   hrsg.von P. Markewitz, F. Chr. Matthes (2008), 376 Seiten
   ISBN 978-3-89336-518-0

7. **Untersuchungen zum Verschmutzungsverhalten rheinischer Braunkohlen in Kohledampferzeugern**
   von A. Schlüter (2008), 164 Seiten
   ISBN 978-3-89336-524-1

8. **Inorganic Microporous Membranes for Gas Separation in Fossil Fuel Power Plants**
   by G. van der Donk (2008), VI, 120 pages
   ISBN: 978-3-89336-525-8

9. **Sinterung von Zirkoniumdioxid-Elektrolyten im Mehrlagenverbund der oxidkeramischen Brennstoffzelle (SOFC)**
   von R. Mücke (2008), VI, 165 Seiten
   ISBN: 978-3-89336-529-6

10. **Safety Considerations on Liquid Hydrogen**
    by K. Verfondern (2008), VIII, 167 pages
    ISBN: 978-3-89336-530-2

11. **Kerosinreformierung für Luftfahrtanwendungen**
von R. C. Samsun (2008), VII, 218 Seiten
ISBN: 978-3-89336-531-9

12. **Der 4. Deutsche Wasserstoff Congress 2008 – Tagungsband**
hrsg. von D. Stolten, B. Emonts, Th. Grube (2008), 269 Seiten
ISBN: 978-3-89336-533-3

13. **Organic matter in Late Devonian sediments as an indicator for environmental changes**
by M. Kloppisch (2008), XII, 188 pages
ISBN: 978-3-89336-534-0

14. **Entschwefelung von Mitteldestillaten für die Anwendung in mobilen Brennstoffzellen-Systemen**
von J. Latz (2008), XII, 215 Seiten
ISBN: 978-3-89336-535-7

15. **RED-IMPACT**
Impact of Partitioning, Transmutation and Waste Reduction Technologies on the Final Nuclear Waste Disposal
SYNTHESIS REPORT
ed. by W. von Lensa, R. Nabbi, M. Rossbach (2008), 178 pages
ISBN 978-3-89336-538-8

16. **Ferritic Steel Interconnectors and their Interactions with Ni Base Anodes in Solid Oxide Fuel Cells (SOFC)**
by J. H. Froitzheim (2008), 169 pages
ISBN: 978-3-89336-540-1

17. **Integrated Modelling of Nutrients in Selected River Basins of Turkey**
Results of a bilateral German-Turkish Research Project
project coord. M. Karpuzcu, F. Wendland (2008), XVI, 183 pages
ISBN: 978-3-89336-541-8

18. **Isotopengeochemische Studien zur klimatischen Ausprägung der Jüngeren Dryas in terrestrischen Archiven Eurasiens**
von J. Parplies (2008), XI, 155 Seiten, Anh.
ISBN: 978-3-89336-542-5

19. **Untersuchungen zur Klimavariabilität auf dem Tibetischen Plateau -**
Ein Beitrag auf der Basis stabiler Kohlenstoff- und Sauerstoffisotope in Jahrringen von Bäumen waldgrenznaher Standorte
von J. Griessinger (2008), XIII, 172 Seiten
ISBN: 978-3-89336-544-9

20. **Neutron-Irradiation + Helium Hardening & Embrittlement Modeling of 9%Cr-Steels in an Engineering Perspective (HELENA)**
by R. Chaouadi (2008), VIII, 139 pages
ISBN: 978-3-89336-545-6

21. **Messung und Bewertung von Verkehrsemissionen**
von D. Klemp, B. Mittermaier (2009), ca. 230 Seiten, erscheint in Kürze
ISBN: 978-3-89336-546-3

22. **Verbundvorhaben APAWAGS (AOEV und Wassergenerierung) – Teilprojekt: Brennstoffreformierung – Schlussbericht**
von R. Peters, R. C. Samsun, J. Pasel, Z. Porš, D. Stolten (2008), VI, 106 Seiten
ISBN: 978-3-89336-547-0

23. **FREEVAL**
Evaluation of a Fire Radiative Power Product derived from Meteosat 8/9 and Identification of Operational User Needs
Final Report
project coord. M. Schultz, M. Wooster (2008), 139 pages
ISBN: 978-3-89336-549-4

24. **Untersuchungen zum Alkaliverhalten unter Oxycoal-Bedingungen**
von C. Weber (2008), VII, 143, XII Seiten
ISBN: 978-3-89336-551-7

25. **Grundlegende Untersuchungen zur Freisetzung von Spurstoffen, Heißgaschemie, Korrosionsbeständigkeit keramischer Werkstoffe und Alkalirückhaltung in der Druckkohlenstaubfeuerung**
von M. Müller (2008), 207 Seiten
ISBN: 978-3-89336-552-4

26. **Analytik von ozoninduzierten phenolischen Sekundärmetaboliten in *Nicotiana tabacum* L. cv Bel W3 mittels LC-MS**
von I. Koch (2008), III, V, 153 Seiten
ISBN 978-3-89336-553-1

27. **IEF-3 Report 2009. Grundlagenforschung für die Anwendung**
(2009), ca. 230 Seiten erscheint in Kürze
ISBN: 978-3-89336-554-8

28. **Influence of Composition and Processing in the Oxidation Behavior of MCrAlY-Coatings for TBC Applications**
by J. Toscano (2009), 168 pages
ISBN: 978-3-89336-556-2

29. **Modellgestützte Analyse signifikanter Phosphorbelastungen in hessischen Oberflächengewässern aus diffusen und punktuellen Quellen**
von B. Tetzlaff (2009), 149 Seiten
ISBN: 978-3-89336-557-9

30. **Nickelreaktivlot / Oxidkeramik – Fügungen als elektrisch isolierende Dichtungskonzepte für Hochtemperatur-Brennstoffzellen-Stacks**
von S. Zügner (2009), 136 Seiten
ISBN: 978-3-89336-558-6

31. **Langzeitbeobachtung der Dosisbelastung der Bevölkerung in radioaktiv kontaminierten Gebieten Weißrusslands – Korma-Studie**
von H. Dederichs, J. Pillath, B. Heuel-Fabianek, P. Hill, R. Lennartz (2009), Getr. Pag.
ISBN: 978-3-89336-532-3

32. **Herstellung von Hochtemperatur-Brennstoffzellen über physikalische Gasphasenabscheidung**
von N. Jordán Escalona (2009), 148 Seiten
ISBN: 978-3-89336-532-3

33. **Real-time Digital Control of Plasma Position and Shape on the TEXTOR Tokamak**
by M. Mitri (2009), IV, 128 Seiten
ISBN: 978-3-89336-567-8

34. **Freisetzung und Einbindung von Alkalimetallverbindungen in kohlebefeuerten Kombikraftwerken**
von M. Müller (2009), 155 Seiten
ISBN: 978-3-89336-568-5

35. **Kosten von Brennstoffzellensystemen auf Massenbasis in Abhängigkeit von der Absatzmenge**
von J. Werhahn (2009), 242 Seiten
ISBN: 978-3-89336-569-2

36. **Einfluss von Reoxidationszyklen auf die Betriebsfestigkeit von anodengestützten Festoxid-Brennstoffzellen**
von M. Ettler (2009), 138 Seiten
ISBN: 978-3-89336-570-8

37. **Großflächige Plasmaabscheidung von mikrokristallinem Silizium für mikromorphe Dünnschichtsolarmodule**
von T. Kilper (2009), XVII, 154 Seiten
ISBN: 978-3-89336-572-2

38. **Generalized detailed balance theory of solar cells**
von T. Kirchartz (2009), IV, 198 Seiten
ISBN: 978-3-89336-573-9

39. **The Influence of the Dynamic Ergodic Divertor on the Radial Electric Field at the Tokamak TEXTOR**
von J. W. Coenen (2009), xii, 122, XXVI Seiten
ISBN: 978-3-89336-574-6

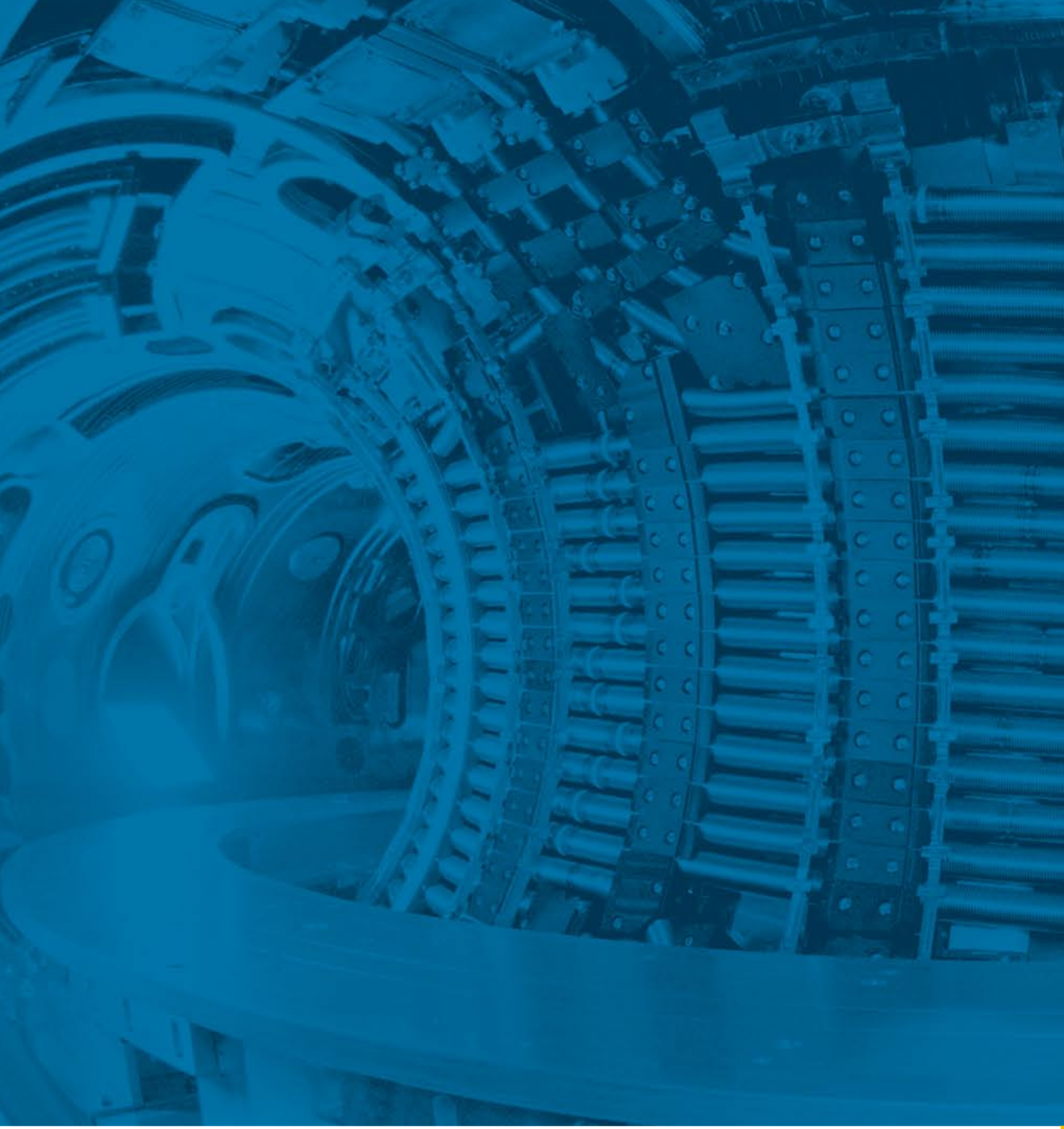

Band | Volume 39
ISBN 978-3-89336-574-6

JÜLICH
FORSCHUNGSZENTRUM